Experimental studies and modelling of high radiation and high density plasmas in the ASDEX Upgrade tokamak

Livia Casali

München 2015

Experimental studies and modelling of high radiation and high density plasmas in the ASDEX Upgrade tokamak

Dissertation zur Erlangung des akademischen Grades eines
Doktors der Naturwissenschaften (Dr. rer. nat.)
an der Fakultät für Physik der Ludwig-Maximilians-Universität München

durchgefürt am
Max-Planck-Institut für Plasmaphysik, Garching bei München

vorgelegt von
Livia Casali

München, den 14. July 2015

Erstgutachter:	Prof. Dr. Hartmut Zohm
Zweitgutachter:	Prof. Dr. Gregor Morfill
Tag der mündlichen Prüfung:	24.11.2015

”Onde, acciò che la scienza è ultima perfezione de la nostra anima,
ne la quale sta la nostra ultima felicitade,
tutti naturalmente al suo desiderio semo subietti.”

— Dante Alighieri, Convivio, 1304

Zusammenfassung

Fusionsplasmen enthalten Verunreinigungen, entweder intrinsische von der Wand, oder absichtlich injizierte mit dem Ziel die Wärmebelastung der Anlagenbauteile zu verringern, indem der Wärmefluss in Strahlung umgewandelt wird. Das Verständnis und die Vorhersage der Auswirkungen dieser Verunreinigungen und deren Strahlung auf den Plasmaeinschluß ist von äußerster Wichtigkeit um hohen Einschluss beizubehalten. Zusätzlich ist es wichtig die Auswirkungen von Pelleteinschuss auf die Plasma Leistung zu verstehen, da diese Technik höhere Dichten im Kern ermöglicht, die erforderlich sind um die Fusionsleistung zu maximieren. Diese Arbeit leistet einen Beitrag zu diesen Bemühungen sowohl durch experimentelle Untersuchungen als auch durch Modellierungen.

Die Experimente wurden an ASDEX Upgrade durchgeführt, das eine komplette Wolframwand besitzt. Das Impfen mit Verunreinigungen wurde auf H-Moden angewandt, indem Stickstoff und mittel-Z Verunreinigungen wie Kr und Ar injiziert wurden, um die Auswirkung sowohl der Rand- als auch der Zentralstrahlung auf den Einschluss zu beurteilen. Eine Datenbank aus 25 Entladungen wurde gesammelt und analysiert. Ein breites Spektrum an Plasmaparametern wurde erreicht, bis zu ITER relevanten Werten wie hoher Greenwald- und hoher Strahlungsanteil. Transportanalysen unter Berücksichtigung der Strahlungsverteilung haben gezeigt, dass Strahlung am Rand keinen wesentlichen Einfluss auf den Einschluss hat, solange das H-Mode Pedestal erhalten bleibt. Die Injektion von N induziert einen höheren Druck am Pedestal, der sich auf Grund von Profilsteifigkeit in den Kern fortpflanzt. Zentrale Strahlung muss begrenzt und kontrolliert werden um eine Verschlechterung des Einschlusses zu vermeiden. Dies erfordert eine zuverlässige Kontrolle der Verunreinigungskonzentration, aber auch die Möglichkeit die ELM Frequenz zu beeinflussen. Diese muss hoch genug gehalten werden, um eine unumkehrbare Verunreinigungsakkumulation im Zentrum und den daraus folgenden Strahlungskollaps zu vermeiden. Die Schlüsselrolle von f_{ELM} wird auch durch die Analyse der N + He Entladungen bestätigt.

Nicht koronale Effekt beeinflussen die Strahlung von niedrig-Z Verunreinigungen am Plasmarand. Aufgrund des radialen Transports, der steilen Temperaturgradienten und dem Ausschwemmen der Verunreinigungen durch ELMs, kann sich kein lokales Gleichgewicht einstellen und die Strahlung wächst in dieser Region an. Um diese Effekte zu berücksichtigen wurde ein empirisches nicht-korona Modell entwickelt, das die Verweildauer der Verunreinigungen am Pedestal berücksichtigt. Die Gültigkeit dieser Annahme wurde durch das modellieren der Verunreinigungs- und Strahlungsevolution von ASDEX Upgrade H-Moden mit Injektion von Stickstoff durch die Kopplung des Tranportcods ASTRA mit STRAHL bestätigt. Die zeitabhängigen Simulationen beinhalten die Strahlung der Verunreinigungen Stickstoff und Wolfram und die Transporteffekte, die am Rand durch ELMs hervorgerufen werden. Die Ergebnisse der Modellierung wurden mit den experimentellen Daten verglichen. Die modellierten Strahlungsprofile zeigen eine sehr gute Übereinstimmung mit den gemessenen, sowohl radial als auch temporal. Vor allem der starke Anstieg der Stickstoffstrahlung, der durch die nicht-koronalen Effekte aufgrund des ELM induzierten Transports hervorgerufen wird, wird sehr gut reproduziert. Die Strahlungseigenschaften von Wolfram werden aufgrund des schnelleren Erreichens des Ionisationsgleichgewichts nur sehr schwach von den nicht-koronalen Effekten beeinflusst. Die W Strahlung, die sehr stark von f_{ELM} abhängt, wächst aufgrund des Fehlens von genügend starkem Ausschwemmen dieser Verunreinigung sehr stark an, wenn f_{ELM} verringert wird. Dies ist in Einklang mit experimentellen Beobachtungen und belegt, dass es für die Stabilität und Leistungsfähigkeit der Entladungen essenziell ist, eine hohe ELM Frequenz zu erhalten.

Analysen des hochdichte-Szenarios zeigen mit Pellets, dass mehrere Prozesse involviert sind, wenn Pellets in das Plasma injiziert werden. Insbesondere wird ein, durch den kühlenden Effekt der Pellets bedingter, vorübergehender Abfall der im Plasma gespeicherten Energie beobachtet. Dies wird durch einen Anstieg der Dichte kompensiert. Diese Prozesse treten vor allem am Rand auf und pflanzen sich aufgrund der Profilsteifigkeit in den Kern fort. Dies erklärt, weshalb der Einschluss während der gesamten Entladung ungefähr konstant bleibt. Sowohl Experimente als auch Transportrechnungen zeigen, dass die Energieeinschlusszeit unabhängig von der Dichte ist und damit die derzeit verwendete Skalierung in diesem Regime nicht gültig ist. Die Ergebnisse dieser Arbeit werden zu einer Erweiterung der Einschlussskalierung beitragen, die derzeit durchgeführt wird.

Abstract

Fusion plasmas contain impurities, either intrinsic originating from the wall, or injected willfully with the aim of reducing power loads on machine components by converting heat flux into radiation. The understanding and the prediction of the effects of these impurities and their radiation on plasma performances is crucial in order to retain good confinement. In addition, it is important to understand the impact of pellet injection on plasma performance since this technique allows higher core densities which are required to maximise the fusion power. This thesis contributes to these efforts through both experimental investigations and modelling.

Experiments were conducted at ASDEX Upgrade which has a full-W wall. Impurity seeding was applied to H-modes by injecting nitrogen and also medium-Z impurities such as Kr and Ar to assess the impact of both edge and central radiation on confinement. A database of about 25 discharges has been collected and analysed. A wide range of plasma parameters was achieved up to ITER relevant values such as high Greenwald and high radiation fractions. Transport analyses taking into account the radiation distribution reveal that edge localised radiation losses do not significantly impact confinement as long as the H-mode pedestal is sustained. N seeding induces higher pedestal pressure which is propagated to the core via profile stiffness. Central radiation must be limited and controlled to avoid confinement degradation. This requires reliable control of the impurity concentration but also possibilities to act on the ELM frequency which must be kept high enough to avoid an irreversible impurity accumulation in the centre and the consequent radiation collapse. The key role of f_{ELM} is confirmed also by the analysis of N+He discharges.

Non-coronal effects affect the radiation of low-Z impurities at the plasma edge. Due to the radial transport, the steep temperature gradients and the ELM flush out, a local equilibrium cannot be establish an the radiation increases in this region. To account for these effects, an empirical non-coronal model was developed which takes the impurity residence time at the pedestal into account. The validity of this assumption was verified by modelling the evolution of the impurities and radiation for ASDEX Upgrade H-modes with nitrogen seeding by coupling the ASTRA transport code with STRAHL. The time-dependent simulations include impurity radiation due to nitrogen and tungsten and the transport effects induced at the edge by the ELMs. The modelling results have been validated against the experimental data. The modelled radiation profiles show a very good agreement with the measured ones over both radius and time. In particular, the strong enhancement of the nitrogen radiation caused by non-coronal effects through the ELM-induced transport is well reproduced. The radiation properties of tungsten are very weakly influenced by non-coronal effects due to the faster equilibration. W radiation, which is highly dependent on f_{ELM}, strongly increases when f_{ELM} is decreased, due to the lack of sufficiently strong flush out of this impurity. This is in agreement with the experimental observations and indicates that maintaining high ELM frequency is essential for the stability and performance of the discharges.

Analyses of the high density scenario with pellets indicate that several processes take place when pellets are injected into the plasma. In particular, due to their cooling effect, the temperature drops as soon as pellets are injected. This is compensated by an increase in density. These processes occur mainly at the edge and are propagated to the core via stiffness. This explains why the confinement stays approximately constant during the whole discharge. Both experiments and transport calculations reveal that the energy confinement time is independent of the density indicating that the currently used scaling is not valid in this regime. The results of this thesis will contribute towards an extension of the confinement scaling which is currently being undertaken.

Contents

1 Introduction **1**
- 1.1 Nuclear fusion as energy source . . . 1
- 1.2 The divertor tokamak concept . . . 2
- 1.3 High confinement mode and Edge Localised Modes . . . 5
- 1.4 Motivation and outline of this work . . . 6

2 Confinement and transport **9**
- 2.1 Global energy confinement scaling . . . 10
- 2.2 Heat and particle transport . . . 10
- 2.3 Classical transport . . . 12
- 2.4 Neoclassical transport . . . 13
- 2.5 Turbulent transport . . . 16
- 2.6 Transport in the plasma core and in the pedestal . . . 18

3 Radiation processes **19**
- 3.1 Coronal and non-coronal equilibrium . . . 19
- 3.2 Radiative processes . . . 24
- 3.3 Impurity seeding and the power exhaust problem . . . 25

4 Numerical tools **27**
- 4.1 TRANSP and ASTRA . . . 27
- 4.2 STRAHL . . . 28
- 4.3 Coupling between ASTRA and STRAHL . . . 30

5 Experimental framework **33**
- 5.1 The ASDEX Upgrade tokamak . . . 33
- 5.2 Heating systems . . . 34
  - 5.2.1 Neutral beam injection . . . 34
  - 5.2.2 Electron cyclotron resonance heating . . . 35
  - 5.2.3 Ion cyclotron resonance heating . . . 36
- 5.3 Diagnostics . . . 37
  - 5.3.1 Interferometry . . . 37
  - 5.3.2 Thomson scattering . . . 40

5.3.3 Lithium beam emission spectroscopy . . . 40
5.3.4 Electron Cyclotron Emission spectroscopy . . . 41
5.3.5 Integrated data analysis . . . 42
5.3.6 Charge exchange recombination spectroscopy . . . 42
5.3.7 Bolometry . . . 43
5.3.8 Tungsten diagnostic . . . 44

6 High radiation experiments 45
6.1 Tomography reconstruction . . . 46
6.2 Development of a non-coronal radiation model . . . 47
6.3 Experiment set up . . . 50
6.4 Transport analysis . . . 50
6.4.1 Transport analysis of nitrogen seeded discharges . . . 51
6.4.2 Transport analysis of nitrogen and krypton seeded discharges . . . 55
6.4.3 Transport analysis of nitrogen and helium seeded discharges . . . 63
6.5 Database of seeded discharges . . . 68
6.6 Discussion . . . 72

7 Modelling of the radiation and impurity evolution in presence of ELMs 73
7.1 Motivation . . . 73
7.2 Energy and particle transport model . . . 74
7.2.1 Core and pedestal modelling . . . 75
7.2.2 ELM modelling . . . 77
7.3 Modelling results . . . 78
7.3.1 Diffusive ELM model . . . 78
7.3.2 Convective ELM model . . . 88
7.3.3 Comparison with bolometry . . . 95
7.4 Comparison with the PIRT model . . . 100
7.5 Summary and discussion . . . 101

8 High density experiments with pellets 103
8.1 Experiment set up . . . 103
8.2 Temperature and density studies . . . 104
8.2.1 Transport analysis . . . 107
8.2.2 Confinement analysis . . . 110

9 Summary, conclusion and outlook 113

A Development of an algorithm for fringe jump corrections 119

B Bibliography 123

Chapter 1

Introduction

This chapter introduces the fundamental principles of nuclear fusion with emphasis on the divertor tokamak concept. It introduces the High confinement mode and Edge Localised modes. Their behaviour under high radiation and high density conditions is investigated in this thesis.

1.1 Nuclear fusion as energy source

In the search for a new CO_2-free energy source able to satisfy the strong increase of energy demand which characterises our time, fusion energy constitutes an excellent candidate. The fusion reaction as a source of power on Earth involves two isotopes of hydrogen: deuterium and tritium. They fuse to form helium and a neutron releasing 17.6 MeV per fusion reaction:

$$^2\mathrm{D} + ^3\mathrm{T} \rightarrow ^4\mathrm{He}(3.52\ \mathrm{MeV}) + n(14.07\ \mathrm{MeV}) \tag{1.1}$$

Tritium is unstable, thus it is bred from lithium using the neutron from the fusion reaction. The lithium in one laptop battery, complemented with half a bath of water, would produce the same amount of electricity as burning 40 tonnes of coal [1]. Several key attributes make fusion a desirable technology for power production: the almost unlimited fuel supply readily accessible everywhere assures energy security independent of geopolitical situations; the intrinsic safe operation due to the small amount of fuel present in the active volume; no chain reaction; the relatively short lifetime of the produced radioactive isotopes; no CO_2 greenhouse gas emission.

Very high temperatures of about 10 keV are required to enable the particles to overcome the Coulomb barrier and fuse together. At such high temperatures the electrons are not

bound to the nuclei and the matter is in the plasma state. While in the sun, the plasma is confined by its own gravity, on Earth plasma can be confined by its own inertia (inertial fusion) or by strong magnetic fields (magnetic confinement). The magnetic confinement is currently a very promising approach. However one of its main challenges is to cope with strong heat and particle losses due to radial transport which prevents the plasma from reaching the necessary conditions to initiate a fusion reaction. In order to obtain a net yield of energy the high temperatures must be sustained with a sufficient ion density and with a sufficient confinement time such that the heating power needed to heat the plasma is low enough. The threshold for ignition, i.e. the point where the heating of alpha particles produced by the fusion reactions self-sustain the plasma temperature without any additional heating is given by the Lawson criterion: the triple product of the ion density n_i, the temperature T_i and the energy confinement time τ_E has to be $> 5 \cdot 10^{21}$keV m^{-3}. The required temperature is set by the fusion reaction cross section at about 10 keV for D-T reactions. For the density an empirical limit exists. Therefore, increasing the fusion triple product needs an increase of the energy confinement time, which itself requires an understanding of the transport mechanisms in a magnetically confined plasma.

In absence of impurities (i.e. any ion which is not part of the fuel) the power balance reads $P_\alpha = P_{rad} + P_{transp}$ where P_{rad} are the energy losses due to radiation and P_{transp} the energy losses due to conduction and convection. The presence of impurities, either intrinsic or deliberately puffed for radiative purposes, lowers fusion output through both impurity radiation and through dilution of hydrogen. This necessitates a modification of the Lawson criterion. An example of a modified Lawson criterion is given in Ref. [2]:

$$n_e \cdot \tau_E \geq \frac{3 f_{tot} \cdot T}{4 < \sigma_{DT} v > \cdot f_H^2 \cdot E_\alpha - L_Z(T)} \tag{1.2}$$

where n_e is the electron density, $f_{tot} = \frac{\Sigma_i n_i}{n_e} \leq 1$ is the ion-electron density fraction (dilution), $T = T_e = T_i$, $< \sigma_{DT} v >$ is the fusion reaction rate of the D-T reaction, $f_H = \frac{n_H}{n_e}$ is the fractional abundance of the hydrogenic species, E_α is the kinetic energy of the alpha particles and L_Z the loss function due to line radiation and recombination of impurities (if the nucleus is not fully stripped, line radiation and recombination are much stronger than bremsstrahlung). Without radiation losses ($L_Z = 0$) and dilution ($f_{tot} = f_H$=1) the formula is the standard Lawson criterion.

1.2 The divertor tokamak concept

The tokamak is a well established magnetic configuration to confine plasmas. It consists of three fundamental magnetic systems as illustrated in figure 1.1 a) :

- Toroidal external coils: to produce the toroidal magnetic field.

- Ohmic transformer: to induce a toroidal plasma current which creates the poloidal field component. The toroidal ohmic current is inductively driven, which limits the tokamak to a pulsed operation.

- Vertical field coils: to define the shape of the plasma ring and control its position.

The superposition of the toroidal and poloidal component of the magnetic field leads to an axisymmetric equilibrium where the pressure gradient $\vec{\nabla} p$ is balanced by the magnetic force: $\vec{j} \times \vec{B} = \vec{\nabla} p$. For such an equilibrium the magnetic field lines lie on nested magnetic surfaces (panel b)) where the pressure and the current j are constant.

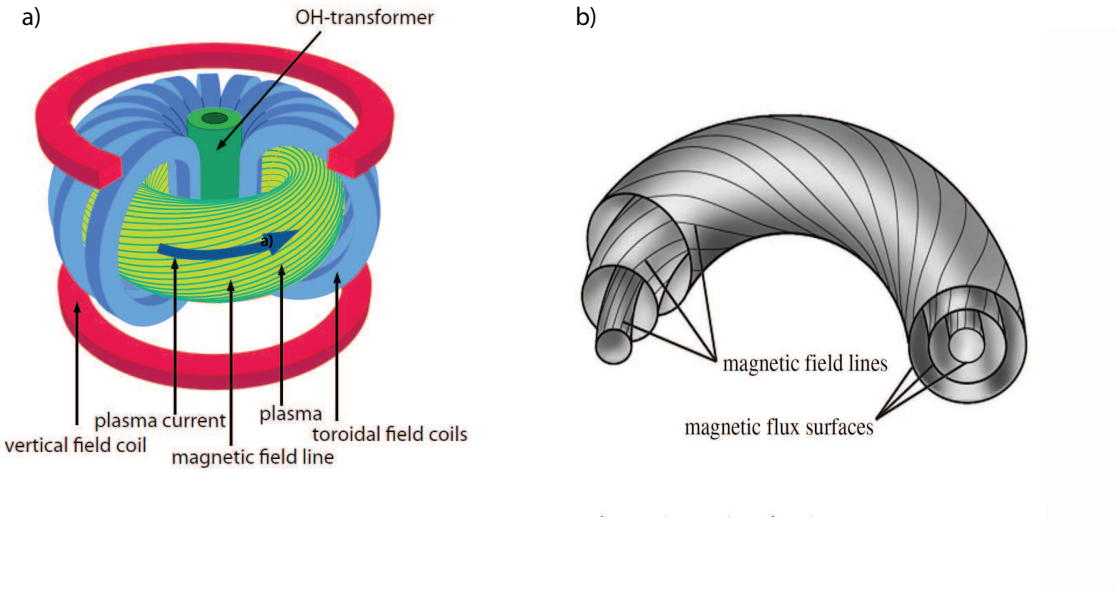

Figure 1.1: a) Schematic view of the tokamak with its magnetic components, b) Magnetic flux surfaces defined by helical field lines.

Plasma performance is described in terms of β, defined as the ratio of the plasma pressure to the magnetic pressure. It is often expressed in terms of the normalised β_N, an operational parameter indicating how close the plasma is to destabilising a magneto-hydrodynamic activity: The normalised beta is defined as:

$$\beta_N = \beta \frac{a \cdot B}{I_p} \tag{1.3}$$

where B is the toroidal magnetic field, a the minor radius, I_p the plasma current. The Greenwald limit is an empirical tokamak operation upper limit for the average density [3]:

$$n_{e,GW} = \frac{I_p}{\pi \cdot a^2}; \qquad n_{e,GW}[10^{20}\mathrm{m}^{-3}],\ I_p[\mathrm{MA}],\ a[\mathrm{m}] \tag{1.4}$$

Exceeding this density limit results in a disruption of the plasma current. However, this limit can be regarded as an edge density limit. This means, while the pedestal top density stays below $\frac{n}{n_{GW}} = 1$, higher core densities can be achieved, which is important for fusion reactors. This aspect will be discussed in chapter 8. For successful tokamak operation, it is essential to limit the entry of sputtered impurities from the wall into the plasma where they give rise to radiation losses and dilute the fuel (see section 3). This requires an effective insulation of the plasma from the vacuum vessel. Such an insulation can be obtained with additional coils deflecting the outer field lines into the so-called *divertor*, as can be see in figure 1.2. That way an X-point is introduced specifying the point where the poloidal magnetic flux is zero. The flux surface containing the X-point is called separatrix. The magnetic separatrix defines the last closed flux surface (LCFS) which separates the confined inner region from the outer region called Scrape Off Layer (SOL). As shown in figure 1.2, heat and particles diffuse from the plasma center towards the edge, cross the separatrix and reach the divertor following the magnetic field lines. There the density of neutrals, ions and electrons is strongly increased decreasing the local temperature. Typical divertor temperatures are in the range of 10 eV. The power deposition at the divertor target is localised in a very narrow region ($\sim$ 1 cm) and therefore the heat flux density is very high. It has been estimated that the maximum limit of heat flux density tolerable for the plasma facing components (PFC) is in the range of 10 MWm^{-2} [4]. For future reactors the heat flux will be much higher and well above this limit. Thus, a large fraction of the power will need to be radiated in both divertor and core region in order to assure the lifetime of the PFC (see section 3.3).

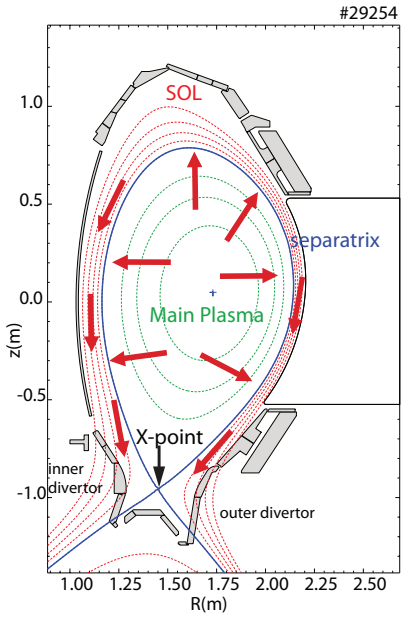

Figure 1.2: ASDEX Upgrade poloidal cross section of magnetic surfaces in divertor configuration.

The flux surfaces are contours of constant toroidal and poloidal magnetic flux and can be labeled with the normalised poloidal and toroidal flux label serving as a radial coordinates:

- Normalised poloidal flux radius ρ_{pol}:

$$\rho_{pol} = \sqrt{\frac{\Psi - \Psi_a}{\Psi_s - \Psi_a}}; \tag{1.5}$$

  where Ψ_a and Ψ_s are the poloidal flux at the magnetic axis and at the separatrix. This coordinate is scaled so that $\rho_{pol} = 0$ at the magnetic axis and $\rho_{pol} = 1$ at the separatrix. It is defined inside and outside the separatrix.

- Normalised toroidal flux radius ρ_{tor}:

$$\rho_{tor} = \sqrt{\frac{\Phi - \Phi_a}{\Phi_s - \Phi_a}} \tag{1.6}$$

  where Φ_a and Φ_s are the toroidal flux at the magnetic axis and at the separatrix. This coordinate is scaled so that $\rho_{tor} = 0$ at the magnetic axis and $\rho_{tor} = 1$ at the separatrix. This coordinate is only defined inside the separatrix.

1.3 High confinement mode and Edge Localised Modes

A tokamak can operate in different regimes with different confinement levels. The regime with a low confinement is dubbed L-mode. With sufficient heating power, the plasma spontaneously transits from L-mode to H-mode. The H-mode was discovered at the ASDEX tokamak (Garching) [5] in 1982. With a confinement improvement of about a factor of 2 compared to L-mode, its discovery represented a revolutionary leap in plasma scenarios. This regime is characterised by the formation of a narrow edge transport barrier (ETB) just inside the separatrix in which the transport for both heat and particles is strongly reduced. This creates high temperature and density gradients in the ETB leading to the steepening of the pressure profile in this region. The steepening determines the formation of a characteristic structure called pedestal (see figure 1.3). Its height determines to a large extent the total stored energy of the plasma.

H-modes are usually accompanied by regular MHD instabilities, the Edge Localised Modes (ELMs) [6]. Each ELM expels a significant amount of particles and energy from the pedestal into the SOL during its short ($\sim 1-2$ ms) crash. Following the magnetic field lines (figure 1.2) the expelled plasma reaches the divertor region depositing high heat loads of the order of several MW/m^2 during a very short time in the order of few ms. The pedestal is then re-established on a longer time scale. In current fusion experiments the expelled energy can reach about 10% of the stored energy. However, in fusion reactors like ITER (International Thermonuclear Experimental Reactor [7, 8]) and DEMO (DEMOnstration power plant [9]) the ELM-induced peak heat fluxes are estimated to

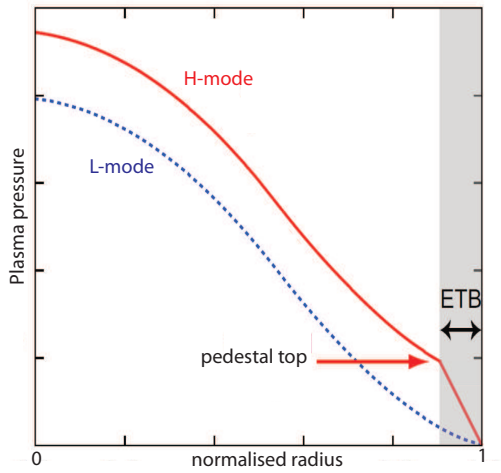

Figure 1.3: Schematic comparison of pressure profiles of the L-mode and H-mode.

greatly exceed the tolerable limit of 0.05 GJm$^{-2}s^{-\frac{1}{2}}$ [10]. On the other side, ELMs have beneficial effects: by flushing out impurities they avoid an unacceptable high impurity concentration in the plasma. Therefore, the understanding of heat and particle transport during ELMs is an important goal for scenario development, especially in reactor conditions. For such conditions a regime with frequent small ELMs could be more favourable than one with large rare ELMs. This aspect will be discussed in chapter 7.

1.4 Motivation and outline of this work

For a burning plasma device like ITER and DEMO, main chamber radiation and divertor radiation by impurity seeding will be mandatory to reduce power loads in the divertor region. The spatial distribution of the radiated power is crucial. It has to be such that the confinement is not degraded. Central radiation has to be applied inside the separatrix but not in the very central region. Strong core radiation losses must be avoided because they cool the plasma core and reduce fusion performance. To optimise the spatial radiation distribution the use of at least 2 seeding species is required. However, the presence of impurities affects fusion performance both through the impact of radiation losses as well as through fuel dilution which lowers fusion output. At ASDEX Upgrade, divertor cooling by nitrogen seeding has been extensively investigated and a confinement increase due to the presence of nitrogen has been discovered. Despite the high radiation, the stored energy of the plasma was found to increase. In this work the high radiation scenario was investigated not only by means of nitrogen seeding but also by injecting medium and high-Z impurities to assess the impact of central radiation. The relevant questions addressed in

this thesis are:

- What is the effect of high radiation and fuel dilution by impurities on heat transport and energy confinement?
- How does the plasma respond to different impurities?
- Which parameter ranges have been reached in the experiments? Are they ITER relevant?
- Is it possible to reproduce the experimental observations by modelling, predict and control detrimental events such as W accumulation?
- Is it important to take non-coronal effects for radiation calculations into account?

To answer these questions transport analyses have been carried out taking the spatial radiation distribution into account. Since edge radiation is affected by the so-called non-coronal effects, a non-coronal model was developed in order to provide a reliable radiation profile for transport calculations. The experimental investigations have been complemented with extensive modelling to gain a better understanding of the complex physical mechanisms which govern the evolution of radiation and impurities in presence of ELMs.

Besides the high radiation fraction requirements, future fusion devices will need to work at high densities in order to maximise fusion performances. It has been demonstrated that high core density can be successfully achieved by pellet injection. The relevant questions addressed in this thesis are:

- What is the effect of high densities induced by pellets on energy confinement?
- Are the scaling predictions for ITER also valid in this regime?

This work is structured as follows: the basic physics of confinement and transport processes in plasmas are briefly presented in chapter 2. Impurity radiation and the concept of coronal and non-coronal equilibrium are described in chapter 3. Chapter 4 introduces the numerical codes employed for the transport analysis and the modelling. The ASDEX Upgrade tokamak, its heating systems and main diagnostics used in this work are presented in chapter 5. The experimental studies and transport analysis of the high radiation discharges are presented in chapter 6. The modelling of the nitrogen seeded discharges in presence of tungsten and ELMs is discussed in chapter 7. Chapter 8 deals with the high density experiments. Summary, conclusions and outlook are given in chapter 9.

Chapter 2

Confinement and transport

As indicated in section 1.1, the figure of merit for fusion performance is the triple product $n_e \cdot T_i \cdot \tau_E$. The energy confinement time τ_E in steady state is defined as the plasma stored energy divided by the heating power:

$$\tau_E = \frac{W}{P_{heat}} = \frac{3}{2} \cdot \frac{\int (n_e T_e + n_i T_i) d_{Vol}}{P_{heat}} \tag{2.1}$$

Fusion efficiency requires high values of τ_E, but plasma confinement is limited by the loss of particles and energy through transport and confinement. Gradients in density and temperature profiles lead to diffusive transport of particles and energy. In tokamaks, heat and particle transport occurs perpendicular to the toroidal magnetic flux surfaces, called radial transport. In fusion reactors, heat transport should be as low as possible to minimize the required heating power. Particle transport should be low enough to reach the required density without causing impurity accumulation of helium ash and high-Z elements [11]. The radial transport, together with the plasma edge (pedestal), determines the global energy and particle confinement. Hence, understanding the transport of heat, particles and impurities is one of the main goals of fusion research.

Section 2.1 introduces the energy confinement scaling. The heat and particle transport mechanism are described in section 2.2. The classical, neoclassical and turbulent transport is described in section 2.3, 2.4 and 2.5. The relative importance of the transport processes in the different plasma regions is discussed in section 2.6.

2.1 Global energy confinement scaling

The theoretical and experimental complexity of the processes determining heat and particle transport renders first principles derivation of the dependence of energy confinement on plasma parameters a difficult task which is not yet completed. Therefore, empirical multi-machine scalings have been developed in order to describe quantitatively the variation of τ_E with the change of plasma parameters across a wide range of plasma conditions. Usually the so-called engineering parameters such as plasma current, toroidal magnetic field, density and heating power are used. They are called engineering because they can be controlled externally [12]. A large amount of data from different machines is collected and fits to the data are performed. The design of future devices, such as ITER, is based on these empirical scalings. The most widely used scaling for the energy confinement time since 1998 is the so-called IPB98(y,2) [13] which is obtained from H-mode discharges in presence of ELMs:

$$\begin{aligned} \tau_{E,IPB98(y,2)} = 0.145 \cdot \kappa^{0.78} \cdot I_p^{0.93} \cdot B_t^{0.15} \cdot n_e^{0.41} \cdot P_L^{-0.69} \cdot R^{1.39} \cdot a^{0.58}; \\ I_p[MA], B_t[T], n_e[10^{19} m^{-3}], P_L[MW], R[m^{-3}], a[m] \end{aligned} \tag{2.2}$$

κ is the elongation and P_L is the total heating power minus the temporal change of the stored energy ($P_{heat} - \frac{dW}{dt}$) not corrected for radiation.

The strong positive dependence of τ_E on machine size R and toroidal plasma current I_p indicates that future power plants must be large. Moreover, a confinement degradation is observed with increasing heating power. This phenomenon, known as power degradation of the energy confinement, is the natural consequence of the turbulent nature of transport (see section 2.5). The favourable density dependence, predicted by the IPB98, is lost when approaching the Greenwald density. This issue will be discussed in detail in section 8.2.2.

2.2 Heat and particle transport

Basic equation

Transport equations describe the temporal and spatial evolution of a quantity under the influence of sources and sinks of heating and particles. To describe this evolution a fluid

representation is generally used:

$$\frac{\partial}{\partial t}u = \nabla\Gamma_u + S_u \tag{2.3}$$

u represents the density of particles or thermal energy. S_u stands for the source and sink terms, and Γ_u for the corresponding flux of the quantity u. The physics of transport is contained in the relation between fluxes and gradients, as follows.

Heat transport

Heat transport for the electron and ion channel can be treated separately so that the flux q_j is given by:

$$q_j = -n_j \cdot \chi_j \cdot \nabla T_j + \frac{5}{2}\Gamma_j \cdot T_j + U \cdot n_j \cdot T_j \tag{2.4}$$

with $j =$ electrons or ions. The first term on the right hand side is purely diffusive, thus it tends to level out temperature profiles. It can be explained by random walk processes of the particles. The other two terms represent convective contributions. In general convection is low compared to diffusion and can be neglected ($U = 0$). Since the core particle source is usually small, the contribution coming from energy convection due to a finite particle flux Γ_j may also be neglected. Thus, the heat transport can be described in terms of a purely diffusive process: $q_j = -n_j\chi_j\nabla T_j$. The heat diffusion coefficient χ_j is determined locally and contains the transport physics. It is different for electrons and ions. The two channels are coupled by heat exchange due to Coulomb collisions. At high collisionality this term is important and prevents an experimental separation of electron and ions fluxes. In this case an effective diffusivity χ_{eff} has to be used: $\chi_{eff} = \frac{q_e+q_i}{n_e\nabla T_e+n_i\nabla T_i}$. In tokamaks the heat source is provided by ohmic and auxiliary heating and by heat exchange between electrons and ions. The last term is directed from the electrons to the ions when T_e is larger than T_i and viceversa. The heat sinks are losses due to radiation and exchange term. The energy conservation equation reads:

$$\frac{3}{2}\frac{\partial(n_j \cdot T_j)}{\partial t} + \mathbf{div}(q_j) = S_j \tag{2.5}$$

It is combined with the expression of q_j given from the flux equation. Considering only the radial component, the 1-D heat diffusion equation is obtained:

$$\frac{3}{2}\frac{\partial(n_j \cdot T_j)}{\partial t} - \nabla(n_j \cdot \chi_j \cdot T_j) = Q_j \tag{2.6}$$

This equation describes the temporal and spatial behaviour of the temperature profile. The heating and the power loss integrated over the volume inside a flux surface provide the profiles of the heat flux. From the heat fluxes the heat diffusivities can be inferred from 2.7:

$$\chi_j^{PB} = -\frac{q_j}{n_j \cdot \nabla T_j} \tag{2.7}$$

This approach is called interpretative analysis or power balance. This is generally done by transport codes such as ASTRA and TRANSP used in this thesis (see section 4.1).

Particle transport

The particle flux is determined by both diffusion and convection, the latter important for particles:

$$\Gamma_j = -D\nabla n_j + \mathrm{v} n_j \tag{2.8}$$

with j= electrons, ions or impurities. While the convective term is usually considered negligible for heat transport, a net convective velocity is typically observed for particle transport. Indeed, the peaked electron density profiles observed also in absence of a central particle source cannot be explained by pure diffusion and imply the existence of an inward convective velocity usually named *pinch* [14]. Particle sources in the center are provided by neutral beam injection and pellet fuelling, at the edge by recycling and gas puffing. Particle sinks are solely located at the edge. In the absence of core particle sources ($Q_j = 0$), the particle flux at steady state is strictly zero and density profiles are determined by the local balance between (outward) diffusion and inward pinch. In this case, the particle balance equation reads:

$$\frac{\nabla n}{n} = \frac{\mathrm{v}}{D} \tag{2.9}$$

In steady state a inward convective velocity leads to a density profile which is peaked in the center. An outward velocity leads to a hollow density profile.

2.3 Classical transport

The transport produced by collisions of particles gyrating around neighbouring field lines in absence of any inhomogeneity of the magnetic field is called *classical transport* and can be described by a simple model using the random walk Ansatz, i.e diffusive transport.

Therein the typical radial steps are assumed to be of the order of the Larmor radius ρ_L and the time between two steps $\triangle t$ by the inverse of the collision frequency. This is the frequency until a particle is deflected by an angle of 90°. The following expression for the diffusion coefficient is deduced: $D = \frac{1}{2}\frac{\triangle x^2}{\triangle t} = \frac{1}{2}\rho_L^2 \nu$. Coulomb collisions between equal particles do not play a role for the radial transport. Note that it is important to specify the species involved in the collisions:

$$D_e = \rho_{L,e}^2 \cdot \nu_{e,i} = \left(\rho_{L,i}\sqrt{\frac{m_i}{m_e}}\right)^2 \cdot \nu_{i,e}\frac{m_i}{m_e} = D_i \tag{2.10}$$

Using the random walk Ansatz the heat diffusivities can be predicted as well:

$$\chi_i^{cl} \approx \rho_{L,i}^2 \cdot \nu_{i,i} \approx \sqrt{\frac{m_i}{m_e}} \cdot \rho_{L,e}^2 \nu_{e,e} \approx \sqrt{\frac{m_i}{m_e}} \cdot \chi_e^{cl} \tag{2.11}$$

The heat diffusivities are estimated to be of the order of 10^{-3} $\frac{m^2}{s}$ for ions and 10^{-4} $\frac{m^2}{s}$ for electrons. Thus, the energy loss is determined primarily by the ion confinement time. However, experimentally determined diffusion coefficients are found to be around $\chi_e^{exp} \approx \chi_i^{exp} \approx$ 1- 5 $\frac{m^2}{s}$. Therefore, the classical transport cannot be the dominant transport process. Indeed, the effect of toroidicity on particle orbits also needs to be taken into account.

2.4 Neoclassical transport

A collisional model which includes all drifts and phenomena arising from the toroidicity is called *neoclassical transport*. Since the strength of the magnetic field in tokamaks varies along the major radius with $\frac{1}{R}$, particles travelling along the magnetic field lines will pass from regions with lower B_t at the outer side of the torus, the low field side, to regions with higher B_t at the inner side, high field side. Depending of the ratio of the parallel and perpendicular velocity, a maximum magnetic field strength exists, for which particles are reflected before they reaches the innermost point of the flux surface. They return along the field line: $\frac{v_\parallel}{v_\perp}|_{LFS} < \sqrt{\frac{B_{max}}{B_{min}} - 1}$ (mirror condition). Thus, the particles are trapped. Note that due to the gradient of the magnetic field, the particle experiences a ∇B drift: downwards for electrons and upwards for ions (for typical AUG magnetic field direction). Therefore, the trapped particles do not stay exactly on the same path. Since the poloidal projection of this orbit recalls the shape of a banana, it is known as "banana orbit" and it is shown in figure 2.1.

Since the orbit crosses several flux surfaces, the perpendicular transport is enhanced. The particles complete the banana orbits only in plasmas with low collisionality $\nu < \varepsilon^{\frac{3}{2}} \cdot v_T \cdot R \cdot q$

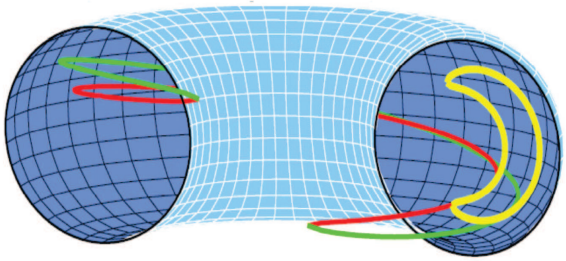

Figure 2.1: Illustration of a 3D banana orbit (green and red) and its poloidal projection (yellow).

where $\varepsilon = \frac{a}{R}$ stands for the inverse of the aspect ratio, $v_T = \sqrt{\frac{T}{m}}$ for the thermal velocity and q = $\frac{r \cdot B_0}{R_0 \cdot B_\theta}$ for the safety factor. The diffusion coefficient due to banana transport is determined by the radial extension of the banana orbit ω_{bo} and effective collisional frequency ν_{eff} between the fraction of trapped particles $\frac{n_t}{n}$:

$$D_{Banana} = \frac{n_t}{n} \omega_{bo}^2 \cdot \nu_{eff} = \frac{q^2}{\varepsilon^{\frac{3}{2}}} D_{class} \tag{2.12}$$

According to the collisionality three regimes are identified. The banana regime takes place at low collisionality. Particles subjected to many collisions before they can complete a banana orbit are in the so-called Pfirsch-Schlüter regime. In this case, trapping of particles on the low field side becomes negligible. The "Pfirsch-Schlüter" diffusion is important due to the hoop force arising from the toroidal geometry of the plasma. Then a vertical current, the so-called Pfirsch-Schlüter current is needed to balance this force. This current will give rise to a perpendicular flow through the parallel electric field. The diffusion coefficient for high collisionality can be written as: $D_{PS} = 2q^2 \cdot D_{class}$. The collisionality regime between banana (low ν) and Pfirsch-Schlüter regime (high ν) is called "Plateau regime". The name comes from the fact that in this regime the diffusion coefficient is almost independent of the collisionality forming a plateau in the plot of D vs ν. The neoclassical diffusion coefficient is dominated by the banana-plateau regime for low-Z and by the sum of the classical and Pfirsch-Schlüter contributions for high-Z elements [2]. In all regimes the values of the neoclassical diffusion are higher than the classical ones.

In addition to the increase of the diffusion coefficient, the toroidal geometry leads to an interaction of the inductive toroidal electric field used to generate the plasma current with the trapped particle in banana orbits. In presence of this electric field, the trapped particles are accelerated when traveling in direction of B and decelerated when they are on the other side of the banana orbit. Thus, the electric field displaces the particles poloidally. The

result is a net inward drift called the neoclassical *Ware Pinch* [15]:

$$v_{ware} = -k_{ware}(\nu)\frac{E_{\|}}{B_{\theta}} \tag{2.13}$$

where the factor $k_{ware}(\nu)$ is collisionality dependent. This dependence takes into account that at high collisionalities only a small part of the banana orbit can be completed before a collision.

Using calculations based on a fluid treatment and summing up all contributions (classical, banana, Pfirsch-Schlüter), a general form for the radial impurity flux can be obtained. In the following the flux for an impurity ion with ionisation stage q is given [16]:

$$\vec{\Gamma}_q = \sum_{x=class,B,Ps} D_x \left(-\nabla n_q + n_q \cdot q \left[\frac{\nabla n}{n} - H_x \frac{\nabla T}{T} \right] \right) = -D_{neo}\nabla n_q + \mathrm{v}_{neo} \cdot n_q \tag{2.14}$$

The diffusive flux (first term) is in the opposite direction to the impurity density gradient and flattens the impurity density profile. The other terms represent convective fluxes which depend on density and temperature gradients. The term $\propto \frac{\nabla n}{n}$ is directed towards the plasma center leading to a peaking of the density profile. The contribution $\propto \frac{\nabla T}{T}$ is called *temperature screening*, it changes with the transport regime and points inwards or outwards depending on the factor H_x. H_x is the collisionality dependent temperature gradient factor and itself depends on the mass ratio between collision species, plasma parameters and geometry. Since H_x is usually positive and the temperature gradients point in the same direction as the density gradient, this term is usually directed radially outwards and reduces the impurity peaking arising from the first convective term. The application of central ion heating to avoid central impurity accumulation is based on this effect. The equation also shows a strong dependence on the charge state of the impurity. This leads to a strong convection for high-Z impurities, in particular for W. This is an essential factor for the modelling work presented in chapter 7. In the low collisionality regime, the total flux is dominated by the Banana-Plateau terms, whereas in the high collisionality regime, the Pfirsch-Schlüter transport is the main contribution. The presented equation is a limiting case when only one impurity is present in the plasma. In reality, many impurities are present and the friction between all of them needs to be taken into account. This is computed by the numerical code NEOART in STRAHL (see section 4.2).

2.5 Turbulent transport

Although neoclassical transport predicts higher transport coefficients than classical theory, it still cannot explain the experimental observations, especially for the electron channel: experiments have a ratio of $\frac{\chi_i}{\chi_e}$ close to one instead of the predicted square root of the mass ratio [17]. Hence, another transport mechanism must be present which deteriorates confinement. Historically this additional transport has been termed "anomalous". Today we know it originates from microturbulences of the density and temperature. Turbulence is often associated with strong gradients, which represent free energy within a system which can drive instabilities. The main candidates are the Ion Temperature Gradient mode (ITG [18, 19]), the Trapped Electron Mode (TEM [20, 21]) and the Electron Temperature Gradient Mode (ETG [22]). The scale lengths of the fluctuations are of the order of the ion Larmor radius for ITG and TEM and of the order of the electron Larmor radius for ETG. A common feature is that the instabilities occur if the temperature gradient length $L_T = \frac{T}{\nabla T}$ drops below a certain critical threshold κ_c. The heat diffusivity strongly depends on κ_c and scales with $T^{\frac{3}{2}}$ (Gyro-Bohm dependence). Above a certain threshold, χ increases with increasing ∇T, with a slope that is proportional to $T^{\frac{3}{2}}$. Thus, the profiles become stiffer at higher temperatures, as illustrated in figure 2.2:

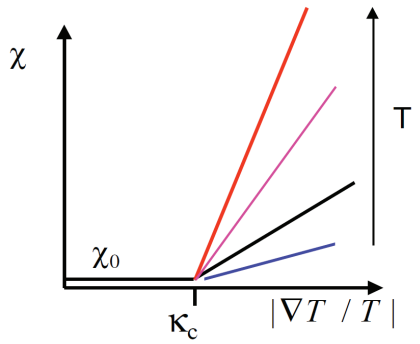

Figure 2.2: Heat transport coefficient χ vs. $\frac{\nabla T}{T}$. Above a certain threshold κ_c, χ increases with ∇T with a slope that scales as $T^{\frac{3}{2}}$ (Gyro-Bohm dependence) (adapted from [11]).

For a fixed gradient length, the central temperature depends on the edge temperature which is limited by edge instabilities [23]. This self-similarity of the temperature profiles is called "stiffness" and has been evidenced experimentally. This behaviour is the origin of the strong deterioration of confinement with heating power. The turbulent eddies are quasi-perpendicular to the toroidal magnetic field while their effect on the parallel transport is rather small. Therefore turbulence dominates the perpendicular transport. One main feature of turbulence is the interaction between different time and length scales, meaning that turbulent transport cannot be properly described by simple convection and diffusion. Locally, however, this approximation can be valid, when space and time averaged fluxes are considered [20, 24].

Collisional transport is always present even when the turbulent transport dominates. Adding the contribution from the anomalous transport $\Gamma_{an} = -D_{an}\nabla_q + \mathrm{v}_{an} n_q$ to the collisional part, the total radial impurity flux of the charge state q can be obtained:

$$\vec{\Gamma}_q = -(D_{neo,q} + D_{an,q})\nabla n_q + (\mathrm{v}_{neo,q} + \mathrm{v}_{an,q}) n_q = -D_q \cdot \nabla n_q + \mathrm{v}_q \cdot n_q \tag{2.15}$$

When turbulent transport dominates, then $D_{neo} << D_{an}$. In general for particles and impurities the neoclassical transport is important. Due to the charge dependence of convection, for high-Z elements neoclassical effects are sometimes well visible in addition to the turbulent transport and lead to strongly peaked density profiles.

Critical Gradient Model

The semi-empirical Critical Gradient Model (CGM) [25, 26] is a transport model proposed to quantify the plasma behavior above the threshold κ_c. The CGM is based on the existence of an instability threshold in the inverse temperature gradient length and of a low transport below the threshold. It is characterised by three scalar parameters per species: a threshold, a background diffusivity χ_0 and a dimensionless stiffness factor χ_s. It was initially developed for electron heat transport and it has been recently used also for ions. In the CGM the thermal diffusivity is written as:

$$\chi = \chi_s \cdot q^{\frac{3}{2}} \cdot \frac{T\rho_L}{eB_t R}\left(\frac{-R\nabla T}{T} - \kappa_c\right) \cdot H\left(\frac{-R\nabla T}{T} - \kappa_c\right) + \chi_0 \tag{2.16}$$

ρ_L is the Larmor radius and the dependence on the safety factor q has been introduced to account for the experimentally observed dependence of confinement on plasma current also supported by gyrokinetic simulations [27].

If the normalised gradient is below the threshold, the Heaviside function $H(x)$ is zero and only the background diffusivity χ_0 remains. If the normalised gradient is above the threshold, the stiffness factor χ_s quantifies the ratio between diffusivity and the difference between the logarithmic gradient of the temperature and its critical value $L_{T,crit}$ using an appropriate normalisation. A strong stiffness corresponds to a large value of χ_s. The level of stiffness characterizes how strongly the temperature profiles are tied to threshold. The CGM was assessed against experimental data in different fusion devices [26, 28, 29]. In this work it has been used to model the turbulent transport in the core (section 7.2).

2.6 Transport in the plasma core and in the pedestal

In H-mode, the transport behaviour varies significantly with plasma radius so that the pedestal is governed by different mechanisms than the plasma core. The transport at the edge is dominated by the transport due to ELM crashes and an inter-ELM transport. The latter determines the recovery time of the edge pressure in between ELMs. Within the H-mode barrier, the transport can be described neoclassically [30], and a strong inward convection is present. In the confined region, which lies between the ELM affected area and the very core region ($0.2< \rho_{tor} <0.8$), microscopic turbulence and neoclassical transport are dominant. The impurity diffusion coefficient here is turbulent. The very core region, $\rho_{tor} <0.2$, is characterised by transport dominated by MHD events called sawteeth which are quasi-periodic reconnection in the plasma centre. These considerations will be the basis of the modelling work presented in chapter 7.

Chapter 3

Radiation processes

The radial radiation distribution is an essential component of the power balance in tokamaks. It will be even more important in fusion reactors where a substantial fraction of the energy will have to be dissipated through radiation. The presence of impurities in the plasma has significant impact on fusion performance through dilution of the main ions and radiation losses. The sources of impurities in a tokamak are the plasma-wall interaction processes and the deliberate injection for diagnostic purpose or for radiative cooling. In addition, future reactors will contain helium ash which will dilute the D-T fuel significantly and reduce the fusion efficiency. The impurities relevant for fusion experiments can be classified into groups based on the emitted radiation, which in turn depends on the number of bound electrons and the plasma temperature:

- **Low-Z impurities** such as carbon, oxygen, boron and nitrogen. They have only few bound electrons and therefore are more easily stripped. Their radiation contribution is mainly at the plasma edge since in the core they are fully ionised.
- **High-Z impurities** such as tungsten, iron and nickel. They radiate over the entire plasma radius.

In addition a mid-Z ion class can be identify, which, depending on the plasma temperature, may exhibit either high-Z or low-Z behaviour. Argon and krypton fall into the mid-Z category.

3.1 Coronal and non-coronal equilibrium

Impurities enter the plasma as neutrals very localised at specific locations, but they effect the plasma at a global level (e.g. confinement time). While diffusing into the plasma,

they are successively ionised. If transport velocities are slow enough (but also depending on the T_e profile shape), the charge state distribution is governed by the balance between ionisation by collisions and recombination by radiation, which depends only on the local electron temperature, as in the solar coronal. Hence, this situation is denoted *coronal equilibrium*. For two adjacent ionisation stages the following is valid:

$$\frac{n_{Z+1}}{n_Z} = \frac{S_Z}{\alpha_{Z+1}} \tag{3.1}$$

where α_{Z+1} is the (radiative plus dielectric) recombination rate coefficient of ions with charge $Z+1$ and S_Z the ionisation rate coefficients of ions of charge Z. S_Z has the strongest dependence on T_e and governs the electron temperature dependence of the equilibrium [2]. In the coronal model, ions are excited by electron collisions and immediately decay into the ground state. Therefore, the excitation rate coefficients are fully determined by the local electron density and temperature. In a tokamak, coronal ionisation equilibrium predicts a shell-like structure of the ionisation stages, dependent on the temperature profile which increases monotonically from the edge to the centre [31]. Each shell appears where T_e is approximately one-third of the ionisation energy which is $\sim (Z+1)^2$. This quadratic dependence on the nuclear charge suggests that the concentration of heavy impurities must be kept as low as possible.

In the absence of transport, the sequence of ionisation shells starts with the neutral atom at the plasma edge and ends with the most highly stripped ions further in the plasma center. For low-Z elements, the innermost shell contains the fully ionised element. Ions with a noble gas like electron shell (He-like, Ne-like) are very stable and occupy an especially wide radial shell [2]. In steady state with negligible transport (coronal equilibrium), the radiated power emitted by an impurity species is proportional to the impurity and the electron density:

$$P_{rad} = n_e \cdot n_Z \cdot L_Z \tag{3.2}$$

where L_Z is the radiative loss function for an impurity and is a function of the electron temperature only. The data originates from ADAS, the most recent and complete atomic database [32]. $L_Z(T_e)$ curves have a principle maximum with additional subsidiary maxima. For light impurities all peaks are of similar magnitude. The principal maximum occurs at low temperatures in the range of tens of eV (see figure 3.1). At 1 keV these impurities are fully stripped. In the plasma center they contribute to radiation only through bremstrahlung. For high-Z impurities, instead, the first maximum occurs at higher temperatures and therefore impurities are not fully stripped even at reactor temperatures [33].

However, especially at the plasma edge, impurities do not have enough time to reach the coronal equilibrium. Due to radial transport and steep temperature gradients, the local equilibrium cannot be established since the ionisation and recombination times are longer than the radial transport time. This situation is denoted *non-coronal equilibrium*. In this case, the shell structure is shifted inwards and the individual width of the ionisation shells

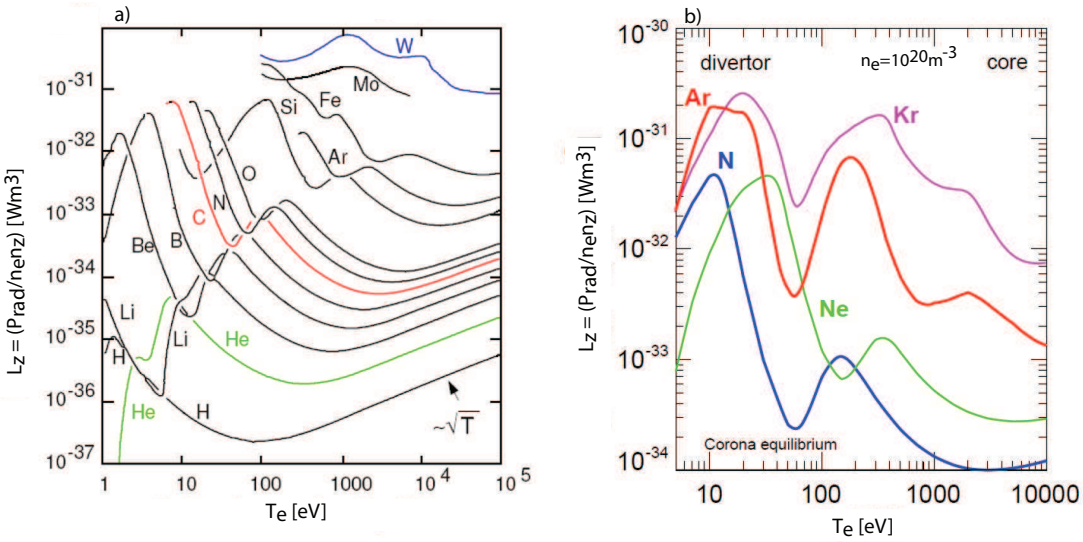

Figure 3.1: a) Radiative loss function (L_Z) for several impurities. b) L_Z for possible seed impurities from the ADAS database [32].

is broadened (see figure 3.2).

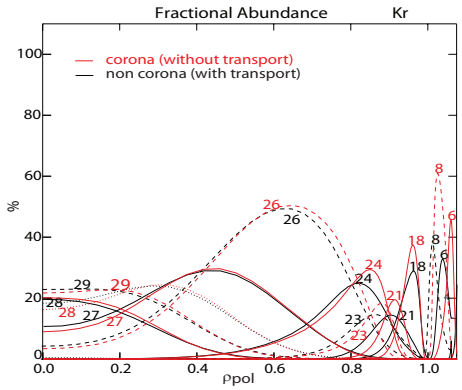

Figure 3.2: Ionisation distribution of Kr: in red assuming a local balance between ionisation and recombination (coronal conditions), in black considering the transport effects (non-coronal conditions). Note the deviation from coronall conditions at the edge.

As example, the ionisation distribution of krypton is shown. In red for coronal conditions, i.e without taking the transport effects into account and in black including them. In non-coronal conditions the shells are shifted inward and this effect is more pronounced at the plasma edge. In chapter 7 the fractional abundance of nitrogen is shown and the effects of the shell structure-shift on radiation are discussed.

The radiated energy per atom can be calculated using atomic data and a collisional-radiative model. This solves the time dependent ionisation equations as sum of bremsstrahlung, line radiation, recombination and ionisation radiation. Thereby all atomic processes are taken into account. A detailed review of the model can be found in [34]. In non-coronal conditions, the radiative loss function is not only a function of the temperature but also

of the parameter $n_e \cdot \tau$: $L_z(T_e, n_e \cdot \tau)$. The parameter $n_e \cdot \tau$ represents the ratio of the particle residence time τ and the collisional-radiative evolution time which is inversely proportional to n_e. The mean charge state $< Z >$ is a useful quantity when calculating the number of additional free electrons produced during impurity ionisation. It is defined as

$$< Z >= \frac{1}{n_I} \sum_k k \cdot n_k \tag{3.3}$$

k stands for the charge state and n_I for the total impurity density. The radiative loss function L_Z and average charge $< Z >$ corresponding to different values of $n_e \cdot \tau$ are presented in figure 3.3.

The magenta line represents coronal conditions while the red one is the farthest from coronal equilibrium, typical for divertor conditions. The plots indicate that non-coronal effects are more pronounced for low-Z than for high-Z impurities. The L_Z functions show that the farther away the impurities are from coronal equilibrium, the flatter the radiation profiles becomes. The reason is that, far from coronal equilibrium, the radiated power is dominated by line radiation, which has a weak dependence on the electron temperature. Moreover, for nitrogen the difference between coronal (magenta line) and non-coronal red line) is one order of magnitude, whereas for the other impurities the difference is marginal. The mean charge decreases with the decrease of the parameter $n_e \cdot \tau$ (far from coronal). Hence, the impurity ions have more bound electrons in a non-coronal regime compared to the coronal conditions. Thus, they produce greater radiation losses. The crucial task is the determination of τ which has been addressed in this work: following an empirical basis, a formula for τ has been proposed and a model to calculate the radiated power density in non-coronal conditions has been developed (see section 6.2).

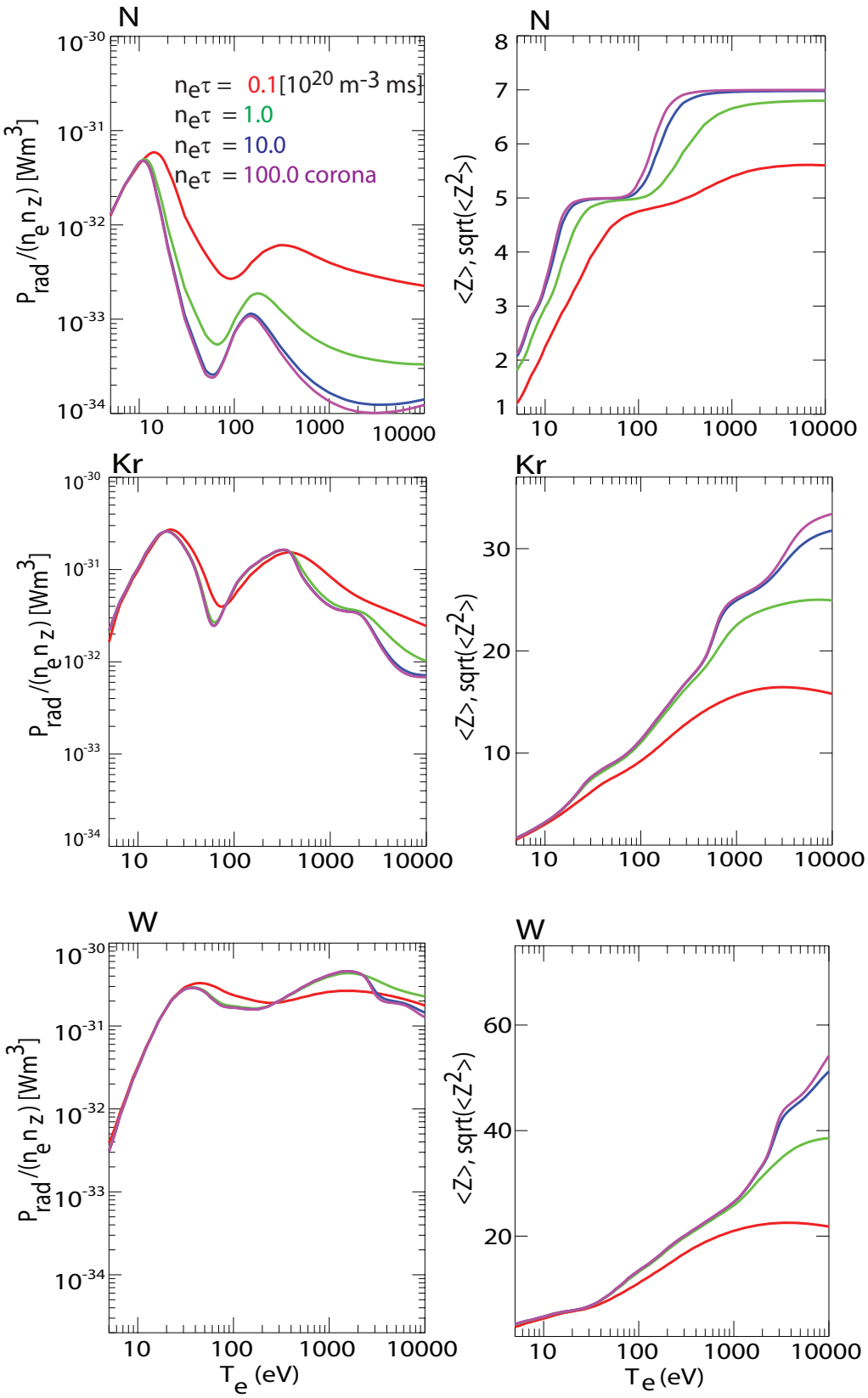

Figure 3.3: Radiative loss function and mean charge state <Z> of nitrogen, krypton and tungsten for different values of $n_e\tau$.

3.2 Radiative processes

Radiation in tokamaks comes from electrons and their transition from higher to lower energy levels. The presence of impurities results in energy losses through bremstrahlung and the atomic processes of line radiation and recombination [13]:

- **Bremstrahlung** arises from the acceleration of electrons by the electrostatic field of charged particles. The power density is given by:

$$P_B = 5.35 \cdot 10^{-27} n_e^2 \cdot Z_{eff}^2 \cdot T_e^{\frac{1}{2}} \qquad [W \cdot m^{-3}] \tag{3.4}$$

  In the formula the Gaunt factor which gives a quantum mechanical correction is taken equal to one. The effective charge is defined as

$$Z_{eff} = \frac{\sum n_i Z_i^2}{\sum n_i Z_i} \tag{3.5}$$

  Since Z_{eff} increases with the impurity content, bremmstrahlung radiation also poses a limit for the maximum impurity content of low-Z impurities in the plasma. The energy loss by bremsstrahlung is proportional to Z^2.

- **Line radiation** arises from excitation by electron impact, radiative and dielectric recombination followed by radiative decay of the excited state [13]. Since the bound electrons in the ion shells can only exist in discrete energy levels, the spectrum has a lines structure. It represents a major source of energy loss from the plasma especially in presence of heavy impurities which are not fully-stripped. This poses a severe restriction on the maximum level of impurity concentration that can be tolerated.

- **Recombination radiation** consists of the emission of a photon after the capture of an electron by an ion. Its spectrum is continuous above a threshold energy corresponding to the binding energy of the captured electron.

Based on the described radiation features, the tokamak plasma can be divided into three different regions, figure 3.4:

- **Plasma core**: the hottest region of the plasma. In absence of high-Z impurities, it is dominated by bremsstrahlung. In presence of heavy impurities, such as tungsten, the core can be affected by impurity accumulation [35, 36]. In this case a strong radiation source is located in the core increasing not only bremmstrahlung but also line radiation since heavy impurities are not fully stripped even at those high temperatures. Impurity accumulation often leads to plasma disruption and therefore is unwanted for plasma operation. Accumulation of tungsten and radiative collapse is discussed in detail in chapter 7.

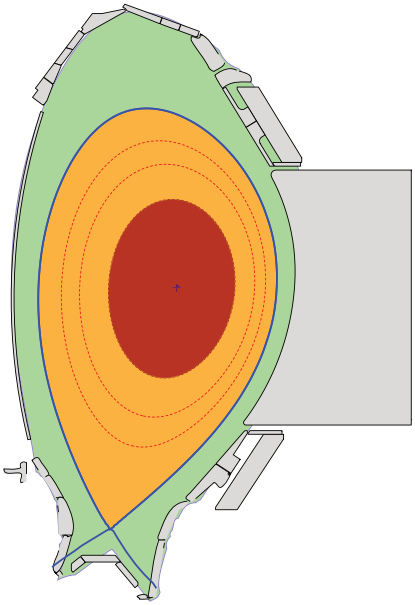

Figure 3.4: Plasma regions based on the different radiation characteristics: in red the core region, in yellow the intermediate zone and in green the SOL and divertor region.

- **Intermediate region**: in this region, which includes the H-mode pedestal, hydrogen and helium are fully ionised, whereas low Z impurities may be partly or fully ionised depending on the plasma temperatures. Therefore line radiation can only be emitted by medium, high-Z impurities and partly ionised low Z impurities. The contribution from bremmstrahlung is also present. The difference with the plasma core region is that more ions contribute to line radiation.
- **SOL and divertor**: this region is characterised by relatively low temperatures between 1 eV and 100 eV. The radiation consists of recombination and line radiation mainly emitted in the ultraviolet (VUV) spectrum. Neutral atoms and ions radiate efficiently most of the power to the divertor walls. In order to reduce high heat fluxes on the divertor tiles, low-Z impurities impurities are introduced in the plasma as explained in the next section.

3.3 Impurity seeding and the power exhaust problem

In order to establish regimes with acceptable confinement and heat loads on the divertor target plates several conditions must be fulfilled simultaneously:

- High edge and divertor radiation to reduce power loads on divertor components;
- Tuned level of core radiation satisfying power exhaust requirements and at the same time avoiding impurity accumulation and central radiation losses;

- Mild ELM activity to exploit their beneficial flush out of impurities but avoiding the power overload problem on the divertor plates;
- Minimise dilution.

A well established technique to control the power fluxes into the divertor is the insertion of low and medium Z impurities into plasma to convert the heat flux to radiation. The portfolio of suitable elements consists of noble gases and nitrogen [37]. The crucial question is: which is the most suitable impurity to radiate in the desired region of the plasma? The atomic data contain the information necessary to determine which impurity is most appropriate to radiate in which region of the plasma.

The radiative loss functions L_Z for seeded impurities as a function of the electron temperature are depicted in figure 3.1 b). It shows that nitrogen has the principal peak at low temperatures typical for divertor conditions ($\approx$ 10 eV), while krypton and argon still radiate significantly at higher temperature. Therefore, N is the most suitable element for SOL and divertor radiation, while Kr and Ar are the best candidates for main chamber radiation. Ar has a more favourable profile with less radiation in the center. However, for a similar radiation level, Kr has the advantage of smaller dilution compared to Ar. While the combination of N and Kr appears the more adequate in current experiments, xenon is also considered as a good candidate for future experiments. Both ITER and DEMO will require high divertor radiation. In ITER high core radiation is not allowed since the heating power (150 MW) is close to the L-H threshold. In DEMO strong core radiation of about $\approx$ 350 MW is foreseen. The combination of divertor and core radiation aims also to maximize the power handling capability which is indicated by the ratio of the power flux through the separatrix and major radius $\frac{P_{sep}}{R}$. In AUG $\frac{2}{3}$ of the value required for ITER $\left(\frac{P_{sep}}{R} = 15\frac{MW}{m}\right)$ has been achieved [38].

Chapter 4

Numerical tools

The radial transport observed on confinement timescales can be modelled with radial transport codes. In this chapter the numerical tools employed in this work to interpret the experimental data and to model the plasma behaviour are presented.

4.1 TRANSP and ASTRA

TRANSP [39, 40] and ASTRA [41] are both time dependent transport codes for the analysis and the modelling of transport of magnetically confined plasmas. Both codes can be used in a predictive or interpretative way. In the predictive approach, the diffusivity terms are calculated self-consistently with kinetic profiles evolving in time and following a given transport model. Sources and sinks must be provided. This approach is used to validate transport models. In the interpretative way, the transport coefficients are computed using the experimental profiles as input. The code inverts the transport equations to infer the transport necessary to match the observed evolution of fluid plasma profiles.

In this thesis, the TRANSP code was used in the interpretative approach to perform power balance analysis (section 2.2 and 8.2.1). The input for the code can originate from experimental data or theoretical models. In the simulations performed in this work the following input were provided time-dependent:

- Toroidal field, plasma current, toroidal loop voltage.
- Injected power for every NBI injector, every ECRH launcher, every ICRH antenna.
- LCFS based on the MHD equilibrium reconstruction given by CLISTE [42].

- Initial condition for the safety factor based on the reconstruction of CLISTE.
- Kinetic profiles.
- Impurity density profiles when available and/or impurity relative concentration.
- Radiation distribution from the non-coronal radiation model developed in this work, see section 6.2. This choice has been motivated by the fact that in TRANSP the impurity charge states are given only in coronall equilibrium. However, as discussed in section 3.1, for low-Z impurities non-coronal effects are important and it is essential to take them into account in order to not underestimate the radiation. Indeed, an important aspect of this work was the inclusion of such effects in the calculation of P_{rad}. The result of these efforts was that, for the first time, TRANSP has been fed with a non-coronal radiated power calculation.

TRANSP contains modules to calculate profiles of heating and current drive sources. For the NBI deposition NUBEAM [43] is employed. NUBEAM is a Monte Carlo package which provides a time dependent description of the particles, the power deposition, momentum transfer, driven current and losses of the neutral beam injection. The evaluation of beam deposition takes into account the full range of atomic processes that affect beam stopping. This makes NUBEAM one of the most accurate codes for the calculation of NBI deposition. In this work, the results provided by the NBI routine in ASTRA were compared with the results obtained with NUBEAM. No significant difference was found for the high radiation scenario discharges. Instead, a discrepancy was found in the pellet discharges (section 8.2.1) during the pellet train when the beam is deposited off axis due to the high density. This feature is well reproduced by NUBEAM, whereas the NBI routine in ASTRA still delivers a rather central peaked profile. This motivated the choice to perform the transport analysis with TRANSP in this thesis.

ASTRA (Automated system of transport analysis) code [41] is characterised by a modular organisation allowing the use of numerous existing routines for analyses of transport processes. Another important feature is the graphical user interface, which allows the user to look at the radial profiles and the time traces at each time step. This way the plasma parameters can be changed and controlled during the simulation enabling the testing of different transport models for heat and particles at run time. This feature, together with the fact that ASTRA is an in-house development, motivated the choice to employ this code for the validation of the radiation and impurity transport model in presence of ELMs, see section 7.

4.2 STRAHL

The 1-D radial transport code STRAHL [44, 45] computes the radial transport of impurities and the associated radiation in the plasma bulk. The conservation law of the particle

density $n_{I,Z}$ of an impurity I in ion stage Z may be written as:

$$\frac{\partial}{\partial t} n_{I,Z} = -\nabla \Gamma_{I,Z} + Q_{I,Z} \tag{4.1}$$

$\nabla \Gamma_{I,Z}$ stands for the flux density of the impurity (the transport term) and $Q_{I,Z}$ for the sources and the sinks of the ion density $n_{I,Z}$. For the flux density $\Gamma_{I,Z}$ a diffusive and convective Ansatz is usually used. Taking the flux surface average leads to the coupled set of radial transport equation:

$$\frac{\partial}{\partial t} n_{I,Z} = \frac{1}{r} \frac{\partial}{\partial r} (D \frac{\partial}{\partial r} n_{I,Z} - \mathrm{v} n_{I,Z}) + Q_{I,Z} \tag{4.2}$$

The term $Q_{I,Z}$ which couples the different ionisation stages via ionisation and recombination reads:

$$\begin{aligned} Q_{I,Z} = -(n_e S_{I,Z} + n_e \alpha_{I,Z} + n_H \alpha_{I,Z}^{cx}) \cdot n_{I,Z} \\ + (n_e S_{I,Z-1}) \cdot n_{I,Z-1} \\ + (n_e \alpha_{I,Z+1} + n_H \alpha_{I,Z+1}^{cx}) \cdot n_{IZ+1} \end{aligned} \tag{4.3}$$

where $S_{I,Z}$ is the ionisation rate of impurity species I in ionisation stage Z, $\alpha_{I,Z}$ is the recombination rate coefficient for radiative and di-electronic recombination and $\alpha_{I,Z}^{cx}$ is the charge exchange recombination coefficients. The first line on the right side of the equation represents the losses of $n_{I,Z}$ due to ionisation $n_e S_{I,Z}$, recombination $n_e \alpha_{I,Z}$ and charge exchange recombination $n_H \alpha_{I,Z}^{cx}$. The second line on the right is the contribution from the lower ionisation stages whereas the third line shows the contribution from the higher ionisation stages.

STRAHL solves the set of couple equations 4.2 for each radial point, time point and ionisation stage. The radial profiles of electron density and temperature are needed to calculate the ionisation and recombination rates and are usually taken from the experiments. The rate coefficients are taken from the ADAS database. The code contains the module NEOART [46–48] which calculates the neoclassical transport for toroidal geometry. Therefore, the neoclassical contributions D_{neo} and v_{neo} can be taken into account. One important feature of NEOART is the inclusion of collisions of the considered impurity with the main plasma ions and all other impurities. In STRAHL, the transport equations are only solved for the ions while neutrals only act as a source for the first ionisation stage. Wall recycling, transport of impurities between divertor, SOL and pump duct are treated with a two chamber model. A sketch of the model is shown in figure 4.1.

The model consists of a valve which introduces the impurities, a wall, a plasma volume

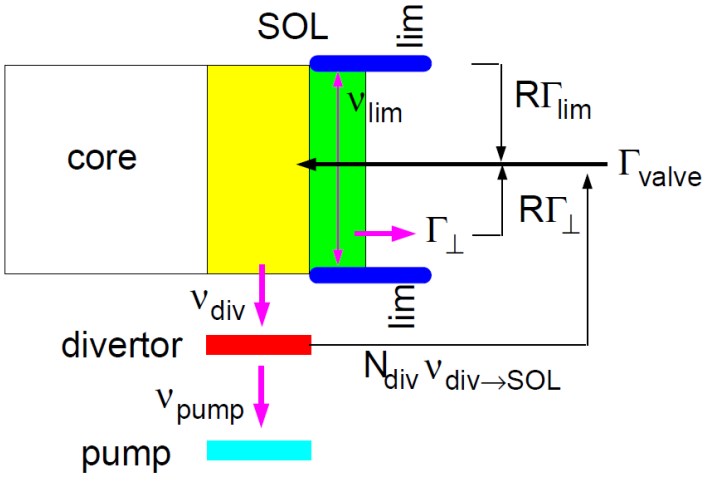

Figure 4.1: Recycling two chamber model used by STRAHL.

which is divided into core and SOL and a divertor volume which is connected to a pump. The transport processes between the SOL and divertor are treated by the Ansatz of empirical loss times. The parallel loss to the divertor is specified by a time constant $\tau_{SOL\rightarrow div}$ which is calculated from the parallel flow velocity and the connection length to the divertor. Depending on their characteristics, particles in the divertor reservoir cause a recycling flux rate $\frac{N_{div}}{\tau_{div\rightarrow SOL}}$ and a rate of pumped particles $\frac{N_{div}}{\tau_{pump}}$. An adjustable recycling parameter R determines the ratio between the recycling fluxes and the fluxes to the wall. At the edge, the recycled neutrals appears as an additional source. R can be set between 0 and 1 where R= 0 stands for non recycling whereas R= 1 stands for complete recycling. The calculation of the radiative emissivity of the impurities is important for this work: radiative recombination, bremmsstrahlung, line radiation and charge exchange contributions can be calculated by specifying rate coefficients from the ADAS database.

4.3 Coupling between ASTRA and STRAHL

The time dependent transport code ASTRA and the impurity transport and radiation code STRAHL have been presented separately. For a detailed time dependent modeling of impurities and radiation, which will be presented in chapter 7, the transport coefficients for all impurities should be calculated during the transport calculations. For such a modeling, an important element is the transport in the edge transport barrier (ETB). Measurements of the impurity transport coefficients in the ETB have shown that between ELMs, the impurity transport coefficients are in agreement with neoclassical theory [30]. This means that in the modeling, a new run of NEOART should be started, whenever the background profiles change considerably. In this way, the correct evolution of D_{neo} and v_{neo} for all impurities is ensured during the whole simulation. This motivated the development of the

coupling between ASTRA and STRAHL [49] which was extended during the course of this work. The coupling of the two codes allows the inclusion of impurities in transport calculations performed with the ASTRA code. In addition ASTRA is coupled to the equilibrium transport code SPIDER [50], which in this thesis is prescribed in fixed boundary mode.

The ASTRA-STRAHL coupling version exhibits a self-consistent interplay between impurity transport, radiation and the heat and particle transport of the background plasma. Information about background profiles (T_e, T_i, n_e) and magnetic equilibrium are transferred from ASTRA to STRAHL which calculates the radiation, Z_{eff} and the impurity density evolution. The output of STRAHL is then used by ASTRA to evolve the background profiles to the next time step as shown in the flow chart 4.2. The turbulent coefficients D_{turb} are set in ASTRA whereas the neoclassical transport is computed in STRAHL using NEOART. ASTRA and STRAHL are run simultaneously at each time step. The time step of ASTRA is 1 ms while the time step of STRAHL is 1μs. The time step of ASTRA Δt_{ASTRA}, and the time step of STRAHL Δt_{STRAHL} are synchronised such that their ratio is an integer number: $\frac{\Delta t_{ASTRA}}{\Delta t_{STRAHL}} = \mathrm{N}$. The radial grid consists of 500 equispaced points for ASTRA and 500 radial points for STRAHL more concentrated in the boundary region where strong gradients in the electron temperature and in the densities of the different ionisation stages are present. ASTRA uses ρ_{tor} as radial coordinate, whereas STRAHL uses ρ_{Vol}. This means that the diffusion coefficient in STRAHL is written as:

$$D_{STRAHL} = D_{ASTRA} \cdot \left(\frac{\partial \rho_{Vol}}{\rho_{tor}}\right)^2 \frac{|\nabla \rho_{tor}|^2}{|\nabla \rho_{vol}|^2} \tag{4.4}$$

Since $\left(\frac{\partial \rho_{Vol}}{\rho_{tor}}\right)^2 \frac{|\nabla \rho_{tor}|^2}{|\nabla \rho_{vol}|^2} \sim 1$, it can be omitted. The coupled version ASTRA-STRAHL is the essential analysis tool used for the predictive-iterative modelling presented in 7.

the radial step size used in the numerical calculations needs to be around 1mm in the boundary region, while in the central part of the plasma a grid resolution around 1 cm is usually sufficient. It is advantageous to change the radial grid spacing from centre to edge in order to keep the number of radial mesh points as low as possible.

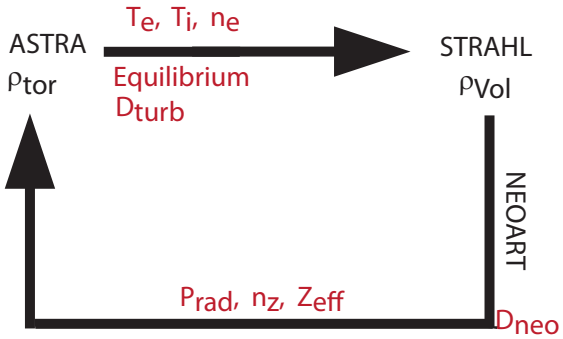

Figure 4.2: Flow chart of the coupling between ASTRA and STRAHL.

Chapter 5

Experimental framework

5.1 The ASDEX Upgrade tokamak

This work is based on data collected at the ASDEX Upgrade tokamak, Garching, Germany. ASDEX Upgrade (Axial Symetric Divertor Experiment Upgrade) is a medium sized tokamak with a divertor configuration and a full tungsten wall. It has been operated by the Max Planck Institute for Plasma Physics since 1991. AUG was transformed in stages from carbon into a tungsten device (1999-2006). In 2007 it demonstrated successful H-mode operation with a full-W wall, the first tokamak to do so [51]. This is of particular importance since future devices will have to operate with high-Z plasma facing components (PFC) in order to simultaneously handle the high thermal loads and avoid retention of tritium observed for carbon PFC.

ASDEX Upgrade has flexible plasma shaping possibilities and all heating systems foreseen for ITER. The elongated plasma geometry similar to the ITER design shape, the powerful heating capability together with the all-W wall allows to investigate aspects of ITER's plasma operation. This makes ASDEX Upgrade well-suited for studies of high performance plasmas and power exhaust by impurity seeding. Several impurities can be injected in AUG through valves located in the divertor and the mid-plane. The device has a major radius R_0 of 1.65 m and a minor radius a of 0.5 m. The plasma current is in the range of 0.6-1.4 MA, the toroidal magnetic field B_t, created by 16 toroidal field coils, is typically -2.5 T. The pulse length is around 10 s, which is a multiple of the global energy confinement time τ_E $\sim$100 ms. ASDEX Upgrade is equipped with a large number of diagnostics measuring a wide range of plasma parameters. The most important diagnostic and heating systems used in this work are presented in the following sections.

5.2 Heating systems

The aim of auxiliary heating systems is to raise the plasma temperature towards the required values of fusion reactions. Besides ohmic heating from the plasma current inherently present in tokamak, three different auxiliary heating systems are available at AUG: the neutral beam injection (NBI) with 20 MW, the electron cyclotron resonance heating (ECRH) with a source power of 6 MW and the ion cyclotron resonance frequency heating (ICRF) with a source power of 8 MW. This work focuses on the investigation of high radiation scenarios which require operation at relatively high power. Thus, typically all three auxiliary system have been employed.

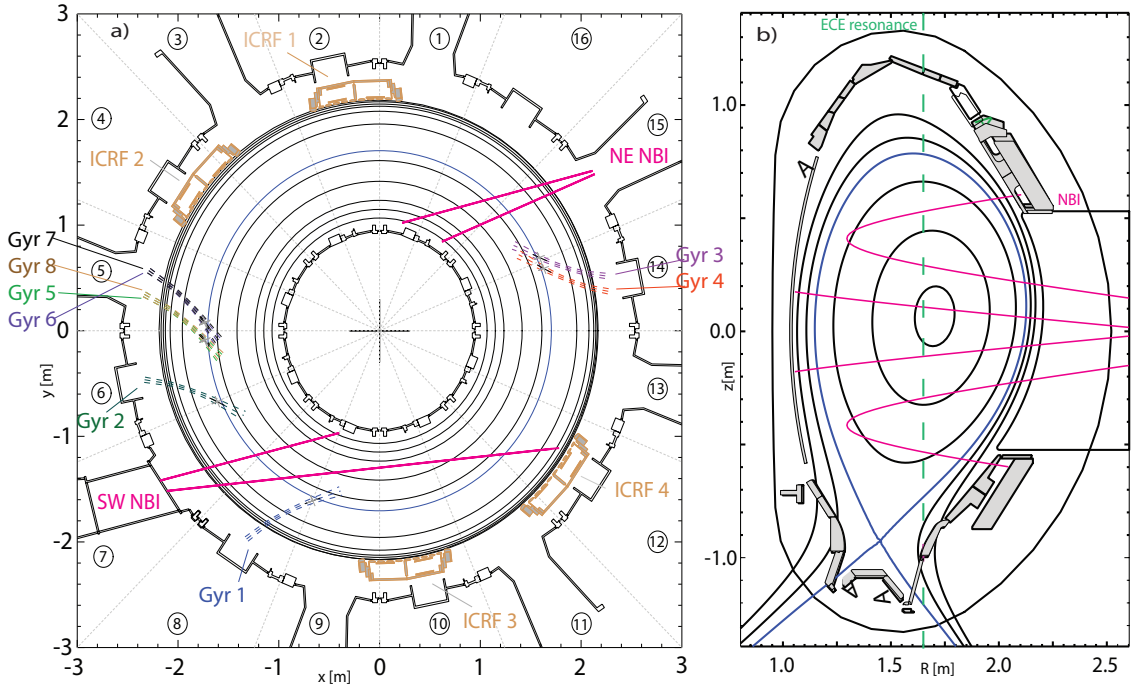

Figure 5.1: a) Toroidal and b) poloidal cross section of ASDEX Upgrade with the used heating systems.

5.2.1 Neutral beam injection

The NBI heats the plasma by transferring energy from fast particles to the plasma, typically deuterium as used in this work. Alternatively, hydrogen or helium can be used. The ion beam is accelerated by means of high voltage and directed towards the plasma after neutralisation of the fast ions by collisions with neutral hydrogen gas [52]. As the neutral beam passes through the plasma, the fast neutrals are ionised by three collisional processes: charge exchange; ionisation by ions and ionisation by electrons. The ions are

trapped gyrating around the magnetic field lines. They are slowed down to thermal energy by collisions with the plasma, transferring their energy and heating both electrons and ions. The fraction of power deposited in each species is dependent on the initial beam energy and the plasma temperature and is typically 50:50. At ASDEX Upgrade, the NBI system consists of two injectors, each with 4 neutral beam sources at 2.5 MW output power. The set up of the two injectors is similar, but due to different currents and extraction voltages, neutrals from injector 1 have a full injection energy of 60 keV, while those from injector 2 have 93 keV in order to achieve better penetration and current drive. The path of the beams are shown in figure 5.1. In general, the NBI deposition profiles for both electrons and ions are broad and span the entire plasma radius. The electron deposition profile is rather flat whereas the ion profile is peaked in the centre. The computation of the deposition profile of the NBI power has been calculated in this work time dependent with the NUBEAM code inside TRANSP (section 4.1).

5.2.2 Electron cyclotron resonance heating

Radiofrequency heating is based on transferring energy to the plasma by electromagnetic waves. In the case of electron cyclotron resonance heating [53] the electron cyclotron frequency and its harmonics are used. The electron cyclotron frequency is the frequency with which the electrons gyrate around the magnetic field lines:

$$\omega_{c,e} = \frac{e \cdot B_{tot}}{m_e} \tag{5.1}$$

where e is the elementary charge, B_{tot} the magnetic field and m_e the electron mass. It depends on the magnetic field which decreases with $\frac{1}{R}$ from the center to the edge in tokamaks. Hence, the ECRH deposition is localised because the waves are only resonant at a given magnetic field. At ASDEX Upgrade the electrons are heated using the second harmonic in X-mode. The microwaves are generated by gyrotrons and are guided to the vacuum vessel by oversized wave-guides. The launched waves accelerate the resonant electrons which transfer their energy through collisions with the plasma electrons. At AUG waves are launched at a frequency of 140 (or 105) GHz. With a typical B_t= -2.5 T, the ECRH deposition is close to the magnetic axis. Characteristics of the ECRH are its local power deposition well suited for central heating and the fact that it heats only the electrons. As for the ECE diagnostic, "the cutoff density" (see section 5.3.4) represents an operational limit for the ECRH system. This is the reason for which in the pellet discharges presented in chapter 8, the ECRH had to be switched off before the injection of the pellet train due to the resulting high densities. The ECRH at AUG consists of 2 gyrotron systems. The first system has 4 units, gyrotron 1-4, each one able to deliver up to 400 kW for 2 seconds. The second system has 4 gyrotrons (gyrotron 5-8) which can deliver 1 MW each and operate at both 105 GHz and 140 GHz for 10 seconds. The injection angles can be varied toroidally and poloidally. At AUG, it is calculated using

the beam tracing code TORBEAM [54].
The ECRH is particular relevant at AUG because its centrally localised heating enhances the radial outward transport of heavy impurities, in particular tungsten, preventing their accumulation in the plasma core [55, 56].

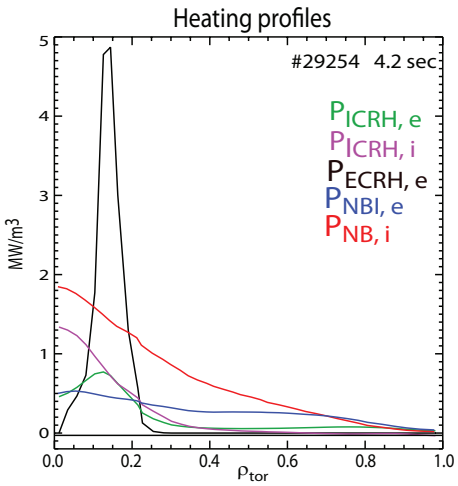

Figure 5.2: Example of power deposition profiles for one of the analysed discharge from TRANSP: in green ICRH to the ions, in magenta ICRH heating to the electrons, in black ECRH to the electrons, in blue NBI heating to the electrons, in red NBI heating to the ions.

5.2.3 Ion cyclotron resonance heating

The ion cyclotron resonance heating [57] exploits the ion cyclotron frequency and its harmonics to heat the plasma. The ion cyclotron frequency is given by:

$$\omega_{c,i} = \frac{Z \cdot e \cdot B_{tot}}{m_i} \tag{5.2}$$

Z stands for the ion charge numbers and m_i for the mass of the minority ions. The waves lie in the frequency range of 30-120 MHz and are coupled via large antennas to the plasma. As for the ECRH, the locations of these resonances depend on the magnetic field strength. At AUG the minority scheme is generally used. In this scheme, the fast wave transfers its energy mainly to the minority ions and fast ions are produced in the plasma. Similarly to the fast ions of the NBI, they build a tail in the distribution function and thermalise by Coulomb collisions with electrons and ions. The ICRH system at AUG consists of four generators with an output power of 2 MW each connected to 4 antennas. They are located near the equatorial plane on the low field side (figure 5.1). At AUG, the ICRH is principally used to accelerate the hydrogen minority present in deuterium plasmas at a frequency of ∼36 (30) MHz with a typical B_t = -2.5 (2.0) T [58]. The ICRH

typically heats the innermost on-axis 15 cm of the plasma in both the electron and ion channel. The broadness is in between the NBI and ECRH deposition profile. The ICRH power deposition used in the modelling part of this work has been calculated with TORIC inside TRANSP [58].

The comparison of the typical power deposition profiles of NBI, ECRH and ICRH to the electrons and ions for one of the analysed discharges is illustrated in figure 5.2.

5.3 Diagnostics

ASDEX Upgrade is equipped with more than 70 different diagnostics. This section introduces various diagnostics which have been used for the analysis of plasma discharges in this work.

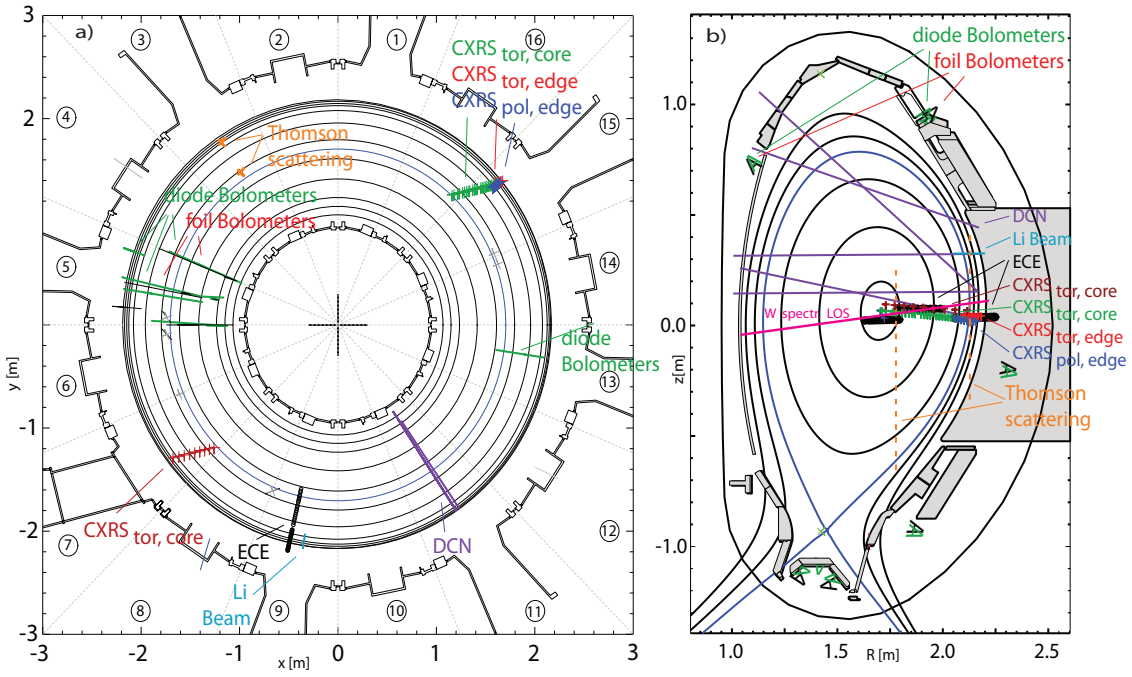

Figure 5.3: a) Toroidal and b) poloidal cross section of ASDEX Upgrade with the used diagnostics.

5.3.1 Interferometry

Interferometry is a well established method to measure density in fusion plasmas. Its principle is based on the phase shift of an electromagnetic wave passing through the plasma. In ordinary mode its refractive index is given by:

$$N = \sqrt{1 - \frac{\omega_p^2}{\omega^2}}; \qquad \text{with} \qquad \omega_p = \sqrt{\frac{e^2 \cdot n_e}{\varepsilon_0 \cdot m_e}} \tag{5.3}$$

If the frequency of the electromagnetic wave, ω, is much higher than the plasma frequency ω_p, the phase shift between a beam of coherent radiation (laser) propagating through the plasma and a reference beam propagating in the vacuum is proportional to the electron density integrated along the beam probing the plasma [13]:

$$\varphi = \frac{\lambda_0 e^2}{4\pi\varepsilon_0 m_e c^2} \int_0^l n_e(x)dx = \lambda_0 r_e \int_0^l n_e(x)dx \tag{5.4}$$

$\lambda_0 = \frac{2\pi c}{\omega}$ stands for the vacuum wavelength and $r_e = \frac{e^2}{4\pi\varepsilon_0 \cdot m_e \cdot c^2} \approx 2.82 \cdot 10^{-15} m$ for the classical electron radius.

On one hand, long wavelengths are favorable to maximise the density resolution. On the other hand, perturbing beam refraction by density gradients increases with λ^2 and phase counting errors, so-called fringe jumps, can occur when the total phase shift exceeds 2π as explained later. In ASDEX Upgrade the phase shift is measured with a Mach-Zehnder-type heterodyne interferometer, which works as follows (figure 5.4 a)): The beam from a laser is split into two components using a beam splitter. One of this is shifted in frequency by $\triangle\omega$ using a blazed optical grating where $\triangle\omega$ is proportional to the rotational speed of the disc [59]. The other component is subdivided further (by another beam splitter) into a reference beam and a probe beam. The shifted beam is combined on one side with the reference signal and on the other side with the probe signal. Both the reference detector and the probe detector receive the superposition of the two light waves with frequencies ω and $\omega + \triangle\omega$. The beat signal may be written as [60, 61]:

$$\begin{aligned} A_1 \cdot \sin(\omega t + \varphi) + A_2 \cdot \sin((\omega + \triangle\omega)t) &= (A_1 - A_2) \cdot \sin(\omega t + \varphi) \\ &+ 2A_2 \cdot \left(\frac{2\omega + \triangle\omega}{2} t\right) \cdot \cos\left(\frac{\triangle\omega}{2} t - \frac{\varphi}{2}\right) \end{aligned} \tag{5.5}$$

The detectors are not sensitive to optical frequencies $\left(\omega, \frac{2\omega+\triangle\omega}{2}\right)$, but only register the slow $\left(\frac{\triangle\omega}{2}\right)$ beat signal, which contains the desired phase information. The first term indicates that the two amplitudes A_1 and A_2 are different resulting in a constant offset at the output of the detector. The beat frequency limits the time resolution of the interferometer. To have a good time resolution the beat frequency is usually in the range of 10 kHz up to 1 MHz limited by the maximum disc rotation speed. The DCN beat signals at AUG have

a frequency of 10 KHz. The comparison between the phase of the two beat signals at the output of the two detectors gives the line-integrated density. Because of the cosine dependence of the detector signal it is not possible to determine unambiguously whether the phase difference is φ or φ+n $\cdot 2\pi$. Hence, multi-radian phase detectors are used to count all transitions of the beat signal from one period to the next. This implies a monitoring of the density evolution from the beginning of the discharge making the measurement historically dependent [61]. In presence of density changes faster than the time resolution, counting errors by multiples of 2π, can affect the measurement. These errors are known as "fringe jumps". In post-discharge analysis a quick criterion to identify fringe jumps is to check whether the measured phase does not return to zero. If this is the case then it is clear that at least one fringe jump occurred. However, several fringe jumps can occur whose amplitudes sum up to zero making the detection more complicated.

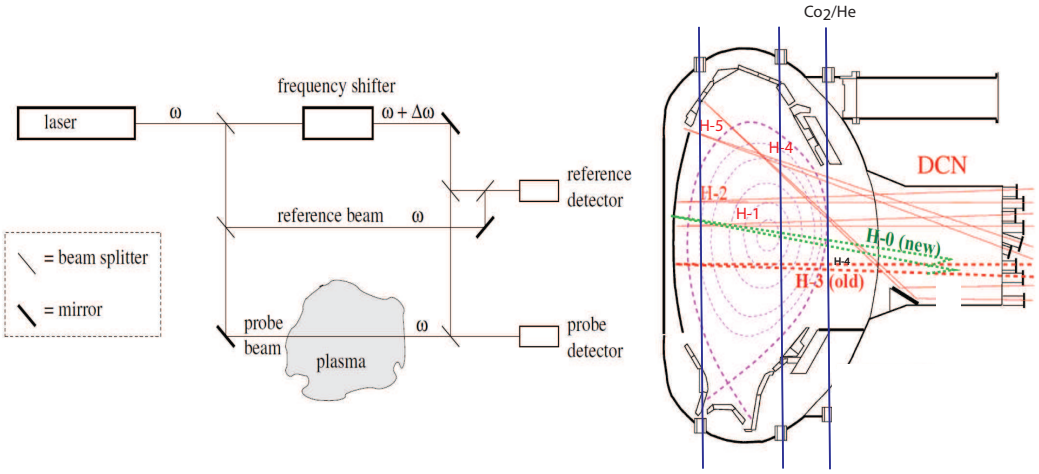

Figure 5.4: a) Overview of the Mach-Zehnder interferometer; b) The three vertical lines of sight of the CO_2/He interferometer (blue) and the 5 lines of sight of the DCN (red). The replacement of H-3 with H-0 (green) is also shown (adapted from [61]).

The interferometry system of ASDEX Upgrade consists of a λ_0 = 195 μm DCN interferometer with five horizontal lines of sight and a 10.6 μm / 633 nm two-color CO_2/HeNe interferometer with three vertical channels. The three vertical channels are named V-1, V-2, V-3, however only two of them can be operated simultaneously. Until 2013 the geometry of the DCN consisted of three horizontal channels H1- H3 parallel to the midplane and two lines of sight crossing the plasma transversally, H-4, H-5. H-5 is referred to as edge line integrated density and H-1 used to be referred as core line integrated density (although it was not exactly crossing the plasma centre). The channels H-2 and H-3 were situated symmetrically around the plasma centre giving a redundant information, whereas no measurement in the very center of the plasma was available. Hence, H-3 was redirected through the centre and renamed H-0. The lines of sight are shown in figure 5.4 b). The line averaged density of the plasma in m^{-3} is defined as the measured line integrated density in m^{-2}, divided by the length of the laser path inside the confined plasma [60]. At the wavelength of the vertical interferometer, beam refraction due to density gradients is not an issue but its high noise level together with the limited number of lines of sight

render the DCN measurements preferable. On the contrary, the wavelength of the DCN is sensitive to beam refraction and fringe jumps sometimes affect the measurements heavily (see appendix A).

5.3.2 Thomson scattering

Electron temperature and density at AUG can be measured with the Thomson scattering (TS) diagnostic [62, 63]. It is based on the radiation as Hertz dipole of particles in the plasma after interaction with an injected laser. The movement of the electrons due to their temperature result in a Doppler broadening of the laser frequency. If the electrons are in thermal equilibrium, the spectrum of the scattered light has a gaussian shape. The width of the gaussian provides information on the electron temperature. The intensity of the scattered radiation is proportional to the laser light intensity and to the electron density following the formula [23]:

$$I_{TS} \propto n_e \sqrt{\frac{m_e}{2\pi \cdot T_e}} \cdot e^{-\frac{m_e v^2}{2k_B \cdot T_e}} \tag{5.6}$$

Therefore, a single measurement provides n_e and T_e at the same position. This has the advantage that the profiles are radially aligned and they can be used to realign profiles from other diagnostics. The radial position of the laser beam and the vertical location of the scattering zones determines the measurement locations. Typically the detectors are located at a scatter angle of 90°. At ASDEX Upgrade simultaneous measurements of the core and edge parameters are possible thanks to a recent upgrade of the TS system [63]. Four vertical Nd-YAG laser beams are used for the core and six for the edge system. Each laser emits an energy of the order of 1 J per pulse, with a pulse duration of 15 ns and a repetition rate of 20 Hz. This yields a snapshot of the profiles every 12.5 ms for the core and every 8 ms for the edge. The measuring locations of the TS are shown in figure 5.3.

5.3.3 Lithium beam emission spectroscopy

Lithium beam impact excitation spectroscopy (LIB) [64] is based on the measurement of Li radiation $Li_I(2s-2p)$ at 670.8 nm produced by lithium atoms injected in the plasma by a lithium beam. The lithium neutrals are excited and ionised by collisions with electrons. The measured line emission intensity is dependent on the electron density and the local intensity of the beam. The beam is attenuated due to ionisation and charge exchange with the background plasma particles, which limits the use of this diagnostic to the plasma edge(typically $\rho_{pol} > 0.95$). A full collisional-radiative model is employed to model the measured spatial line emission profiles. At ASDEX Upgrade lithium neutrals are injected

horizontally into the plasma 30 cm above the mid plane from the low field side with injection voltages of up to 60 keV. The diagnostic is equipped with 35 LOS which cover the entire SOL and roughly the outermost 5 cm of the confined region depending on the separatrix position. The radial resolution of 0.5 cm is determined by the the aperture of the optical setup. The background radiation is subtracted from the measured signal by chopping the Li beam periodically, 56 ms on and 24 ms beam off [65]. However, for studies of fast events such as ELMs, the measuring frequency can be increased up to 2 kHz. The location of the lithium beam diagnostic is shown in figure 5.3.

5.3.4 Electron Cyclotron Emission spectroscopy

Electron cyclotron emission spectroscopy (ECE) [13] is a passive technique which measures the cyclotron radiation emitted by electrons while gyrating around the magnetic field lines. This radiation occurs at discrete angular frequencies $\omega = n\omega_{ce}$ with n being the harmonic number. The frequency ω_{ce} is proportional to the strength of the magnetic field which decreases with $\frac{1}{R}$ determining the location of the emitted radiation. In tokamaks, the main part of the plasma is generally optically thick for electron cyclotron radiation. The intensity I of the emitted radiation is proportional to the electron temperature (black body radiation) and it can be described by the Rayleigh-Jeans law [13]:

$$I_{RJ} = \frac{\omega^2}{8\pi^3 c^2} T_e \tag{5.7}$$

Accordingly, from the spectral radiance at the corresponding frequency, the radial profile of the electron temperature along the line of sight can be obtained. The evaluation is based on the assumption that the velocities take a Maxwellian distribution while the frequency shifts due to relativistic and Doppler effects are neglected. However, at low density, especially at the plasma edge of H-modes, the plasma becomes optically thin and the observed radiation temperature is not anymore equal to the local electron temperature [66]. This phenomenon is known as "shine-through". The ECE measurements are not only limited by this effect but also by the so-called cutoff density [67].

For extraordinary modes (X-mode) as in AUG, the maximum density at which T_e can be measured is $1.2 \cdot 10^{20}\mathrm{m}^{-3}$ for B_t= 2.5 T. In regions where the electron density is larger than the cut-off density no electron cyclotron emission can be measured. This is the reason why for high density experiments presented in chapter 8 only measurements from the Thomson scattering diagnostic are available. At ASDEX Upgrade the ECE system is a multichannel heterodyne radiometer. It measures the second harmonic extraordinary mode (X-mode) at 60 different positions in the frequency range from 89 GHz to 187 GHz. The diagnostic has a sampling rate of up to 1 MHz which allows to resolve fast electron temperature changes, occurring for instance during ELM crashes.

5.3.5 Integrated data analysis

Integrated data analysis (IDA) has been developed at ASDEX Upgrade with the aim of estimating the electron temperature and density through a combination of several diagnostics in the framework of the Bayesian probabilistic model [68]. The use of the Bayesian probability theory allows the inclusion of the so-called prior information and weighting of the data with the corresponding measurement errors. The standard application of IDA combines data from ECE and optionally TS for the temperature measurements. LIB and DCN are used for the density evaluation with optional inclusion of TS. Since there is no information from the plasma core, the profiles are extrapolated quadratically using the gradient of the profile at the last measurement channel and the fact that the profile gradient has to become zero at ρ_{pol}= 0. The time resolution is limited by the time resolution of the LIB diagnostic which is of the order of 1 ms or by the TS resolution. In this work IDA has been used to obtain electron temperature and density profiles to insert into TRANSP for the transport calculations. In addition, the density profiles obtained with IDA have been used to validate the reliability of the fringe jump corrections made to the DCN data especially during large perturbations induced by pellets. This part will be discussed in the appendix A.

5.3.6 Charge exchange recombination spectroscopy

Charge exchange recombination spectroscopy (CXRS) is routinely used in tokamaks to measure ion temperature, toroidal rotation and impurity densities. The diagnostic is based on charge exchange collisions between neutrals and fully ionised impurity ions in the plasma, which are in thermal equilibrium with the main ion species [69]:

$$A^{Z+} + D^0 \rightarrow A^{(Z-1)+*} + D^+ \rightarrow A^{(Z-1)+} + h\nu + D^+ \tag{5.8}$$

Ionised impurities undergo a charge exchange reaction with neutral deuterium atoms from the NBI beam.During the charge exchange an electron is transferred from a neutral D atom to an impurity ion which is generally in an excited state. Line radiation is emitted during the de-excitation of the impurity ion. In ASDEX Upgrade the neutral atoms are provided by the NBI and therefore the optical system is aligned along the heating beams [69]. The light emitted due to charge exchange reactions provides localised information on the fully ionised impurity ion because it arises from the intersection of the line of sight with the neutral beam. The Doppler width of the spectral lines yields the temperature of the impurity ion, the Doppler shift provides the velocity along the line of sight. Impurity densities are inferred from the radiance of the measured spectral line knowing the neutral density n_0. Depending on the impurity content, typically emission lines from low-Z impurities such as boron, carbon or nitrogen are analysed.

ASDEX Upgrade is equipped with 4 charge exchange systems: 2 core systems CEZ and CHZ with a radial resolution of ± 2.5 cm and two edge systems, one toroidal (CMZ) and one poloidal (CPZ). The toroidal and poloidal positions of the systems are shown in figure 5.3. The toroidal core system CHZ looks at beam 8, it has an integration time of 20 ms and in this work it has been used to infer the carbon concentration when the CEZ system (integration time of 5-10 ms) was measuring nitrogen. The three other systems look at beam 3. Both edge systems with 8 LOS are installed at the low field side and have a temporal resolution of up to 2.2 ms. They can resolve the pedestal of AUG with a radial resolution of 1cm. In this work the ion temperature has been obtained by combining the data provided by the core and the edge systems into one single profile. The impurity concentrations have been used to calculate and model the radiation. Helium can also be measured at AUG with a core CXRS diagnostic (CAZ) looking at beam 3 with 15 lines of sight, part of the ITER-prototype CX spectrometer [70].

5.3.7 Bolometry

In fusion devices, bolometers are used to measure the total radiated power from visible light to the soft X-ray region. Bolometry is a crucial diagnostic because radiation represents a significant fraction of the power balance in tokamak. To measure absolutely calibrated values of radiation, at ASDEX Upgrade detectors are installed in the vacuum vessel using pinhole cameras [71]. Two different bolometry systems are available: foil bolometers and diode bolometers. The first consist of 4.5 μ absorbing foils of chemically inert material such as platinum and gold, located above an isolating substrate. They work by detecting the temperature rise of the material due to the energy deposited by photons. The foils absorb all photon energies, therefore the measurement can be absolutely calibrated. The system has 112 LOS installed in 6 pinhole cameras which are mounted at different poloidal locations in the vessel as is shown in figure 6.1 in section 6.1. Since the measurements are line integrated, a tomography reconstruction or Abel inversion is required to retrieve a 2D radiation distribution. Details about the tomography reconstruction are presented in section 6.1.

Various examples of tomography obtained in the course of this work are presented in chapter 6 . The time resolution of the foil bolometers is in the range of a few milliseconds and is set by the finite time the heat is diffusively transported through the foil [72]. However, many events such as ELM-induced radiation take place on a much shorter time scale. Therefore a complementary system is needed. In 2010 diode bolometry, characterised by a time resolution of a few microseconds, was installed [73]. The diagnostic principle relies on the photocurrent generated by AXUV (Absolute eXtreme UltraViolet) photodiodes which is proportional to the incident radiation. The diodes offer a better time resolution than foil bolometers but they are not absolutely calibrated and they lack of sensitivity [72]. The diode set up at AUG consists of 256 LOS installed in eight different cameras which cover the full poloidal cross section of AUG. Their high spatial resolution together with a very high time resolution of 54 μs makes them suitable to study fast radiation effects

which cannot be resolved by foils bolometers. The toroidal and poloidal positions of the foils and diodes are shown in figure 5.3. In this work diode bolometers have been used to measure the ELM-induced radiation during nitrogen seeding experiments and to validate the diffusive and convective ELM radiation models presented in chapter 7.

5.3.8 Tungsten diagnostic

Due to its radiation properties, the maximum allowed tungsten concentration in the plasma core is of the order of 10^{-5}. Hence, it is crucial to be able to measure and control the tungsten concentration in the plasma. Determining the W concentration is not an easy task because the W spectrum spans over a wide wavelength range (from visible to X-ray) with hundreds of spectral lines at similar wavelengths due to the high recombination rate. At ASDEX Upgrade the tungsten concentration is derived from X-ray and VUV spectroscopy [74]. Depending on the electron temperature, two radially separated measurements are routinely available. In the spectral range around 5 nm a compound emission of hundreds spectral lines emitted by ion stages between W_{27+} and W_{35+} forms the envelope of the quasi-continuum radiation. From the measurement of this structure the W concentration in a T_e range of 0.5-1.7 keV is determined.

The emission of Ni-like W_{46+} at 0.793 nm is employed to deduce the W concentration in a T_e range of 2.1-5.5 keV. Figure 5.3 shows the line of sight of the grazing incidence spectrometer. The line is close to the midplane and crosses the plasma horizontally in the poloidal plane (see figure 5.3). This ensures that the measurement includes the emission from the center of the plasma. In this work the tungsten density is used to calculate and model the radiation due to W.

Chapter 6

High radiation experiments

Impurity seeding is an essential element of the power exhaust in tokamaks used to increase radiation. It is usually employed to limit power loads on machine components (see section 3.3). Such a technique is already required in present tungsten machines operating at high power levels and is extensively investigated in view of future reactors for which it will be mandatory. In ASDEX Upgrade divertor cooling by nitrogen seeding has been achieved (see e.g. [75]). A confinement increase due to the presence of nitrogen has been discovered [76, 77]. During the 2012 - 2014 AUG operational campaigns the high radiation scenario has been extensively explored not only by means of nitrogen seeding, but also by injecting medium-Z impurities to radiate in the main chamber and assess the possible impact of central radiation. In this chapter the effects of impurities on plasma performance are investigated. These span from the negative effects of impurity accumulation in the plasma core and radiative collapse, to positive effects such as reduction of the power flux into the divertor; the reduction of ELM size and the improvement of confinement via reduced core transport and/or improved pedestal top values combined with profile stiffness. An introduction to the tomographic method used to retrieve the 2D radiation distribution and the development of a non-coronal radiation model are presented in section 6.1 and 6.2. Section 6.3 introduces the experimental set up of the high radiation experiments. The analysis of the radiated power and the transport properties of H-modes seeded with nitrogen-only and nitrogen combined with krypton are presented in section 6.4.1 and 6.4.2. Since future reactors will contain helium ash, the impact of helium on transport and confinement has also been investigated and results are shown in section 6.4.3. Finally an overview of the parameter dependencies of confinement based on data collected during this work is presented in section 6.5.

6.1 Tomography reconstruction

Bolometers measure the radiated power integrated along their lines of sight (see section 5.3.7). In order to extract as much information as possible from these measurements, 2D tomographic methods [78], which invert the line integrated measurements on a numerical spatial grid, are usually used. However, due to the finite number of LOS, the reconstruction of 2D profiles requires additional information: at AUG it is assumed that the gradients of the emissivity perpendicular to the flux surfaces are higher than those parallel [73]. Additionally, different gradients for different plasma regions such as the confined plasma, the SOL, inner and outer divertor and the X-point can be used and varied to optimise the reconstruction. The tomography algorithm minimises the error χ^2 between the measured signal and the actual reconstructed profile with a regularization integra describing the curvature of the 2D profile [73]. In the present work such a method was used to reconstruct the 2D experimental radiation profile which has been compared with the calculated radiation profile using atomic data (see section 6.2).

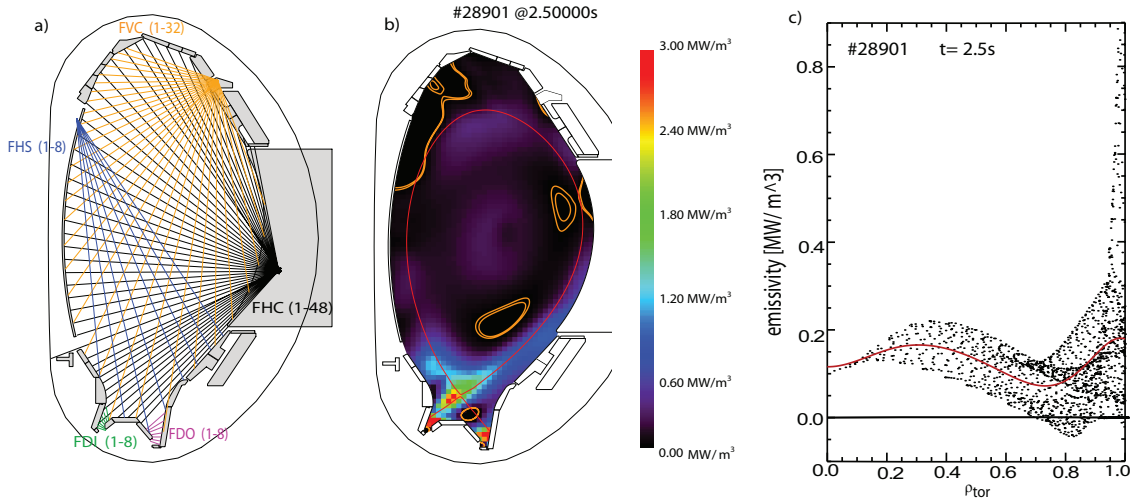

Figure 6.1: Cross section of ASDEX Upgrade: a) Lines of sight of the cameras used for the tomography reconstruction in this work, b) 2D poloidal emissivity distribution, c) Corresponding radial emissivity profile.

Figure 6.1 a) shows a cross section of ASDEX Upgrade with the lines of sight of the foil bolometer cameras used in this work for the tomography reconstruction. In panel b) an example of a 2D poloidal emissivity distribution is depicted where some artifacts are visible (orange spots). These artifacts represent zones of negative radiation which are unphysical. The code utilises them in order to avoid a higher reconstructed brightness than the one actually measured. They are a sign of a non optimal reconstruction but they can be minimised choosing appropriate parallel and perpendicular gradients locally in the different plasma regions. Panel c) shows the radial profile of the emissivity obtained by mapping the 2D poloidal deconvolution on a radial grid. The black points are the points of the deconvolution while the red line represents the spline fitted radial profile. The spread of the points at one radial position arises from the poloidal asymmetry of the emissivity.

The very edge ($\rho_{tor} > 0.9$) is affected by large uncertainties and therefore values here are unreliable. An example of a 2D radiation distribution before and after nitrogen seeding is depicted in figure 6.2. Before nitrogen seeding (panel a)), no strong radiation in the main plasma is detected, only rather weak radiation in the divertor region exists. During nitrogen seeding, an increased radiation in the SOL and a very localised radiation in the divertor is found (panel b), (see also section 3.3). However, the edge radiative ring is not well resolved. With light impurities, as used in this work, the radiation is higher at the edge and the reconstruction is difficult. The radiative ring in the core region is an artifact of the tomography reconstruction which is attributed to the limited spatial resolution of the bolometry. If excessive radiation is detected in the divertor, the tomography algorithm redistributes the radiation over the main chamber to minimise the curvature and a ring appears also in the centre even if no tungsten accumulation is present. Figure 6.2 b) illustrates that lines of sight of the vertical cameras looking into the divertor also cross at the plasma core. Hence, divertor and main chamber reconstruction are "coupled". All these uncertainties in the bolometry reconstruction suggest that a modelling of the radiation is required. This is presented in the next chapter.

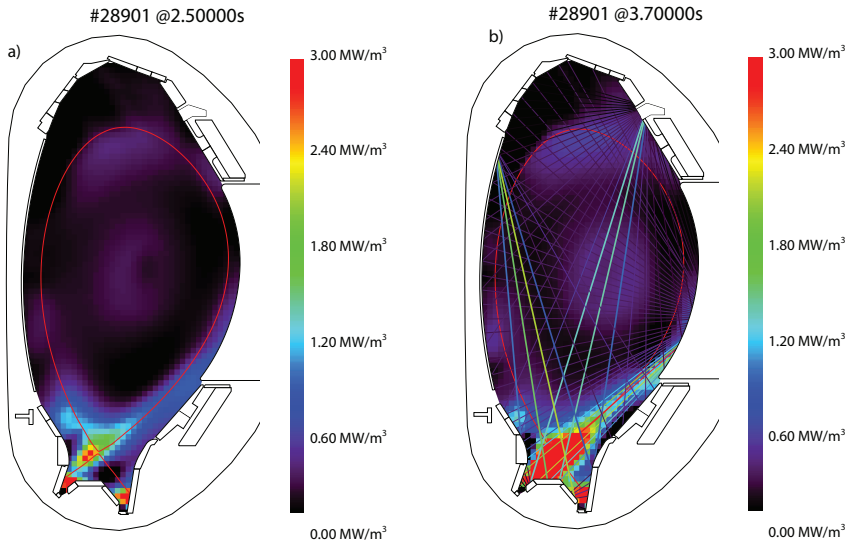

Figure 6.2: Tomography reconstruction: a) before N seeding, b) during N seeding.

6.2 Development of a non-coronal radiation model

In section 3.1 it was shown that if the transport processes are sufficiently slow, the ionisation stages of the impurities are in equilibrium corresponding to the plasma temperature. This coronal equilibrium occurs in the plasma core. Corrections must be made if transport plays a role and this equilibrium is not reached, as happens at the plasma edge. In this work a non-coronal radiation model was developed and assessed by comparison with

bolometric measurements in order to provide a reliable radiation profile for transport calculations. The model was dubbed *PIRT* which stands for "Pedestal Impurity Residence Time". In the PIRT model the enhanced radiation due to non-coronal effects is described using the parameter $n_e \cdot \tau$ already introduced in section 3.1, such that L_Z depends on both T_e and $n_e \cdot \tau$. In the ionisation phase the radiation increases as τ decreases.

In the calculation of the radial profiles of L_Z for each impurity, T_e and n_e are taken from the experimental profiles whereas τ is prescribed according to the following arguments. In the pedestal, the ELMs flush out impurities and cause a reorganization of the profiles at every crash. Therefore, the residence time at the pedestal cannot exceed the inverse of the ELM frequency $\frac{1}{f_{ELM}}$. This assumption takes into account not only the residence time of the impurities but also the recovery of the pedestal profiles after the crash, as well as the possible impurity influx during this phase. Furthermore, an appropriate function for τ must depend on the radius and satisfy two conditions: 1) in the core τ must be large to reflect the coronal equilibrium ($n_e \cdot \tau = 10^{22}$ m^{-3} ms) and 2) in the edge region it has to decrease to a small value, τ_{ped}. The hyperbolic tangent fulfils these constraints and is used in this work. A good agreement with the experimental radiated power is achieved using the following formula:

$$\tau = 100 \cdot (-tanh(k \cdot (\rho_{tor} - \rho_{crit})) + \frac{1}{2}) + \tau_{ped} \tag{6.1}$$

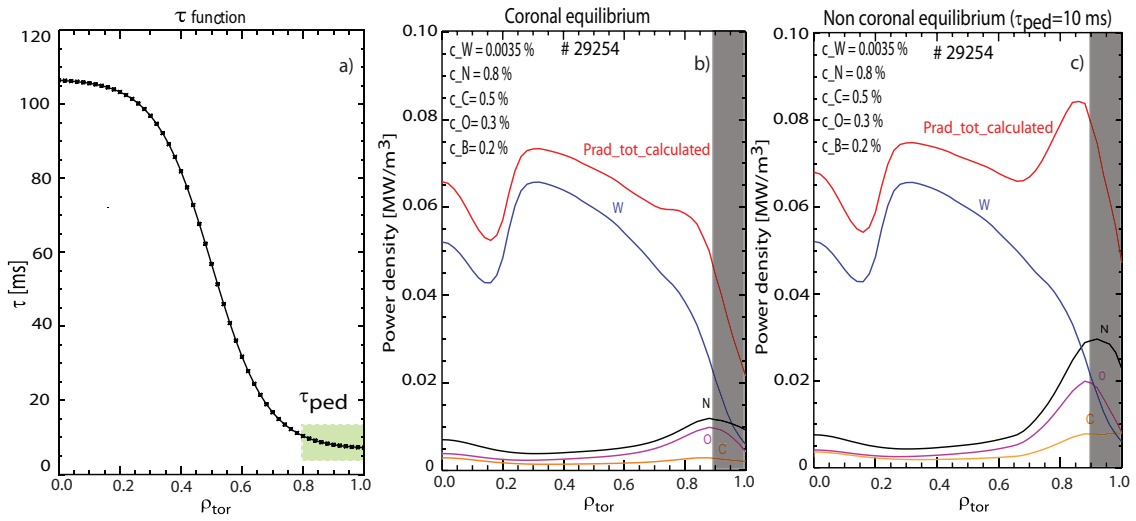

Figure 6.3: a) The hyperbolic tangent as a function for the impurity residence time τ in the PIRT model. Prediction of the radiated power density: b) coronal conditions, c) non-coronal conditions. Calculated radiated powers of carbon (orange), oxygen (magenta), nitrogen (black) and tungsten (blue). The sum of the radiated powers, $P_{rad,tot}$, is shown in red. The comparison shows that if the non-coronal effects are neglected, the radiated power at the edge is significantly underestimated.

The shape of τ can be seen in figure 6.3 a). In the formula the factor 100 is required to reach coronal values in the core, k characterises the slope of the tangent hyperbolic and

ρ_{crit} reflects the radial extension of the ELM depletion on the profiles, while $\tau_{ped} = \frac{1}{f_{ELM}}$ is assumed. Once τ is defined, the $n_e \cdot \tau$ profile is built and the non-coronal P_{rad} is calculated as $P_{rad} = L_z(T_e, n_e \cdot \tau) \cdot n_e^2 \cdot c_z$, where c_z is given by the CXRS diagnostic.

Figure 6.3 shows the comparison of the P_{rad} calculations assuming coronal equilibrium (panel a)) and non-coronal conditions determined by the model (panel b)). The core radiation is dominated by tungsten while the edge is dominated by low-Z impurities (C, O, N). Since non-coronal effects affect mainly the low-Z impurities at the edge ($\rho > 0.8$), where the radiation is strongly enhanced, under coronal assumption, the radiated power is significantly underestimated. Hence, for a correct calculation of the radiated power it is crucial to take the non-coronal effects into account. The model is compared with the bolometric measurements (figure 6.4). The mismatch between the calculated and the measured radiation in the core ($\rho_{tor} < 0.2$) is attributed to the limited spatial resolution of the bolometry already discussed in section 6.1. At the very edge ($\rho_{tor} > 0.9$) the experimental results are not reliable due to the uncertainties discussed in section 6.1(figure 6.1 c)). Because the tomography reconstruction has to minimize the 2D curvature, the 1-D profile tends to be hollow as well. However, the comparison shows that indeed the edge is better described by the non-coronal model. P_{rad} obtained with the non-coronal model is used in the transport calculations presented in the next section.

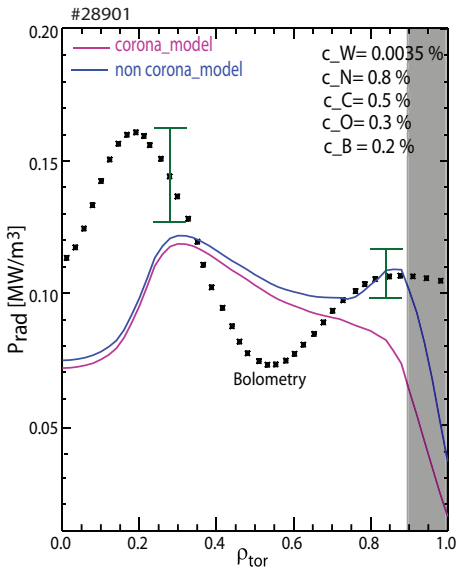

Figure 6.4: Radiation profile from bolometric measurements (black dots). Calculated P_{rad} using coronal approximation (magenta), calculated P_{rad} using the non-coronal model (blue).

6.3 Experiment set up

In the full-W AUG, a high fraction of the heating power can be radiated by varying the seed impurity radiation distribution using dual seeding technique in feedback control and feedforward [75]. Ar and Kr are injected through a midplane valve, N through valves located in the divertor region and distributed toroidally. The exact location and the gas rate are programmed before the discharge by the control system. In order to avoid central W accumulation and obtain stable H-modes with a tolerable W level, high fractions of central heating and a high deuterium gas puff of at least $\Gamma = 0.6 - 1 \cdot 10^{22}$ e^{-}/s are required. Such a high gas rate constrains operation at high plasma density $\left(\frac{n}{n_{GW}} = 0.6 - 0.8\right)$ reducing the achievable confinement ($H_{98} \cong 0.8$). However, confinement can be recovered by puffing N into the divertor as previously reported in [76] and as described in section 6.4.1. The experiments presented here were conducted in the so called "Improved H-mode" scenario [76] with a typical plasma current of I_p= 1-1.2 MA and a toroidal magnetic field of B_T= - 2.5 T suitable for 2^{nd} harmonic ECRH. The heating power was varied and covers a wide range: 5 MW < P_{tot} < 20 MW. In the 2012 campaign, a maximum heating power of up to 23 MW was applied whilst maintaining good performance. In the 2014 campaign, in order to ensure high quality of plasma measurements, experiments at lower powers of 10 and 15 MW were carried out in feed forward on N. In addition, 1 cm radial shift of the plasma allowed high quality edge profiles and a full pedestal coverage to be obtained.

6.4 Transport analysis

It is of a major interest to understand the impact of impurity seeding on plasma transport and confinement. In this regard, it should be pointed out that the formula 2.1 for the energy confinement does not take the radiated power into account. The reason is that in carbon machines, the effect of P_{rad} on τ_E is assumed to be small because P_{rad} is strongly hollow. However, in the case of central radiation, radiation losses have to be taken into account. Already in present tungsten machines, this high-Z impurity might radiate strongly in the core and the inclusion of the radiation losses is therefore crucial. Note that in order to avoid a reduction of the fusion gain, radiation losses occurring where the power is deposited are not permitted. Main chamber radiation must be applied solely at the periphery of the confined region. In future devices, like DEMO, where high P_{rad} will need to be radiated also in the plasma core, P_{rad} losses must be unavoidably considered. This is the reason why the radiation distribution is included in the power balance analysis in this work.

6.4.1 Transport analysis of nitrogen seeded discharges

The analysed discharges were H-modes with about 15 MW of heating power in which nitrogen was injected after the plasma reached its steady state. Figure 6.5 shows the time traces of the main parameters of a nitrogen seeded discharge where all the heating systems are employed: P_{NBI}= 10 MW, P_{ICRH}= 2 MW and P_{ECRH}= 2 MW. A strong D_2 puff is applied ($2.2{\cdot}10^{22}$ e^-/s) such that H_{98} is only 0.8.

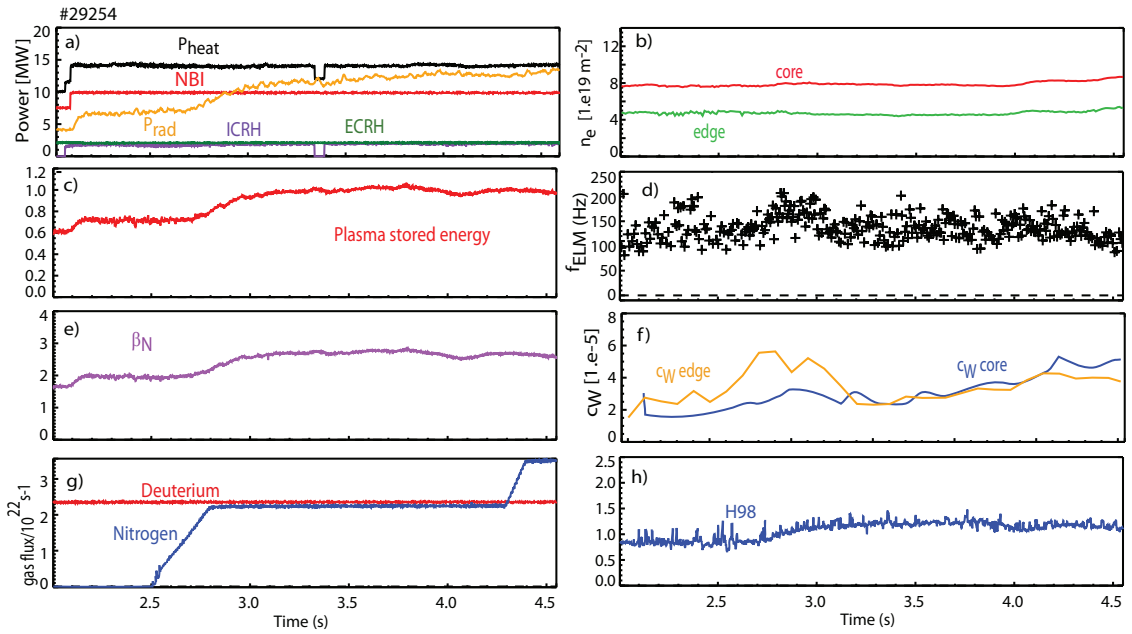

Figure 6.5: Time traces of main plasma parameters of discharge #29254: a) Heating and radiated powers, b) Core and edge densities, c) Plasma stored energy, d) ELM frequency, e) β_N, f) Core and edge tungsten concentration, g) N puff, h) H_{98}

At t = 2.5 s nitrogen is injected into the plasma, the heating power is kept constant from 2.1 s onwards (figure 6.5 panel g) and a)). As expected, the radiated power increases with N, but counterintuitively, the plasma stored energy also increases by about 40% (panel c)), as already reported in [76, 77]. β_N increases from 2 to 2.8 (panel e)) and the H_{98} from 0.8 to 1.2 panel h)). Note that W_{mhd} and β_N are both deduced from the equilibrium. In this discharge f_{ELM} (plot d)) does not vary with nitrogen (plot g)), but in other analysed cases it does. In Ref.[79] it was shown that with N the ELM crash consists only of a drop at the pedestal top. Another important feature of the ELM behavior with N is the reduction of the relative energy loss per ELM shown in section 6.5. The edge tungsten concentration decreases by a factor of 2 after nitrogen is injected due to the beneficial flush-out effect of the ELMs. After t= 3.7 s both concentrations tend to increase due to the approaching detachment phase (not shown here). The N concentration measured by CXRS is about 0.8 % in the first phase and 1.3 % in the higher gas puff phase. Z_{eff} increases from 1.1 to 1.5 with nitrogen. Carbon concentration in the plasma is about 0.5 %, boron around 0.2 % and oxygen 0.3 %. In order to gain a better understanding of the heat transport in

presence of nitrogen, power balance calculations taking into account the P_{rad} distribution have been performed with the TRANSP code which was presented in section 4.1.

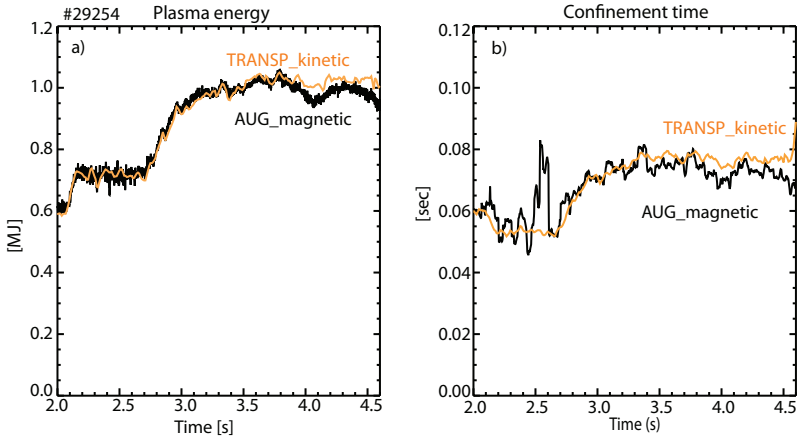

Figure 6.6: Time traces of a) Plasma stored energy from AUG magnetic measurements (black) and TRANSP calculation based on kinetic data (orange); b) Confinement time determination from AUG (black) and from TRANSP (orange).

The consistency between measured global parameters and TRANSP calculations based on kinetic data has been verified: as shown in figure 6.6 a), an excellent agreement for the plasma stored energy is found between the temporal reconstruction based on magnetic data (in black) and the TRANSP determination based on kinetic profiles (in orange). The energy confinement time calculated from TRANSP and from AUG magnetic are also in very good agreement (panel b)).

Measured electron and ion temperature profiles at the plasma edge before and during the N seeding are shown in figure 6.7 a). Higher temperatures are reached during nitrogen seeding in agreement with [76, 77]. Panel a) also reveals that the steep gradient zone of T_i extends further inside the plasma in the case of nitrogen. The N density profiles related to the different phases are shown in panel b).

The results of the transport analysis are displayed in figure 6.8. The dashed lines represent the ion channel, the solid line the electron channel. In black before the nitrogen seeding (ref. phase), in red during the N seeding. Panel a) shows that the pedestal improvement is propagated to the plasma core through stiffness: the higher temperatures are maintained over the whole profile causing the higher energy content. Panel b) shows that the density profiles are only weakly affected by the injection of nitrogen. The ratio $\frac{n_i}{n_e}$ (panel c)) is 0.8 in the unseeded phase and decreases to 0.7 in the seeded phase. Panel d) shows the net electron and ion fluxes defined as $Q_{e,net} = Q_e - Q_{ei} - Q_{rad}$ and $Q_{i,net} = Q_e + Q_{ei}$. Q_e and Q_i are the electron and ion fluxes. Q_{ei} is the exchange flux term from electrons to ions which plays an important role at high collisionalities. Q_{rad} is the radiation flux. As expected, $Q_{e,net}$ decreases at the edge due to the higher value of Q_{rad} induced by the presence of N. Panel e) reveals that χ_e and χ_i normalised by $T^{\frac{3}{2}}$ (see section 2.2) have similar values before and during the seeded phase. This is a sign that the seeding is not changing the core transport properties. Here the errors of χ and $R/L_{T_{e,i}}$ are estimated from

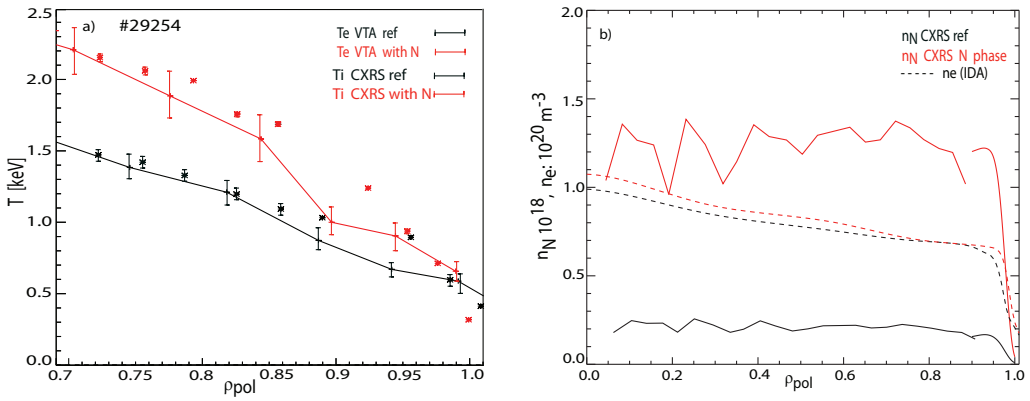

Figure 6.7: a) Edge profiles of: T_e from VTA (solid line), T_i from CXRS (stars) before N seeding (black), during N seeding (red). b) Nitrogen and electron density profiles in the reference phase (black) and in the N phase (red).

the uncertainties of the gradients of the temperature measurements. They are in the range of 20%. As indicated in panel f), from the pedestal top inwards, R/L_{T_e} and R/L_{T_i} are the same in both phases. This means, that since the profiles are bound to a fixed temperature gradient, the profile stiffness transfers the confinement improvement from the edge to the core.

The results of a sensitivity study of the radiation impact on transport are reported in figure 6.9. The integrated radiative power density Q_{rad} is compared to the electron heat flux Q_e. Q_{rad} is much smaller than Q_e in the central plasma, while it reaches about 30% of Q_e towards the edge. This means that the radiation is located in the outer part of the plasma as indicated by the tomography reconstruction (see section 6.1). This explains why it has almost no impact on global confinement. The transport analysis confirms that χ_e does not vary in the core whether the radiation losses are taken into account or not (panel b)). A sign that indeed the seeding is not changing the core transport properties. The fact that the radiation is localised at the edge is beneficial, since high radiation losses in the central plasma would reduce τ_E.

To summarise, the analysis provides evidence that N seeding increases the pedestal temperatures while the density remains unchanged. Thus, higher pedestal pressures are reached with nitrogen. The mechanism for which nitrogen increases the pedestal temperature is not yet understood and currently under investigation [80]. Although the absolute value of the temperatures are different, $\frac{\nabla T}{T}$ is the same indicating the strong role of the critical gradient lengths R/L_T in setting temperature profile features. This suggests that the relevant quantity for transport is R/L_T (see section 2.5).

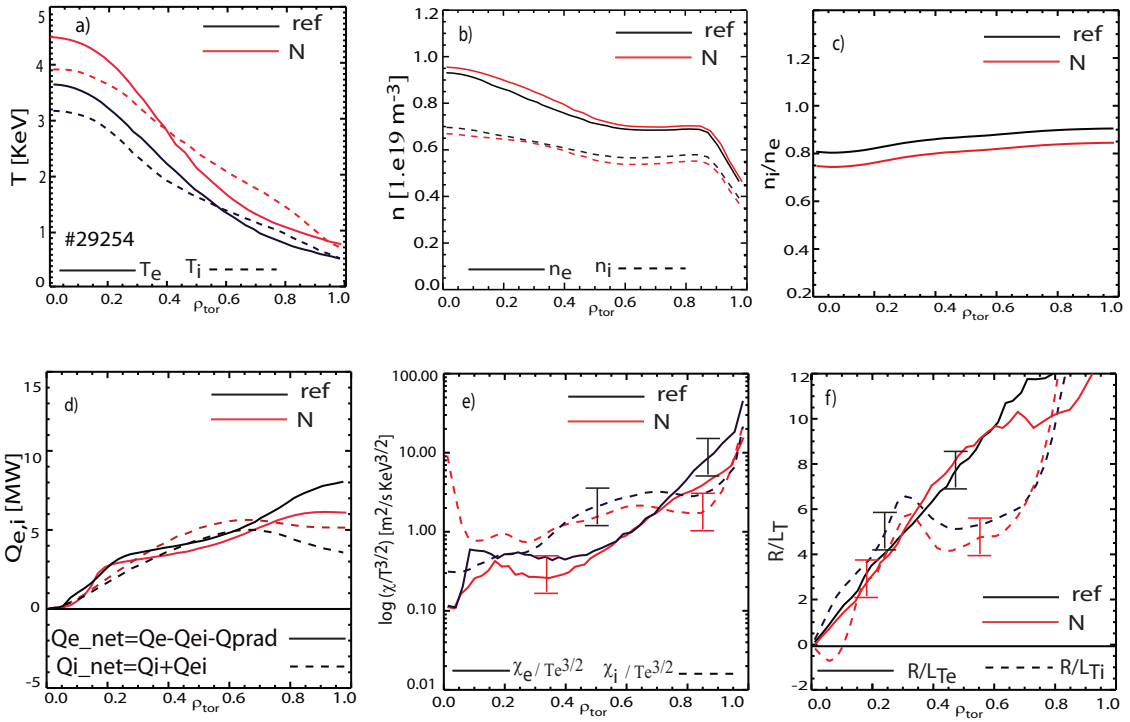

Figure 6.8: a) Temperature profiles, b) Density profiles, c) $\frac{n_i}{n_e}$, d) Electron and ions fluxes, e) χ_e and χ_i normalised by $T^{\frac{3}{2}}$, f) R/L_{T_e} and R/L_{T_i}. In black before N seeding, in red during N seeding. In solid lines for electrons and in dashed lines for ions.

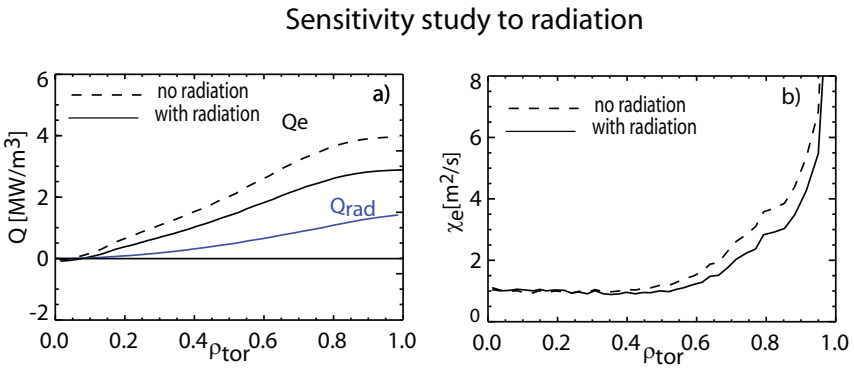

Figure 6.9: In black Q_e without Q_{rad} (dashed) and with Q_{rad} (solid). In blue Q_{rad}. b) χ_e without radiation (dashed), and including the radiation (solid).

6.4.2 Transport analysis of nitrogen and krypton seeded discharges

This section documents the analysis of the Kr seeded discharges where Kr is injected during the N puff. The H-mode discharges in this study are run at I_p = 1 MA, B_T = -2.5 T and a heating power of around 14 MW, 10 MW provided by NBI, the rest equally by ICRH and ECRH as shown in figures 6.10 a) and 6.11 a). Figure 6.10 shows the time traces of the main plasma parameters for discharge #31232 in which a stable phase (N+Kr) with moderate confinement was achieved. During the N puffing, Kr is injected at t= 3.6 s with an initial $\Gamma_{Kr} \simeq 0.5 \cdot 10^{21}$ e$^-$/s which rises until $1 \cdot 10^{21}$ e$^-$/s at t = 5.5 s (panel g)). The important observations are: an increase in W_{mhd} of 13% during the N phase and another 3% when Kr is also added to the plasma (panel c)); an increase in H_{98} (panel h)) from 0.78 in the reference phase, to 0.86 in the N+Kr phase; an increase in the neutron rate of 17 % (panel h)) and a drop of f_{ELM} in the N+Kr phase from a value of about 150 Hz to about 110 Hz.

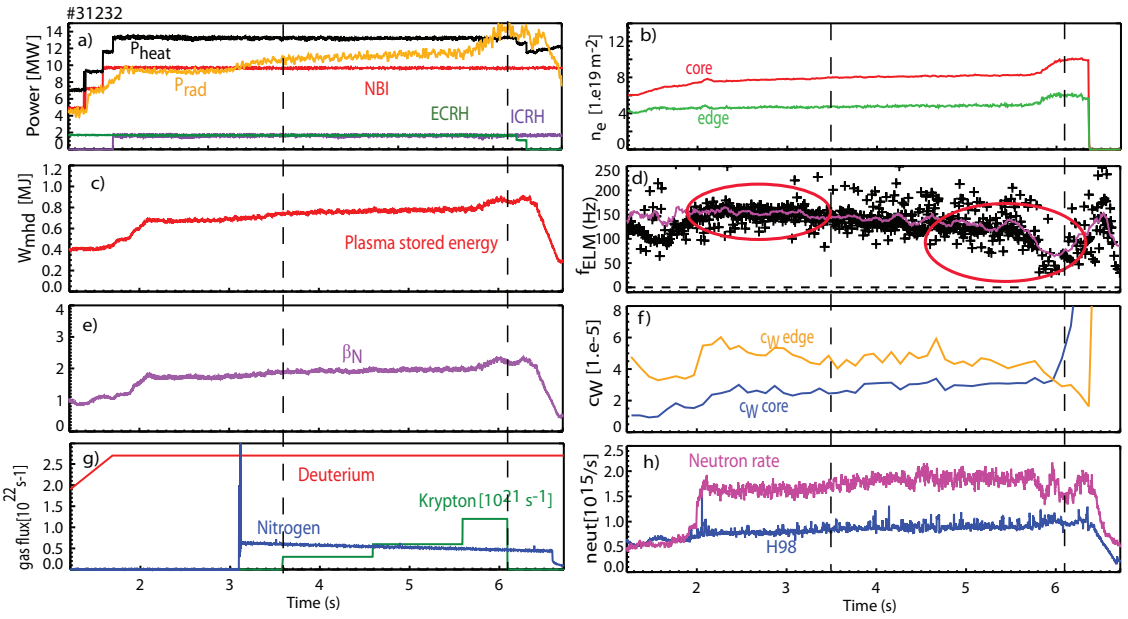

Figure 6.10: Time traces of main plasma parameters of discharge # 31232: a) Heating and radiated powers, b) Core and edge densities, c) Plasma stored energy, d) ELM frequency, in magenta f_{ELM} smoothed, e) β_N, f) Core and edge tungsten concentration, g) N and Kr puff, h) H_{98} and neutron rate. The vertical dashed lines define the time interval of Kr seeding.

If the amount of Kr is increased, the situation becomes unstable as illustrated in discharge # 31230 (figure 6.11) where an excessive Kr concentration led to a radiation collapse at t= 4.5 s. Since the effects of Kr on plasma response are more evident in this latter discharge, the analysis of this discharge #31230 is presented in the following. The analysis of discharge #31232 leads to the same conclusions drawn in this section.

The main plasma parameters of discharge #31230 are shown in figure 6.11. Before the radiation collapse, a short phase of increased confinement ($\sim$ 30%) with N and Kr can be

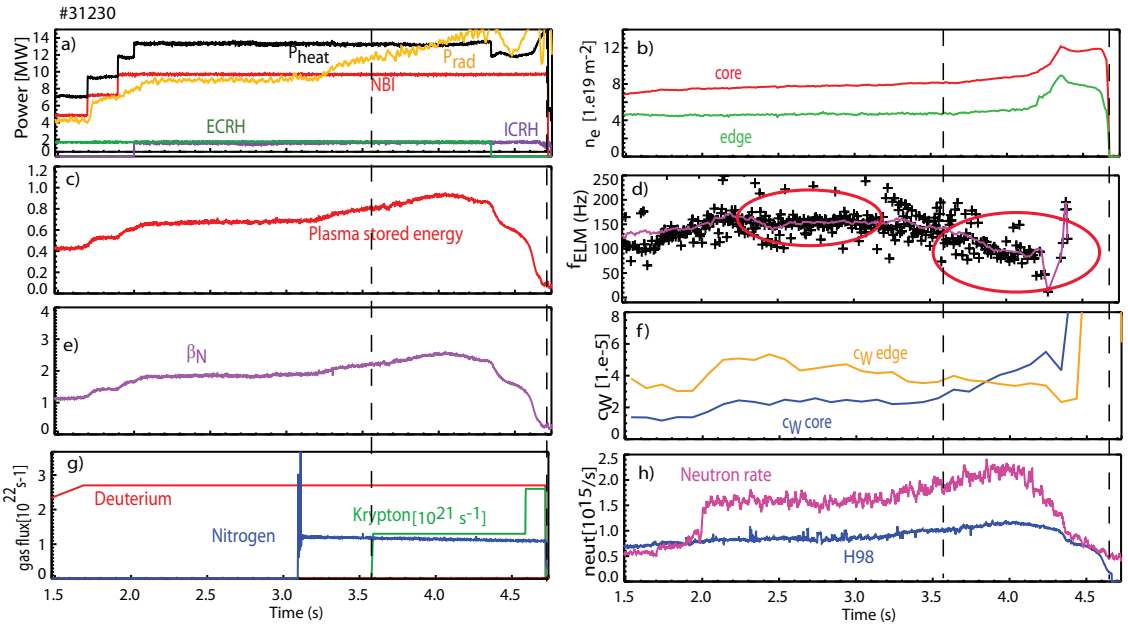

Figure 6.11: Time traces of main plasma parameters of discharge #31230: a) Heating and radiated powers, b) Core and edge densities, c) Plasma stored energy, d) ELM frequency, in magenta f_{ELM} smoothed, e) β_N, f) Core and edge tungsten concentration, g) D, N and Kr puff, h) H_{98} and neutron rate. The vertical dashed lines defined the time interval of Kr seeding.

identified (t = 3.5 - 4.2 s). The plasma stored energy increases from 0.6 MJ in the non seeding phase, to 0.74 MJ during the N-only phase and to 0.88 MJ in the N+Kr phase (before the collapse). β_N increases from 1.7 to 2.0 and to 2.4 in the N + Kr phase. The core and edge densities increase by 5% during the N+Kr phase. H_{98} increases from 0.7 to 0.9 in the N-only phase reaching 1.1 in the N+Kr phase. The neutron rate increases constantly throughout the discharge with a maximum increase of 40% in the last phase. The main contribution to the neutron rate in ASDEX Upgrade comes from the beam-target rate (S_{bt}) which is proportional to T_e and $\frac{n_D}{n_e}$ [81]. The observed rise of the neutron rate with N but in particular with Kr means that the increase in T_e and therefore in the confinement, is larger than the dilution effect. Figure 6.12 a) reveals that the increase in T_e at ρ= 0.6 from the reference phase to the N+Kr phase is about 40 %, whereas the decrease in the $\frac{n_D}{n_e}$ is only about 10% (figure 6.16 c)). The increase in both electron and ion temperatures between the N-only phase and the N+Kr phase is also well visible: at ρ= 0.6 T_e increases of an additional 16 % and T_i of an additional 24 % (6.12 panel b)).

However, the Kr concentration in the plasma becomes too high and triggers tungsten accumulation. This accumulation is a consequence of the reduction of the total heat flux with higher P_{rad} (see 6.16 panel e)). A smaller heat flux means that less source is available to drive turbulent transport making the effects of neoclassical transport more visible, as anticipated in section 2.4. This is particularly true for high-Z elements such as Kr and especially W since the neoclassical effect increases with Z. In addition, the temperature screening, which tends to counteract the convective term (section 2.4), gets lower as well.

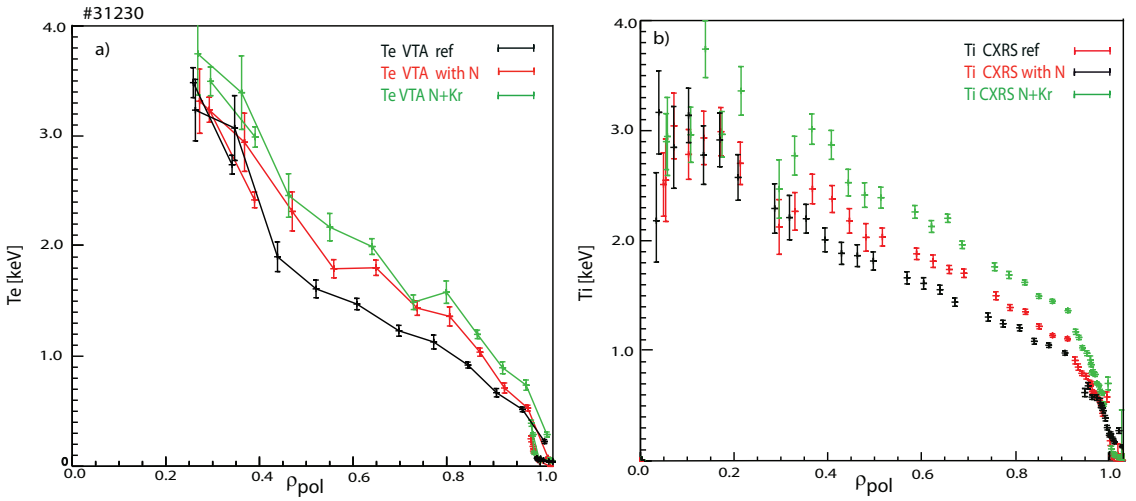

Figure 6.12: a) T_e from VTA; b) T_i from CXRS. Black (reference phase), red (N-only phase), green (N+kr) phase for discharge #31230.

Indeed, panel f) of figure 6.11 shows that as soon as Kr is injected into the plasma, the W concentration increases. Overall the core W concentration increases by a factor of 2 and at t = 4.28 s plasma detachment occurs. Panel d) shows that the ELM frequency drops by 50% when Kr is added to N going from about 150 Hz to 70 Hz. The f_{ELM} reduction is a consequence of Kr radiation inside the pedestal which reduces the heat power flux through the pedestal.

In this thesis the confinement improvement observed in the phase with N+Kr is interpreted as follows: since f_{ELM} gets lower, less power is available to recover the profiles after each ELM crash. Therefore, with a longer inter-ELM phase, N can stay in the plasma longer before it is flushed out with a consequent increase of its concentration in the plasma, as shown in figure 6.14 b). Although other effects could play a role, the confinement improvement is attributed here to the increase of the nitrogen concentration in the plasma which is higher due to a lower f_{ELM} (figure 6.13).

Figure 6.14 a) depicts the tomography reconstruction at t = 4.0, 4.2 and 4.5 s when N and Kr are both in the plasma. In addition to the strong divertor radiation due to N, the tomography illustrates that the plasma radiates across the entire plasma radius inside the pedestal due to Kr. Note that with the increase of Kr radiation, less power goes to the divertor (at t= 4.5 s the divertor region is not longer red but green-blue) and a higher contribution from the main chamber is evident until at t = 4.5 s an intense radiation appears in the core indicating the onset of the radiative collapse due to both krypton and tungsten accumulation.

Currently there is no diagnostic available to measure the Kr concentration. In this work, the Kr concentration was estimated using the following method: the radiation due to Kr is simulated with STRAHL assuming that only this impurity is present in the plasma. The inputs to STRAHL are the equilibrium, the transport, the density and temperature profiles and the impurity source. The integrated radiation along the midplane delivered

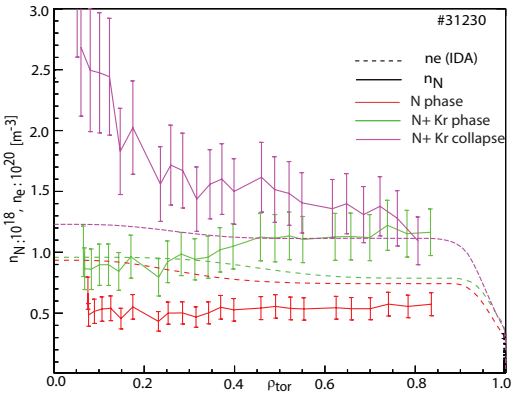

Figure 6.13: N density profile in red during the N-only phase, in green during the moderate N+Kr phase, in magenta at the onset of the radiation collapse. In dashed the corresponding n_e.

by STRAHL is used and its value compared with the one provided by the line integral of the foil bolometry at the midplane. The difference of the P_{rad} measured by the bolometry lines of sight of the FHC camera (figure 6.1 a)) at midplane before and during the Kr injection provides the Kr contribution to the radiation. The Kr source in STRAHL is varied till the corresponding radiation matches this difference.

Using this method it was possible to reconstruct the Kr concentration during the steep increase of the radiation between t = 4.0 s and t = 4.3 s of the discharge #31230. The evolution of the Kr radiation reconstructed by STRAHL in the time interval 4.0 - 4.3 s is shown in figure 6.15. From the Kr and electron density at each considered time point, the Kr concentrations were obtained. The Kr radiation, the relative impurity densities and the concentrations in the time interval t = 4.0 s - 4.3 s are summarised in table 6.1.

$time$	$P_{rad,Kr}[MW]$	$n_{Kr}[10^{16}m^{-3}]$	$c_{Kr}[10^4]$	$c_N[10^2]$
4.0s	0.20	2.4	1.9	1.1
4.1s	0.27	3.4	2.3	1.2
4.2s	0.32	4.0	3.3	1.2
4.3s	0.44	4.9	3.9	1.3

Table 6.1: Radiation, density and concentration of Kr reconstructed by STRAHL in the time interval 4.0 - 4.3 s for discharge #31230. The N concentration at the corresponding time points is also reported.

The radiation values from which the Kr concentration was deduced have been cross checked with the results given by the tomography reconstruction whilst considering that the latter also contains the contributions from tungsten, nitrogen, boron, carbon and oxygen. For discharge #31232 presented at the beginning, a Kr concentration of 1.7 $\cdot 10^{-4}$ is estimated at t = 5.0 s. The gas puff is then further increased and a concentration of $3.2 \cdot 10^{-4}$ at t = 5.9 s has been estimated. As we have already seen for discharge #31230 a Kr concentration of 3.2 $\cdot 10^{-4}$ leads to a radiation collapse. On the other hand, from

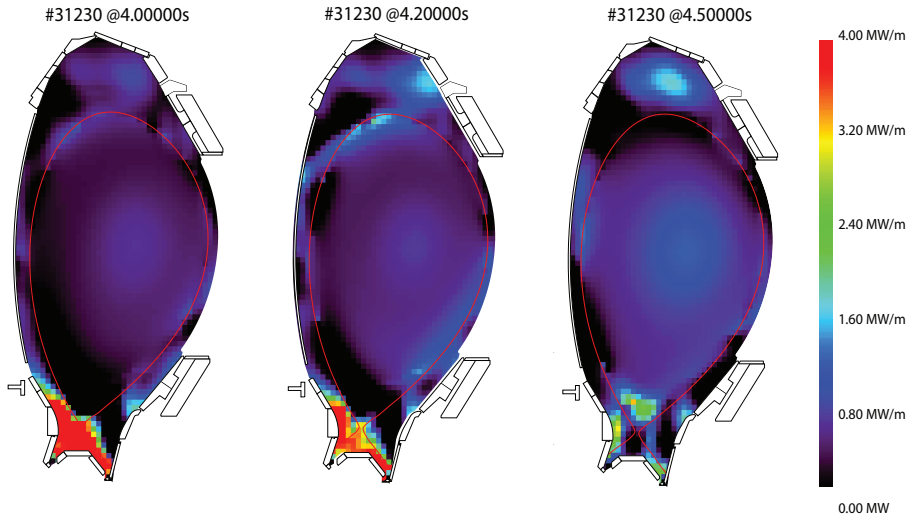

Figure 6.14: a) Tomography reconstruction for discharge #31230 at t= 4.0, 4.2 and 4.5 sec. The strong radiation ring in the centre at t= 4.5 sec indicates the onset of the radiative collapse, b) N density profile in the N only phase (red) and in the N+Kr phase (green).

the analysis of other Kr discharges it has been observed that a concentration $> 1{\cdot}10^{-4}$ is required to obtain a modest confinement improvement. Therefore, based on the results obtained here, the region of Kr concentration which, together with an opportune N seeding, can lead to a confinement improvement before the onset of impurity accumulation lies around $2 \cdot 10^{-4}$.

For discharges with Kr, the heat transport analysis is of utmost importance to understand where the radiation losses take place. Figure 6.16 summarises the most important results of the heat transport analysis performed with TRANSP in black during the non seeding phase, in red during the N-only phase and in green during the early N+Kr phase before the onset of the radiation collapse. As already seen in the previous section, higher pedestal temperatures in both channels are reached during the N seeding which are then extended to the core via stiffness (Panel a)). In addition to this improvement, the plot demonstrates that a Kr concentration of about $1.9{\cdot}10^{-4}$ combined with N can lead to even higher temperatures than obtained with N-only. At ρ= 0.6, the rise in T_e from the N-only to the N+Kr phase is about 17% whereas the increase in T_i is about 26%. The electron density increases slightly during the N-only phase, while the increase is more remarkable during the Kr phase. This increase takes place at the pedestal. This is ascribed here to the fact that less frequent ELMs are available to flush out particles at the edge. The decrease in $\frac{n_i}{n_e}$ (panel c)) is only 10% from the reference case to the N+Kr phase, indicating that dilution caused by Kr is rather small as expected from its low concentration.

The transport analysis reveals also that Q_{rad} increases by about 45% during the N+Kr phase, playing an important role in the total heat flux. The "knee" observed in Q_e (ρ=0.2) is due to the presence of the ECRH which is important to avoid accumulation of heavy

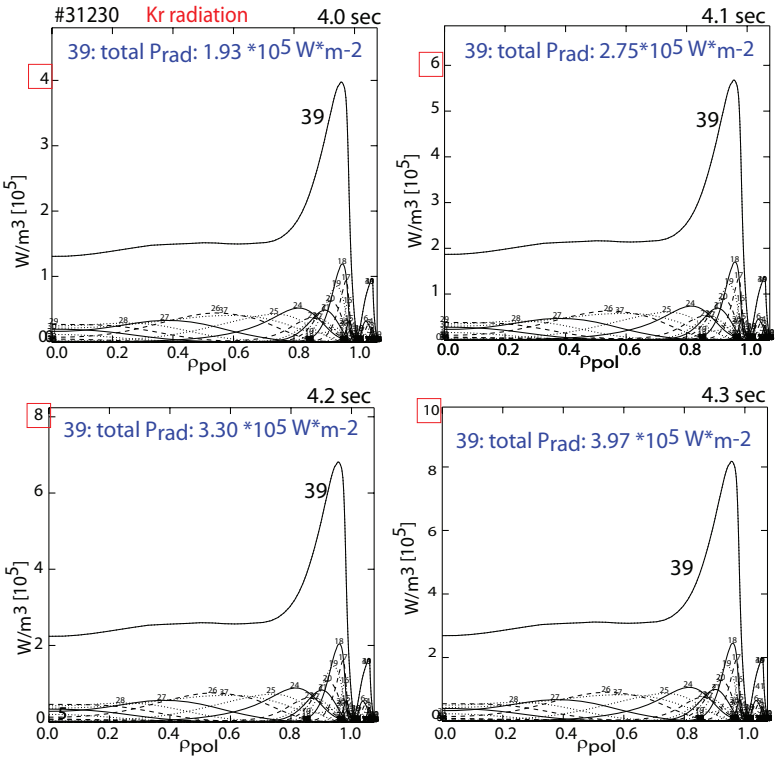

Figure 6.15: Kr radiation calculated with STRAHL during the steep radiation increase between t = 4.0 and 4.3 s in discharge #31230. Note the increasing scale. Kr radiates mostly between ρ_{pol}= 0.8 - 1.0. The contribution of all ionisation stages is also shown. Their sum gives the total P_{rad} (written in blue).

impurities (section 5.2.2).

Both χ_e and χ_i normalised to $T^{\frac{3}{2}}$ are lower during the Kr seeding as displayed in panel f). The reduction is more pronounced in the ion channel. Note that they are almost unchanged during the N-only phase, confirming the results of section 6.4.1. Although there is no significant difference considering the error bars, a slight decrease in the core transport cannot be excluded. The reduction of the core transport when a high fraction of the power is radiated is consistent with the reduction in turbulence needed to drive the heat flux. Thus, as mentioned above, the effects due to neoclassical transport become more visible. At mid-radius both R/L_{T_e} and R/L_{T_i} show similar values to those expected from profile stiffness (plot g)). It is interesting to look at R/L_{n_e}, since the W and to a lesser extent the Kr behaviour are determined by the evolution of the main plasma density profile through the inward convection. The decreases of R/L_{n_e} around $\rho = 0.4$ when Kr is injected (plot h)) indicates a more peaked density profile (as seen in plot b)). This is related to the increase of the Ware pinch (neoclassical effect) and points out that an influx of heavy impurities (Kr and W) is taking place. Indeed, few ms later in the discharge, this impurity influx causes impurity accumulation which is attributed to the fact that the neoclassical inward convection is no longer counteracted by a sufficient anomalous diffusion. In chapter 7 is shown that, starting from the assignment of the transport coefficients, the impurity accumulation can be reproduced. The transport analysis of the discharge

#31232 presented at the beginning of this section leads to the same conclusion as drawn here. Finally in order to document the temperature behaviour both T_e from VTA and T_e from CXRS are depicted in figure 6.12. In both electron and ion channels, higher pedestal temperatures are obtained in the N+Kr phase. The increased ion pedestal is particularly evident.

In summary, the experimental study conducted here shows that krypton efficiently radiates inside the pedestal region. Due to its radiation properties, its concentration must be kept low (in the order of $2 \cdot 10^{-4}$) and accurately controlled. In this case, combining it with appropriate N seeding, this analysis shows: 1) higher pedestal temperatures are reached induced by a higher N concentration. In this thesis this behaviour is attributed to a lower f_{ELM}. 2) R/L_{T_e} and R/L_{T_i} do not change but a slight decrease in the heat diffusivities is found albeit not significant outside the error bars. 3) An irreversible impurity accumulation can occur above a certain level of radiation attributed to the reduction of the ELM frequency and the corresponding lack of sufficient impurity flush out in the pedestal.

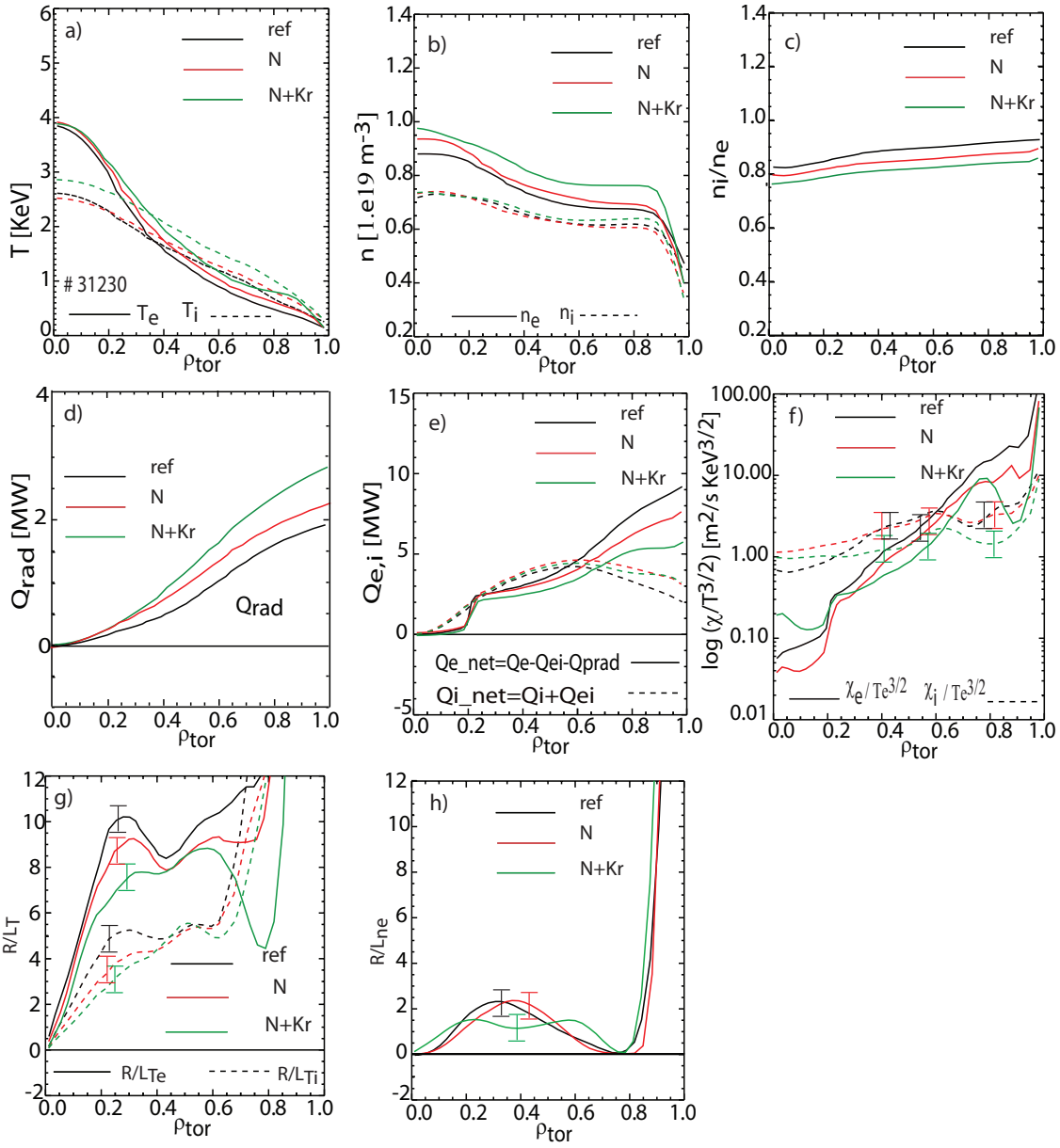

Figure 6.16: a) Temperature profiles, b) Density profiles, c) $\frac{n_i}{n_e}$, d) Q_{rad}, e) Electron and ion fluxes Q_e and Q_i, f) Electron and ion heat diffusivities, g) R/L_{T_e} and R/L_{T_i} , h) R/L_{n_e}. In black before N seeding, in red during N seeding, in green during the N+Kr phase. In solid lines for electrons and in dashed lines for ions.

6.4.3 Transport analysis of nitrogen and helium seeded discharges

In this section the analysis of experiments with both nitrogen and helium seeding is presented. Such analysis contributes to the investigations for scenario development relevant for reactor operation. In future reactors ^{4}He will be produced in the core as a product of the D-T reaction and therefore understanding its core transport properties is crucial. It is estimated that ITER will have a He concentration of 5% in the main plasma [82]. It is important to keep its concentration as low as possible because it unavoidably dilutes the fuel reducing the fusion efficiency. Moreover, since it will be produced in the core of the plasma, its accumulation must be avoided. Since in present tokamaks it is not possible to study the He impact in burning plasma conditions, He is intentionally puffed through valves into the plasma. Its concentration can be measured locally by charge exchange spectrometry as introduced in section 5.3.6. Note that helium is not injected as a seeded impurity for radiation cooling purposes, its radiation capabilities are in fact limited. Rather it is puffed in order to simulate and study its global effect on the plasma.

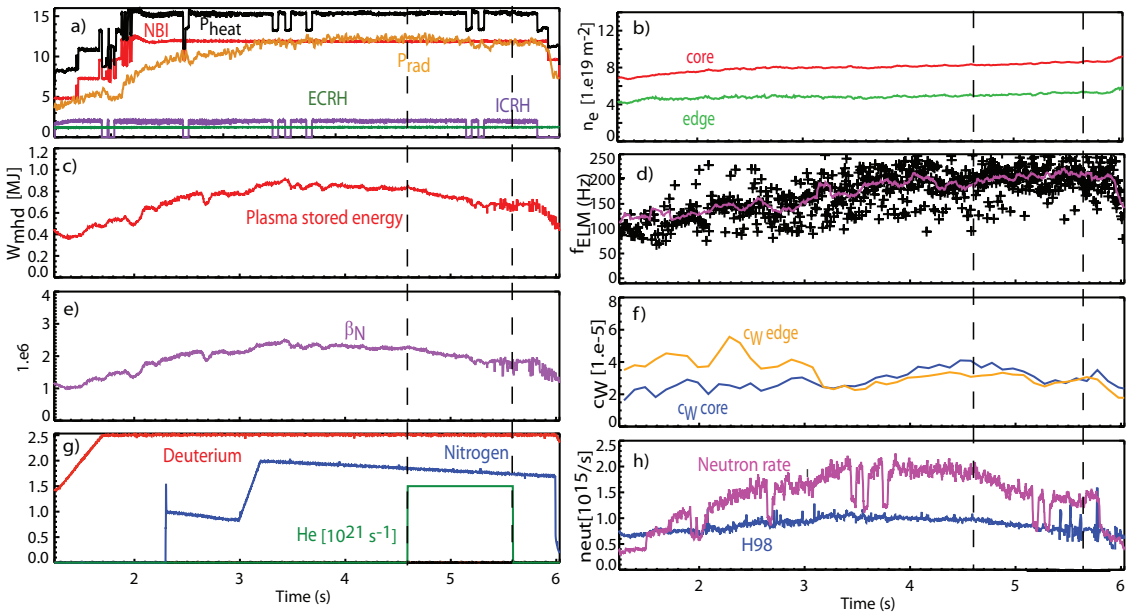

Figure 6.17: Time traces of main plasma parameters of discharge # 30423: a) Heating and radiated powers, b) Core and edge densities, c) Plasma stored energy, d) ELM frequency, in magenta f_{ELM} smoothed, e) β_N, f) Core and edge tungsten concentration, g) N and He puff, h) H_{98} and neutron rate. The vertical dashed lines defined the time interval of He seeding.

Figure 6.17 shows the time traces of the main parameters for discharge #30423 where He was puffed during the nitrogen seeding. At I_p = 1.00 MA, B_T= -2.5 T and a constant heating power of about 15 MW, at t = 2.3 s N is injected into the plasma (with a puff of roughly $\Gamma_N = 1.7 \cdot 10^{22}$ e$^-$/s) inducing the typical observed confinement improvement. Later in the discharge, precisely at t = 4.6 s, a He puff of $\Gamma_{He} \sim 1.5 \cdot 10^{21}$ e$^-$/s is added. The He concentration measured by CXRS is $\sim$ 10% and induces a plasma stored energy drop of $\sim$ 23%. The H_{98} goes from 1 to 0.8. The degradation of the confinement is

also expressed by the neutron rate (panel h)) which decreases by 27%. The decrease in the neutron rate is attributed to the combined effect of dilution and lower central ion temperature. The electron density increases by roughly 12 %. The ELM frequency goes from about 145 Hz before N to roughly 190 Hz with N, reaching 210 Hz with He. The W concentration before nitrogen seeding is about $4{\cdot}10^{-5}$ at the edge and $2{\cdot}10^{-5}$ in the core. During the nitrogen phase both concentrations are about $2.5{\cdot}10^{-5}$ and they decrease slightly during the N+He phase. Their decrease is attributed here to the increased f_{ELM}.

Figure 6.18 a) shows the impurity densities of He and N measured by CXRS during the helium puff. While N exhibits a rather flat profile over the radius, the helium density profile is at least as peaked as the electron density profile in agreement with [70]. It reaches a significantly peak in the centre towards the end of the puffing. Of course such a peaked profile in the plasma core where the fusion reactions take place is detrimental for fusion performance. Panel b) compares the nitrogen profile in the N-only phase with the profile during the N+He phase. In the latter case the N profile is lower than in the N-only phase which here is ascribed to the increased f_{ELM} flushing more often the impurities out of the plasma.

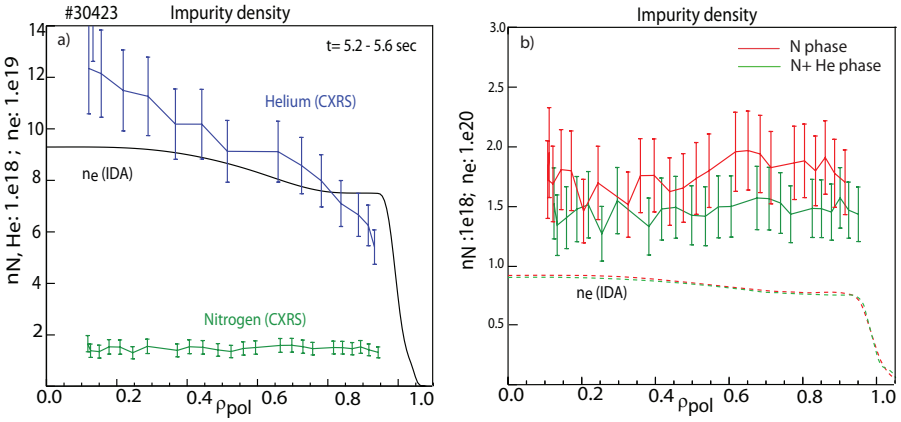

Figure 6.18: a) Impurity density profile for discharge # 30423 of nitrogen (green), helium (blue), electron density from IDA (black, different scale). Note the peaked He profile. b) Nitrogen density profile in the N-only phase (red) and during the N+He phase (green). In dashed n_e from IDA.

Figure 6.19 a) and b) show the ion temperature measurements from CXRS, along the whole radius and in the region $0.8 < \rho_{pol} < 1.05$. Panel b) shows that for $\rho > 0.96$ the T_i measurements during the N-only phase and during the N+He phase overlap each other. A decrease of the temperature during the He phase takes place from $\rho_{pol} < 0.96$ inwards. The temperature gradients of the two phases appear to be the same but the width of the pedestal during the N only phase is broader allowing higher ion temperatures already at $\rho_{pol} \sim 0.94$ where $T_i \sim 1.3$ keV compared to $T_i \sim 1.1$ keV measured during the He phase. At $\rho_{pol} \sim 0.4$ the decrease of the ion temperature during the N+He phase is $\sim 20\%$. The electron temperature from IDA is illustrated in panel c) and d). In this case T_e in the N-only phase and in N+He phase are identical only in the region $0.98 < \rho_{pol} < 1.0$. From $\rho_{pol} = 0.98$ inwards the helium case is characterised by a lower temperature along the

whole radius. During the He phase, both temperature pedestal profiles are still well above the reference case while the core values are reduced. In particular, the decrease in T_i in the confined region is significant as such that it is at the same level of the reference phase. This suggests that a degradation effect in the core might also be present. This has been assessed by the transport analysis.

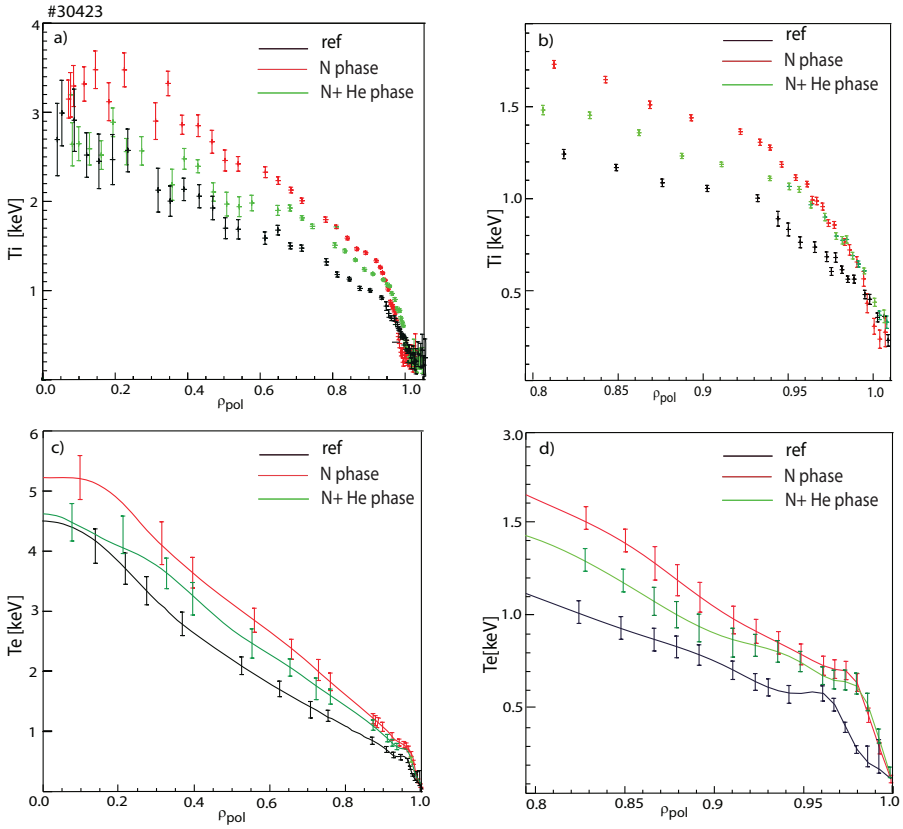

Figure 6.19: a) T_i along the whole radius, b) T_i in the region $0.8 < \rho_{pol} < 1.0$, c) T_e along the whole radius, b) T_e in the region $0.8 < \rho_{pol} < 1.0$. In black (ref phase), in red (N-only phase), in green (N+He phase).

The results from the transport analysis are illustrated in figure 6.20. Panel a) shows the electron (solid lines) and the ion (dashed lines) temperatures for the three different phases: reference phase without seeding (black), N-only phase (red) and N+He phase (green). In the He phase the temperatures lie between the reference phase and the N only phase. Hence, the confinement improvement obtained by nitrogen seeding is almost lost. In contrast to the Kr case, with He, the ELM frequency increases. In this case, the following mechanism is proposed: the higher ELM frequency leads to a frequent flush out of impurities at the edge such that less nitrogen stays in the plasma and its beneficial effect is partially lost.

The electron density increase compensates for the decrease in ion density. However, the addition of He does not produce an additional substantial decrease in the ion density compared to that in the nitrogen phase (panel b)). Panel c) shows $\frac{n_i}{n_e}$. Overall the density fraction decreases by 15% from the reference phase to the He phase of which 6% takes

place from the N-only phase to the N+He phase. Panel e) shows the electron and ion fluxes. Due to its radiation, Q_e decreases with nitrogen as learned in section 6.4.1. The He contribution to radiation instead is negligible such that the flux remains practically unchanged when He is added to N. In more detail Q_e at the very edge is higher than in the N phase. This is attributed to the fact that there is a smaller contribution to the radiation from nitrogen due to a lower concentration induced by the higher f_{ELM}. The electron and ion diffusion coefficients normalised by $T^{\frac{3}{2}}$ are shown in plot e). The plot reveals an increased χ_i along the whole radius. In the electron channel instead, the variation of the diffusion coefficient is not as pronounced: χ_e lies in between the values of the reference phase and the nitrogen phase. In both cases their variations are within the error bars. In the He seeded discharges investigated in this thesis, no sign of W accumulation was found. This means that peaked He profiles are not problematic in terms of impurity accumulation. However, as mentioned earlier, the situation in a reactor will be different because of the presence of a central He source from the fusion reaction. Since the impact of the helium source on central fuel dilution is governed by the magnitude of the He diffusivity, a higher core transport could be beneficial in avoiding He accumulation in the core which is of concern in future devices. Panel f) displays R/L_{T_e} and R/L_{T_i} which stay at a similar levels in the N-only and the N+He phase. Their variations are within the error bars indicating also in this case a critical gradient behaviour.

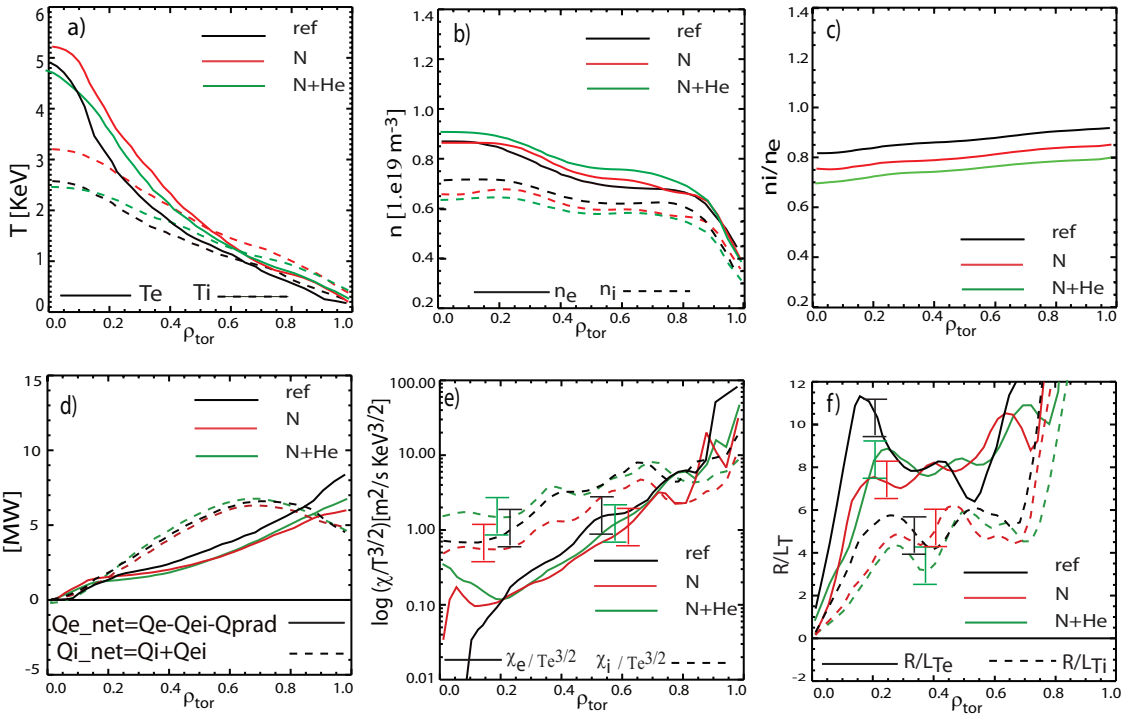

Figure 6.20: a) Temperature profile, b) density profiles, c) $\frac{n_i}{n_e}$, d) Electron and ion fluxes Q_e and Q_i, e) Electron and ion heat diffusivities, f) R/L_{T_e} and R/L_{T_i}. In black before the N seeding, in red during the N seeding, in green during the N+Kr phase. In solid line for electrons and in dashed lines for the ions.

The analysis presented here indicates that He concentrations in the plasma degrade fusion

performances, particularly affecting the ion channel. This is in line with previous work in Ref. [83] where a reduced pedestal width of T_i was found in presence of He-only. In this thesis, the analysis of [83] is extended by the use of nitrogen and a conduction of a transport analysis. This section provides evidence that in presence of He: 1) the pedestal width of the ion temperature is reduced compared to the N phase, 2) the variations of R/L_{T_e} and R/L_{T_i} are within the errors, 3) χ_e and χ_i are within the errors although a more significant variation of χ_i along the whole radius is found, 4) the increase of the ELM frequency with He leads to lower N concentrations.

In the cases analysed here the addition of He to N reduces the plasma performance such that it lies between the reference and the N case. The reduction of the confinement is attributed partly to a direct degradation induced by He [83] and partly to the reduction of the N concentration caused by a lower f_{ELM}.

6.5 Database of seeded discharges

A database of experimental data of seeded H-mode discharges performed at ASDEX Upgrade in the 2012-2014 operational campaign has been collected. It contains discharges with different core radiation levels induced by both Ar and Kr in combination with divertor radiation obtained by different levels of N seeding. Each of the 79 points is an average of the data taken in a time interval of at least 100 ms. The database spans from low power phases (5 MW without seeding) to high power phases of about 20 MW passing through 10, 15 and 18 MW combining the different radiators. Plasma current was in the range of I_p= 1.0-1.2 MA and the toroidal magnetic field in the range of B_t= 2.46-2.53 T. Figure 6.21 shows the achieved parameter ranges and some important correlations of the database.

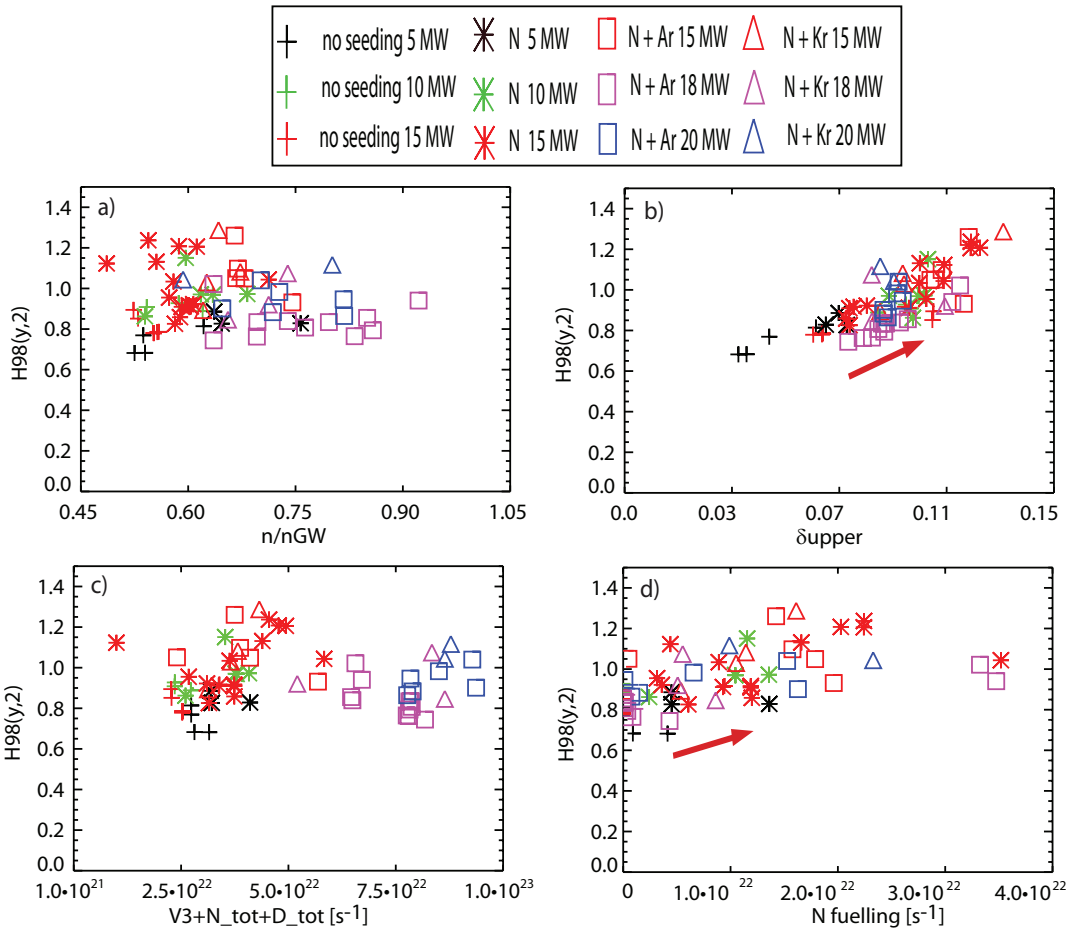

Figure 6.21: a) H_{98} vs $\frac{n}{n_{gW}}$, b) H_{98} vs upper triangularity, c) H_{98} vs total gas puff, d) H_{98} vs N fuelling.

Plot a) shows the H_{98} as a function of the Greenwald fraction $\frac{n}{n_{GW}}$ indicating that a wide range of $\frac{n}{n_{GW}}$ has been obtained. Note that high Greenwald fractions of $\frac{n}{n_{GW}} \simeq 0.9$ can be reached keeping H_{98} near 1. H_{98} spans from 0.75 in the unseeded discharge at low heating power, to 1.3 in N-only phases and in discharges where N has been combined with argon

or krypton. Data points representing Ar seeding align very well. Some of them attain a Greenwald fraction of about 0.85, which is the required value for ITER, still keeping an acceptable confinement. The stagnation of H98 with increasing $\frac{n}{n_{GW}}$ is easily visible. It will be discussed in detail in section 8.2.2.

Plot b) shows H_{98} vs. upper triangularity (δ_{upper}). Triangularity characterises the plasma shift between the X point and the magnetic axis. The plot indicates that confinement increases with plasma shaping. An upper triangularity of 0.13 allows H_{98} values of 1.3 to be reached with a heating power of 15 MW. However, note that δ increases with β and therefore H_{98} and δ are partly correlated.

Plot c) displays the H_{98} vs. total gas puff as the combination of deuterium, nitrogen, argon or krypton. The plot shows that a wide range of gas fuelling has been explored while maintaining good performance. The highest confinement is obtained at 15 MW both with N-only seeding or combining N with Ar or Kr at relatively low gas fuelling. The highest confinement values are reached for a total gas puff of $\Gamma < 4.9 \cdot 10^{22}$ e^-/s. Higher gas puffs at even higher heating powers lead to a lower H_{98}.

Plot d) illustrates the relation between H_{98} and N seeding. It indicates that the improvement of confinement is correlated with nitrogen fuelling. This is a well known effect taking place at different densities and heating powers. While using only N, the improvement is more pronounced at higher power: e.g. seen by comparing the green stars (N only at 10 MW) with the red stars (N only at 15 MW). This is due to the fact that higher heating power allows operation with a higher N concentration. For this reason, due to the limited seeding possibilities at lower powers, the plot is characterised by a smaller spread at low powers. When combining main chamber radiators with nitrogen the situation becomes ambiguous: in some cases a better confinement than in the N-only phase can be attained, in other cases the confinement is lower. This behaviour was well illustrated in section 6.4.2 where it was shown that the typical situation observed with Kr seeding exhibits a first phase of confinement improvement followed by a radiation collapse. Given the high radiative capability of Kr, it is important to determine the amount of Kr that allows the plasma to reach and, more importantly, to sustain a stable confinement improvement phase without rapidly causing a radiation collapse. In section 6.4.2 it was estimated that a Kr concentration of $2 \cdot 10^{-4}$ at 15 MW allows the highest confinement. In a few discharges the N puffing was intentionally increased drastically in order to investigate its effect on plasma performances. Plots d) highlights that a confinement increase is obtained up to $\Gamma_N = 2.6 \cdot 10^{22}$ e^-/s. A huge nitrogen puff of $\Gamma_N \sim 3.5 \cdot 10^{22}$ e^-/s used alone or combined with argon does not further increase the confinement. A limit of the maximum nitrogen puff still inducing confinement improvement can therefore be identified in the region $\Gamma_N = 2.6 - 3.5 \cdot 10^{22}$ e^-/s.

Figure 6.22 panel a) shows H_{98} against the radiation fraction. Thus, discharges with different heating powers can be compared, since the heating power is directly related to the possibility of radiating at different levels. As shown in the time traces of the discharges presented in this chapter, the confinement improves with increasing radiation fraction. At

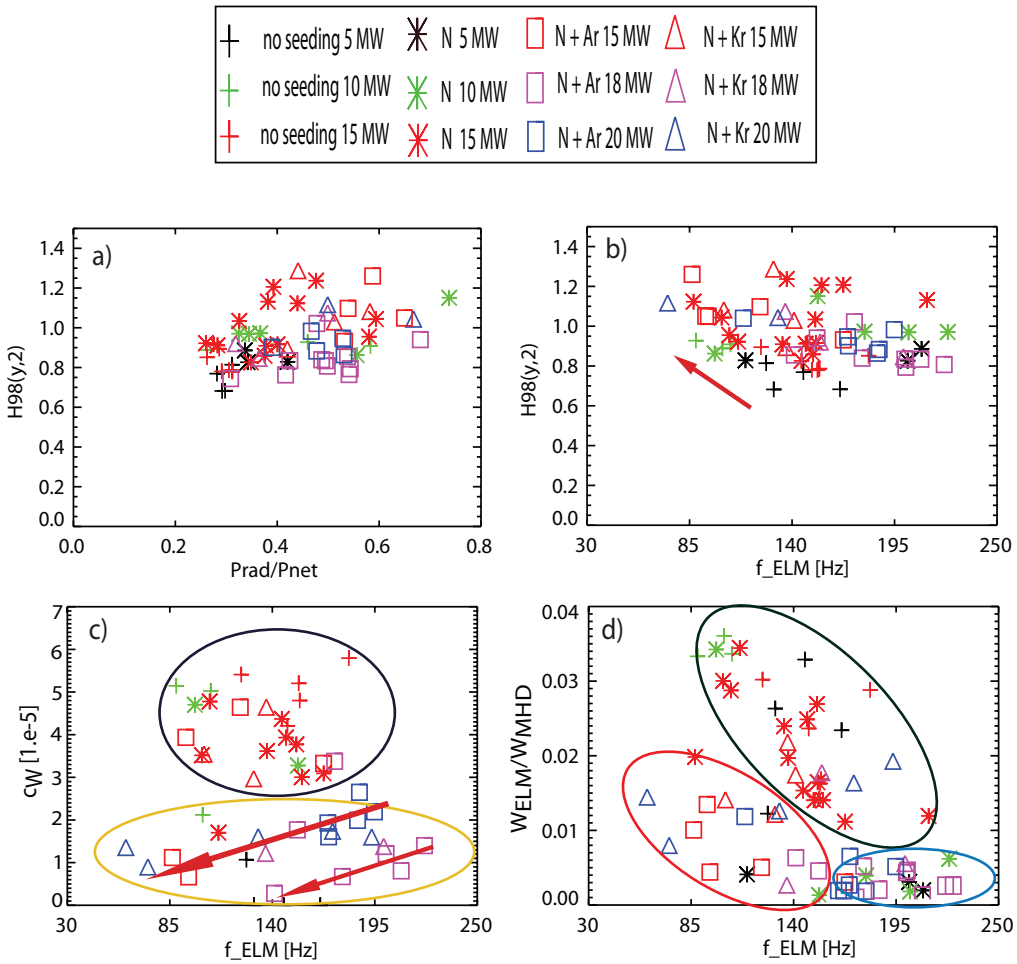

Figure 6.22: a) H_{98} vs f_{ELM}, b) c_W vs f_{ELM}, c) Relative ELM energy loss vs f_{ELM}, d) normalised ELM particle loss vs f_{ELM}

the same radiation fraction, at high heating power, krypton allows a higher confinement than argon: the blue triangles (N+Kr at 20 MW) always lie above the blue squares (N+Ar at 20 MW). The magenta triangles (N+Kr at 18 MW) are always above the magenta squares (N+Ar at 18 MW).

A matter of interest is the impact of the seeding on f_{ELM} and the tungsten concentration. Panel b), representing H98 vs. f_{ELM}, highlights that $H_{98} > 1$ can be reached with N-only at 15 MW, N+Ar at 15 MW and N+Kr at 15 and 20 MW with an f_{ELM} in the range between 80 and 160 Hz. For $f_{ELM} \geq 160$ Hz, H_{98} lies mainly below 1. Discharges with heating powers of 18 MW lie mainly below $H_{98} = 1$, both for Kr and Ar, whereas discharges with Kr at 15 and 20 MW lie mostly above $H_{98} = 1$. Data points with argon at 15 MW also lie above $H_{98} = 1$, while at 20 MW they are below. Ultimately, the plot illustrates the trend of H_{98} to increase with decreasing f_{ELM} mainly at moderate heating power. This is in agreement with the mechanism proposed in the previous sections for which lower f_{ELM} allows higher N concentrations in the plasma. However, too low f_{ELM} leads to impurity accumulation as discussed during this chapter and shown in detail in chapter 7. Therefore, the

optimum f_{ELM} is given by the balance between these two conditions. Panel c) shows the tungsten concentration c_W (average value between core and edge) c_W vs f_{ELM}. The points are distributed in two groups: group 1), circled in black, contains data points representing mainly discharges with N-only and with nitrogen combined with argon or krypton at 15 MW. The tungsten concentration characterising this group spans from a value of $3{\cdot}10^{-5}$ (seeded discharges) up to $5.3 \cdot 10^{-5}$ (unseeded cases). The orange group, instead, represents the high power discharges at 18 and 20 MW obtained by nitrogen plus argon and krypton seeding. Their tungsten concentration is much lower than the concentration of the red group with an average value of about $1.3 \cdot 10^{-5}$. The plot shows that when argon and krypton are injected at high powers, low W concentrations of about $1 \cdot 10^{-5}$ can be obtained. Instead, when argon and krypton are injected at lower powers, the W concentration is similar to the values which are reached with N only. For the magenta and the blue points it is possible to identify a trend whereby the W concentration decreases with a lower f_{ELM} (see arrows). The dependence of tungsten concentration on the ELM frequency is modelled in chapter 7.

In this chapter it was mentioned that the improvement in confinement appears to be related to the ELM frequency. To further investigate this point, the relative ELM energy loss $\frac{W_{ELM}}{W_{MHD}}$ is plotted against the ELM frequency in plot d). The ELM energy loss is calculated as the drop of W_{MHD} associated with one ELM. W_{MHD} is calculated with CLISTE. The plot demonstrates that impurity seeding reduces the average ELM loss. The group marked in black contains a few non seeded phases at the highest $\frac{W_{ELM}}{W_{MHD}}$ around 0.035 and mainly N seeded phases performed at 10 and 15 MW with a reduced ELM energy loss. All of these phases have a relatively high f_{ELM} between 170 and 220 Hz. The reduction of the energy loss with nitrogen seeding has been already pointed out in previous works [79, 84]. In [79], it was shown that nitrogen seeding allows values of $\frac{W_{ELM}}{W_{MHD}}$ between 0.02 and 0.03. In this thesis, not only this result is confirmed, but it is shown that seeding of medium-Z impurities in addition to nitrogen injection allows further reduction of $\frac{W_{ELM}}{W_{MHD}}$ by a factor of 2.

The reduction of the energy loss per ELM with seeding is an important observation since for large devices the energy impact on the plasma facing components can be so large to cause melting and therefore it is desirable to reduce it. The effect of core seeding can be broken into two different groups: the group circled in blue, which is characterised by a very low energy loss value contains mainly discharges with Ar. The group in red contains both Ar and Kr with an energy loss intermediate between the 2 other groups but with a lower f_{ELM} between 80 and 140 Hz. Thus, argon at very high powers allows a significant reduction of $\frac{W_{ELM}}{W_{MHD}}$ but without a decrease in f_{ELM}. A relevant reduction of f_{ELM} with slightly higher values of $\frac{W_{ELM}}{W_{MHD}}$ is obtained with Kr at all heating powers and with argon but only at 15 MW. In the case when a reduction of f_{ELM} is desired while keeping low the ELM energy loss, Kr appears to be the better choice. Ultimately, the use of Kr can improve the performance through a reduction of f_{ELM} but the latter must be controlled to avoid an excessive high concentration in the confined region.

6.6 Discussion

The confinement studies presented in this chapter provide evidence that edge localised radiation losses do not impact the global confinement, whereas central radiation must be limited and controlled. It was shown that, even using high-Z radiators, if the core radiation losses are controlled and the ELM frequency is kept high enough to avoid radiative collapse, an even higher confinement than possible with N-only can be achieved. The results of the analysis conducted here are summarised in the following:

- Nitrogen concentrations in the plasma induce higher pedestal temperatures keeping the density unchanged and therefore leading to higher pedestal pressure.
- The transport analysis indicates a strong role of the critical gradient length in setting profile features. As a result the global confinement depends strongly on the pedestal values. The pedestal confinement improvement obtained with N is propagated to the core via stiffness. Note that a higher confinement can be reached with plasma shaping which increases the density likely due to a reduction of f_{ELM}.
- Key role of f_{ELM}: - Discharges with N+Kr (stable cases) exhibit an increased confinement here attributed to the increase of the N concentration in the plasma due to a lower f_{ELM}. - Discharges with N+He are characterised by higher f_{ELM} which causes a reduction of nitrogen in the plasma contributing to a confinement degradation.

The confinement improvement observed with both low and high-Z radiators can be explained by an increased nitrogen concentration which increases the plasma stored energy by increasing the temperature at the pedestal. However, since impurities contribute to Z_{eff}, this might indicate that the higher Z_{eff} can also contribute to the confinement improvement, independent of the chosen impurity. The effect of Z_{eff} on the pedestal stability is currently under investigation [80].

”Per aspera ad astra sic igitur ad sidera.”

— Seneca, Hercules furens

Chapter 7

Modelling of the radiation and impurity evolution in presence of ELMs

7.1 Motivation

In section 6.2 the non-coronal radiation model PIRT (Pedestal Impurity Residence Time) developed during work was presented. In this model, the non-coronal effects are described by the parameter $n_e \cdot \tau$, where n_e stands for the electron density and τ for the residence time of the impurities. As we have seen, the crucial point is the determination of τ. In the pedestal τ is assumed to scale with the inverse of the ELM frequency: $\tau_{ped} = 1/f_{ELM}$. This criterion is based on the fact that the pedestal is strongly influenced by ELMs: they flush out impurities and cause a reorganisation of the profiles at every crash. Therefore the residence time of impurities cannot exceed the inverse of the ELM frequency. Using $\tau_{ped} = 1/f_{ELM}$, a very good agreement is found between the PIRT model and the bolometric measurements at the edge where non-coronal effects take place. To assess the validity of the assumption that f_{ELM} determines τ_{ped} and understand why under such assumption the experimental behaviour is well reproduced, a time dependent modelling of the radiation and impurities in presence of ELMs has been carried out with ASTRA coupled to STRAHL (section 4.3). The aim is to model the radiation and the evolution of the impurities from the separatrix inwards with particular attention to the pedestal region and ELM-induced transport: coupling the transport effects on the ionisation stages with the reaction of the background profiles. At the beginning, the modelling effort was focussed on reproducing the experimental discharge #29254 with nitrogen seeding which exploits the high radiation scenario presented in section 6.3 and is analysed by power balance analysis with the TRANSP code in section 6.4.1. Because of the full tungsten wall of ASDEX Upgrade, the model includes both N and W. The density and the radiation

evolution of nitrogen and tungsten was simultaneously simulated for the first time. The physics questions which are addressed in this modelling section are:

- What are the physical parameters required to reproduce the temporal evolution of the impurities and radiation under non-coronal conditions?
- Which ELM model is able to reproduce the experimental radiation behavior?
- What are the differences in the time evolution of N and W?
- How do both impurities respond to a change of f_{ELM}?

In order to answer these questions, a transport model was devised and parameters were varied extensively until the experimental features of discharge #29254 were reproduced. The ELM crash was modelled as a diffusive and a convective transport. Scans of f_{ELM} were also performed in both diffusive and convective cases to investigate the effect of f_{ELM} on P_{rad}. The most representative case of f_{ELM}=10 Hz for the lower part of the f_{ELM} scan is presented for both ELM models. For lower f_{ELM} values a radiative collapse occurs. The modelled radiation was compared with the radiated power density measured by diode bolometers described in 5.3.7. Finally, the comparison of the modelled radiation with the PIRT model is shown.

7.2 Energy and particle transport model

The tasks described above require a complex modelling effort which was carried out with ASTRA coupled to STRAHL.The boundary conditions in ASTRA are set at the separatrix by experimental values while in STRAHL they are set at the plasma "limiter".

The following input parameters are given in ASTRA:

- Shape of the separatrix, I_p and B_T.
- Geometric quantities of vessel and plasma.
- Experimental electron density n_e, electron and ion temperatures T_e and T_i which were used to set the boundary conditions at the separatrix.
- Power deposition profiles of NBI to electrons and ions $P_{NBI,e}$ and $P_{NBI,i}$ and deposition profiles of the driven current by NBI j_{NBI} are calculated using NUBEAM.
- Power deposition profiles of the ICRH to electrons and ions $P_{ICRH,e}$ and $P_{ICRH,i}$ obtained with the wave deposition model TORIC4 [85] inside TRANSP.

- Power depositions profiles of the ECRH to electrons P_{ECRH} and the driven current (j_{ECRH}) calculated with TORBEAM.

The current profile is evolved assuming neoclassical resistivity and setting the experimental total plasma current as boundary condition. The bootstrap current is also taken into account using the Sauter-Angioni formula [86]. The particle source takes into account the ionisation from neutrals, the contribution of the NBI and of the recycling flux through the separatrix. The radial distribution of the neutrals is calculated in the subroutine NEUT, implemented in ASTRA, which solves the kinetic equation for a neutral distribution in slab geometry [41]. To summarise, every STRAHL run needs:

- Plasma geometry provided by SPIDER.
- Plasma background profiles which in this work are provided by ASTRA.
- Atomic data for ionisation, recombination and emission of impurities taken from the ADAS database.
- Transport coefficients as presented below.

7.2.1 Core and pedestal modelling

The electron and ion temperatures, as well as the electron density, are modelled in ASTRA. The impurity density transport and radiation are simulated in STRAHL which takes the non-coronal effects due to transport into account. For the modelling the following facts are important: in H-mode plasmas, the very steep gradients in the ETB collapse during an ELM and recover during the inter-ELM phase. It was found experimentally that the impurity transport between ELMs is well described by neoclassical theory including both diffusion and pinch [30]. This implies that impurities in the ETB are subject to a neoclassical pinch leading to steep density gradients which are flattened during ELMs. Therefore, it is possible to identify two main temporal phases: the short phase during the ELM, characterised by a strongly increased transport and the phase between ELMs described by neoclassical theory. According to neoclassical theory, the inward pinch becomes stronger as Z increases. Consequently, each impurity has a different gradient in the H-mode ETB.

The presence of heat and particle sources needed to rebuild the pedestal after an ELM crash and the transport effects which determine the heat and particle profiles are essential factors in the simulations. Taking into account all these elements, a semi-empirical transport model was built as follows.

- Core T_e, T_i modelling: In the core, T_e and T_i are modelled assuming turbulent and neoclassical transport. For the turbulent transport the critical gradient model has

been employed (see section 2.5). For the neoclassical contribution, the neoclassical electron heat conductivity has been used for the electrons, while the neoclassical ion heat conductivity has been used for the ions, with $\chi_e^{NEO} << \chi_i^{NEO}$.

- Pedestal (ETB) T_e, T_i modelling: In the pedestal both T_e, T_i are modelled assuming neoclassical ion heat conductivity [86]. The neoclassical conductivity for the electrons is in fact two orders of magnitude too low to explain the experimental data. Therefore, the empirical choice $\chi_e = \chi_i$ has been used. The pedestal is 2.5 cm wide from the separatrix inwards. The diffusivities are prescribed such that they match the ELM-averaged pedestal top temperature profiles. The boundary conditions are set at the separatrix by experimental values.

- Core n_e modelling: The evolution of n_e is obtained assuming purely turbulent transport in the core. The turbulent part of the particle diffusivity D_n is chosen as a fraction of $\chi_{e,turb}$. Since the particle source in the core is rather small in steady-state the convection velocity V is chosen such that the drift parameter fulfills $-\frac{V}{D_n} = \frac{\nabla_{n_e}}{n_e}$. With this choice the normalised experimental density gradients are well reproduced.

- Pedestal n_e modelling: In the pedestal, the evolution of n_e is obtained setting $D = 0.7 \cdot \chi_i^{NEO}$. In the following section, whenever the density peaking is mentioned, the following definition is used: $n_{peak} = \frac{n_0}{< n >_{Vol}}$ with n_0 being the density on axis and $< n >_{Vol}$ the volume-averaged density. Since frequent ELMs erode the pedestal, the source is varied to maintain the pedestal top electron density at the target value.

- Core n_z modelling: In the core, the turbulent particle diffusivity of the impurities is chosen as a fraction of χ_i. The turbulent convection velocity is set to zero.

- Pedestal n_z modelling: The impurity pedestal transport is at neoclassical level. The neoclassical contribution is computed in STRAHL using NEOART [47]. NEOART produces the diffusion coefficient D_{neo} and the convective velocities V_{neo} for all impurity species for a given magnetic equilibrium, electron and ion temperature profiles and density profile. The impurity turbulent convection is set to zero. The impurities considered in this work are nitrogen (from impurity seeding) and tungsten (from the wall). Their source is set 2.0 cm outside the separatrix in STRAHL. Its magnitude is chosen such that the experimental P_{rad} and impurity concentrations are reproduced once the equilibrium is reached. The SOL is not modelled in ASTRA, but it is used in STRAHL for the impurity evolution to the separatrix and to the limiter. The SOL parameters are adjusted in order to get the required impurity concentrations in the pedestal. More details about the SOL can be found in [45].

Example profiles of the electron heat diffusivity χ_e and the electron particle diffusivity D and electron particle convection V are shown in figure 7.1 a) and b). Profiles of the neoclassical impurity diffusion coefficient D_{neo} and the neoclassical impurity convection velocity V_{neo} are shown in figure 7.1 c).

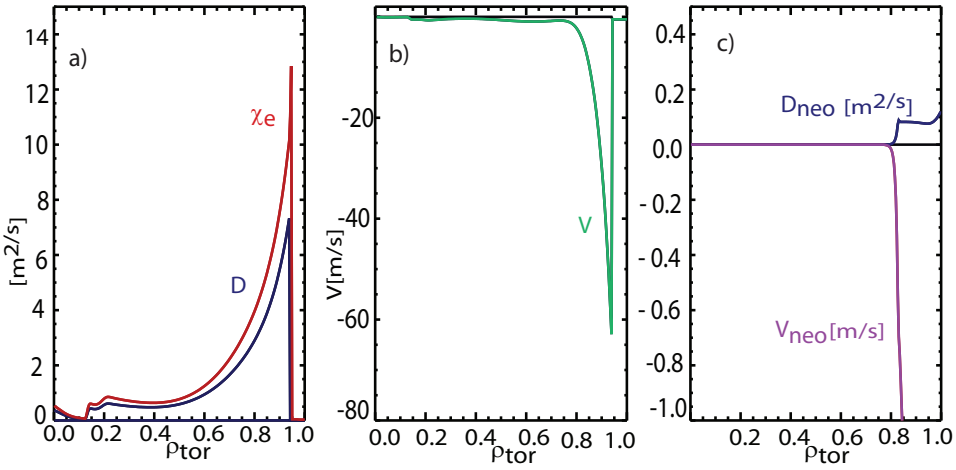

Figure 7.1: a) Electron heat diffusivity χ_e and electron particle diffusivity D, b) electron particle convection V, c) impurity diffusion D_{neo} and impurity convection coefficients V_{neo} from NEOART.

7.2.2 ELM modelling

The ELMs can be modelled based on two different assumptions. Both consider the fact that ELMs induce a high transport during their short crash.

- Diffusive ELM model: ELMs are simulated as an instantaneous increase in heat and particle diffusivities in the "ELM affected area" which is 2.5 cm wide ($\rho_{tor} = 0.92 - 1.0$). The diffusive transport during the ELM flattens the profiles. They steepen again during the inter-ELM phase due to sources and the presence of the neoclassical inward pinch.

- Convective ELM: An outward convective velocity causes a loss of the impurity content. The instantaneous increase of the convective transport coefficients in the ELM affected area is applied to both particle and impurity convection velocities.

In both cases, the ELM frequency is set according to the experiments. In the following simulations an ELM lasts for 2 ms. In this time interval the increase of the diffusivities (diffusive case) or of the convection velocity (convective case) in the ELM affected area is adjusted to reproduce the experimental variation of the line integrated density measured by the H-5 channel from interferometer measurements and the stored energy obtained from the equilibrium reconstruction.

7.3 Modelling results

7.3.1 Diffusive ELM model

The diffusive ELM model is applied to the N seeded discharge #29254. Details about this discharge were given in section 6.4.1. In the following analysis, we will refer to this discharge as the reference case, characterised by an ELM frequency of 143 Hz.

Since we are interested in studying the impurity and radiation evolution in presence of ELMs, the results presented in this section are focussed on the edge of the confined region. This is illustrated by the behavior at several radial positions in the pedestal region: the time evolution at $\rho_{tor} = 0.80$, $\rho_{tor} = 0.90$, $\rho_{tor} = 0.95$ and $\rho_{tor} = 0.98$ is depicted in figure 7.2. It presents the evolution of the electron temperature and the electron density for all radial positions mentioned above. The oscillations of T_e and n_e are correlated with the ELM period. The ELM crash induces a drop of the electron temperature and density which then recover until the occurrence of the next ELM crash.

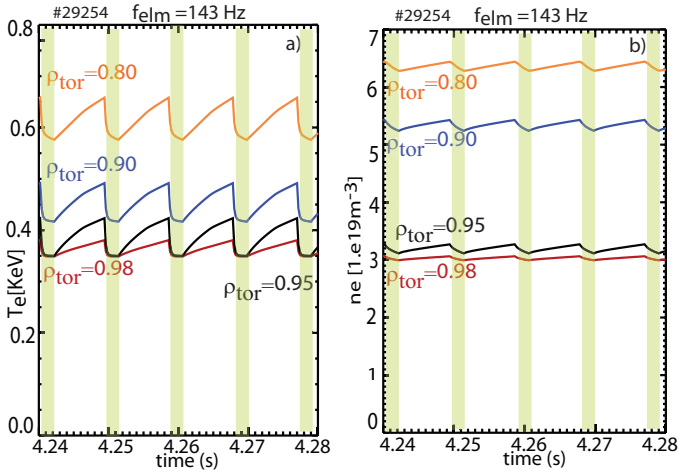

Figure 7.2: Evolution of a) electron temperature, b) electron density at different radial positions in the pedestal: $\rho_{tor} = 0.8$ (in orange), $\rho_{tor} = 0.9$ (in blue), $\rho_{tor} = 0.95$ (in black) and $\rho_{tor} = 0.98$ (in red). The green zone represents the ELM crash.

The time evolution of both nitrogen and tungsten densities are shown in figure 7.3 a) and c). At the ELM crash the impurity density of both species drops at $\rho_{tor} = 0.8$, $\rho_{tor} = 0.9$ and at $\rho_{tor} = 0.95$. The densities during the ELM crash itself show different features at different radial positions. At $\rho_{tor} = 0.95$ the drop is very quick while the recovery takes place on a longer time scale. At $\rho_{tor} = 0.90$ the drop is less steep, while the recovery happens at the same time scale as for $\rho_{tor} = 0.95$. The radial position $\rho_{tor} = 0.80$ is, as expected, less perturbed by the ELM crash compared to the other radial position, since it is located outside the ELM affected area. The N density profile (panel b)) also shows that at $\rho_{tor} = 0.80$, the inter-ELM phase and the ELM crash phase are in close proximity. For N the onset of a saturation behaviour is already visible in these time traces. This

aspect will be discussed in detail later. A different situation occurs at $\rho_{tor} = 0.98$ where both impurities exhibit a peak in the time traces. This behaviour can be understood by looking at the W profile in panel d). Panel b) and d) compare the density profiles of nitrogen and tungsten during the inter-ELM phase, at the ELM crash start and at the maximum ELM depletion: the diffusive nature of the ELM model leads to a flattening of the density profiles during an ELM. At the pedestal top, the impurity density decreases compared to the density in the inter ELM phase. However, near the separatrix the nitrogen density increases. In more detail, the radial position at $\rho_{tor} = 0.95$ is still dominated by profile flattening, consistent with the drop observed in the time traces. The turning point lies around $\rho_{tor} = 0.96$. From this position outwards, the density profile of both impurities experience an increase which is also visible in the time traces. The reason for this behaviour observed in both the time traces and in the profiles can be explained by the fact that the ELM crash causes a transient perturbation which steep the gradients transiently. In order to conserve the particle flux, the steepening of the gradients has to be re-equilibrated by the transport. This is the reason why the profiles are flattened further inside the ELM affected area. This behaviour is consistent with the experimental observation that the second crash phase is suppressed when introducing N seeding and the gradients steep directly after the crash [79].

The time traces of the modelled radiation of nitrogen and tungsten are presented in figure 7.4 panel a) and d). For all radial positions, the N radiation from STRAHL is significantly higher than that from coronal calculations (dashed) emphasising the importance of non-coronal effects for low-Z elements at the plasma edge which was highlighted in section 6.2. For W, coronal calculations yield a radiation very similar to STRAHL, indicating that for high-Z elements the coronal equilibrium is a good approximation even at the edge. This point is illustrated later in figure 7.6. The outermost region of nitrogen radiation exhibits a saturation behaviour, which is not observed in the W radiation. This saturation behaviour suggests that a change in f_{ELM} may not change the nitrogen radiation behaviour, while the tungsten flush out may depend on f_{ELM}. This was investigated with the f_{ELM} scan of which the most representative case (f_{ELM}=10 Hz) is shown later. For N radiation, the outermost radial position ($\rho_{tor} = 0.98$) emits the highest radiation in agreement with the fact that N losses occurs at the very edge through the line components which give rise to the sharp peaks in the radiative loss function. For W, instead, it is the innermost region ($\rho_{tor} = 0.80$) to emit the highest radiation. This is consistent with the fact that for high-Z impurities the bulk of the radiation comes from the interior of the plasma: as the W ions penetrate deeper into the plasma, they reach regions with higher T_e and therefore ions with a higher charge number take place and radiate strongly.

Interestingly, at the ELM crash, the outermost region of the N radiation shows a drop in P_{rad} while all other regions experience an increase. For W, instead, all radial positions show a drop at the ELM crash while the outermost region exhibits a peak. Such behaviour is a consequence of the combined effect of the decrease in temperature and density due to the ELM crash with the reaction of L_Z at the ELM crash. This can be also seen in the L_Z and P_{rad} profiles of figure 7.4 (panel e) and f)).

Panel b) and c) of figure 7.4 show the effect of the ELMs on the nitrogen radiative loss

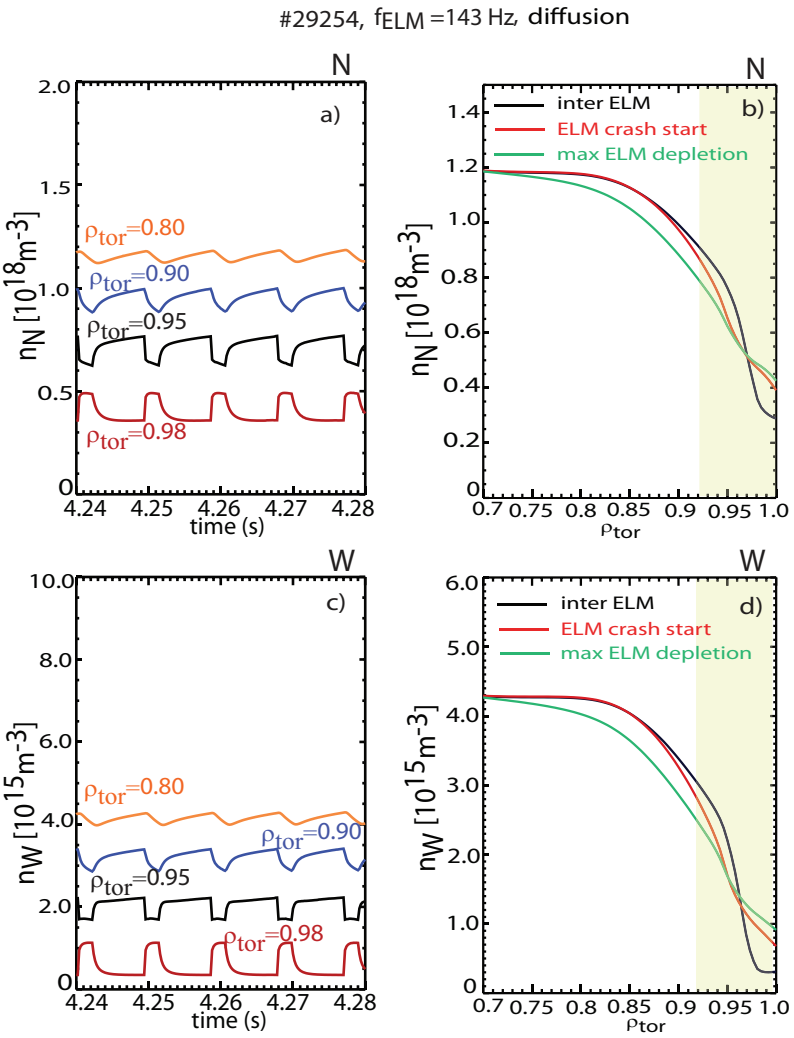

Figure 7.3: Time traces of a) N density, c) W density. In red at $\rho_{tor} = 0.98$, in black at $\rho_{tor} = 0.95$, in blue at $\rho_{tor} = 0.90$, in orange at $\rho_{tor} = 0.80$. Effect of ELMs on b) nitrogen density profile; d) tungsten density profile. The green zone represents the ELM-affected area.

function L_Z and on the nitrogen radiation profiles: despite the flattening of the nitrogen density profile caused by the ELM, the radiation increases. The increase in P_{rad} is caused by the increase of L_Z at the ELM crash.

Indeed, the radiation enhancement can be understood looking at the ionisation stage evolution, figure 7.5. It shows the fractional abundance of nitrogen in the inter ELM phase (in black) and during the ELM (in red) as a function of the radius. The zero point on the x-axis represents the separatrix. The ELM-induced diffusion causes the broadening of the shell-like structure of the ionisation stages symmetrically around the local ionisation-recombination balance. Due to the high diffusion, the outer region of the ionisation shell is flushed out at the separatrix while the inner region is broadened and the maximum is shifted radially inwards. The radiation from impurities depends on their ionisation stage and it comes mainly from non fully stripped ions during the ionisation processes (see

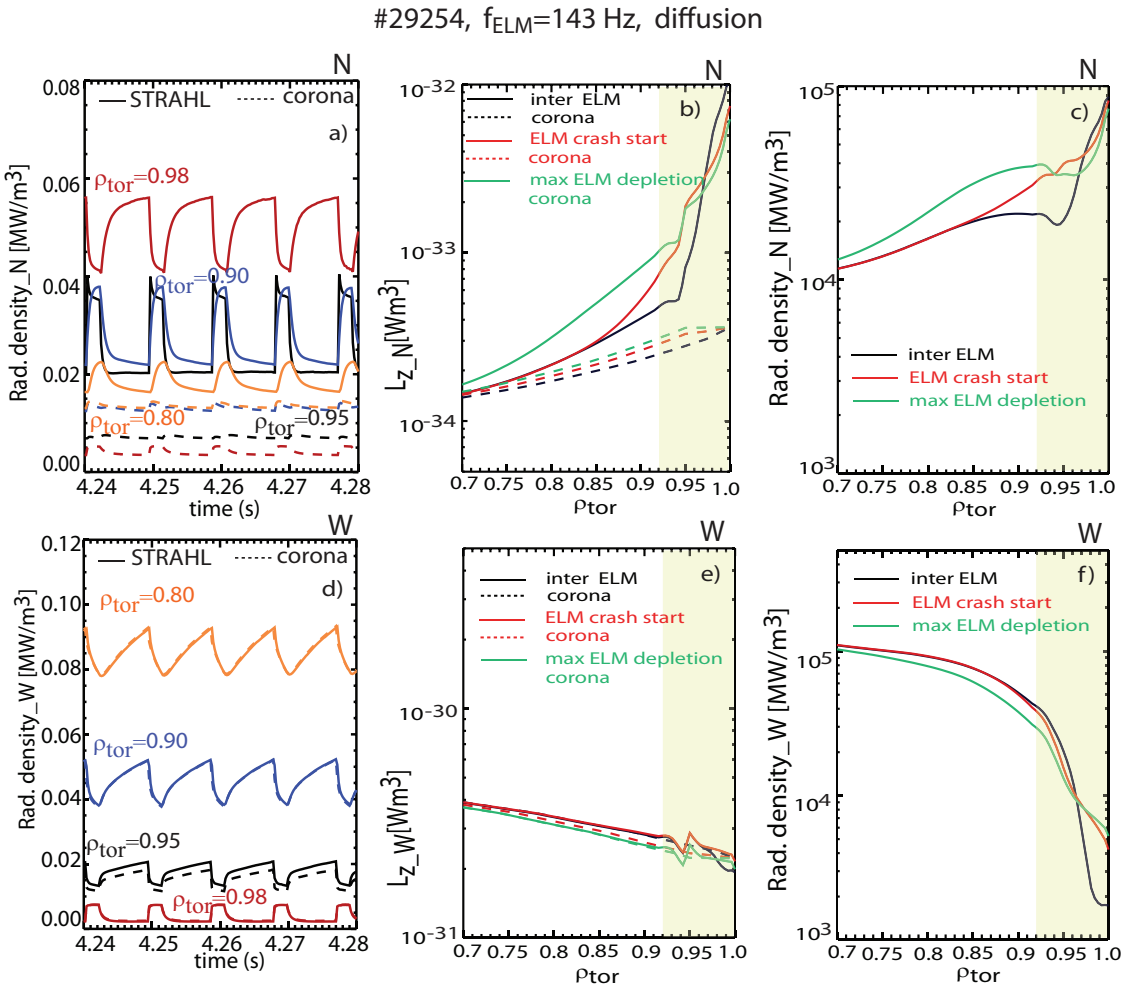

Figure 7.4: Time traces of the modelled radiation from STRAHL at different radial positions. The corresponding dashed lines represent the coronal values. Radiated power density of a) N, d) W. Effect of ELMs on L_Z profile of: b) N, e) W. Effect of ELMs on radiation profile of c) N, f) W.

chapter 3). The ionisation stages number 5 (He like N) and 6 (H like N) shown in figure 7.5 are broadened by the radial transport and shifted inward. Hence, the ionisation stages are at higher temperatures compared to the equilibrium one and accordingly they will be less ionised giving rise to a higher level of radiation. This is the so-called non-coronal radiation discussed in section 3.1 and 6.2. Panel b) and e) of figure 7.4 show also the L_Z evolution in coronal equilibrium (dashed lines). For nitrogen, the two calculations agree very well for $\rho_{tor} < 0.6$ (not shown). For $\rho_{tor} > 0.6$ outwards they deviate significantly. It is essential to stress that since coronal calculations do not take into account the transport effects, the comparison between STRAHL and the coronal results enables the disentanglement of the contributions due to the temporal evolution of n_e and T_e profiles from the transport effects as follows:

Panel b) of figure 7.4 reveals that in coronal equilibrium L_Z changes only slightly from the inter-ELM phase to the intra-ELM phase, while the STRAHL calculations show a

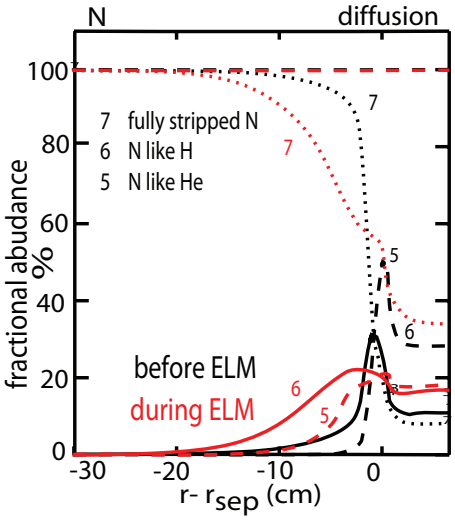

Figure 7.5: Fractional abundance of N in the inter ELM phase in black and during ELM in red. The zero point on the x axis represents the separatrix.

significant enhancement of L_Z. This suggests that the radial transport during the ELM phase, dominates the pedestal nitrogen radiation.

A different situation is found for tungsten. The effects of ELMs on L_Z and radiation profiles are shown in panel e) and f). In figure 7.3 d) it was shown that ELMs cause a flattening of the W density profile as well as of the nitrogen profile (panel b). In general there are two effects on L_Z: one is the deviation from coronal values due to the shell broadening and one is the temperature decrease which occurs during an ELM. In contrast to nitrogen, tungsten is well described by the coronal equilibrium and accordingly the variation of the tungsten L_Z within the ELM phase is rather small. However, the effect of the decrease in temperature during the ELM phase remains, which, given the tungsten L_Z shape in the considered temperature range, leads to a decrease of L_Z when going from the inter-ELM phase to the ELM phase (figure 7.4 e)). Following the trend of n_W and L_Z, P_{rad_W} decreases for $\rho_{tor} < 0.95$ during the ELM phase. An inversion of this trend is observed for $\rho_{tor} > 0.96$ consistent withthe radiation increase observed in the time traces.

The reason why non-coronal effects are important for N but not for W is explained in the following. First, the shape of L_Z as a function of T_e as shown in figure 7.6. The shape of L_Z for N is such that a small deviation from coronal values leads to a significant change in L_Z for the low T_e range of the pedestal region (100-500 eV). L_Z also spans over a wide range. This is due to the dominance of the line components for low-Z impurities where the peaks and the troughs reflects the shell-like structure (see also section 3.1). The L_Z shape for W implies a smaller relative change when deviating from coronal values. For W a deviation in the $L_Z - T_e$ domain has a much smaller impact on L_Z in the considered temperature range.

Second, the recombination $\alpha_{rec.}$ and ionisation $S_{ion.}$ rates which were discussed in section 4.2 have to be considered. Their rates increase with the atomic number Z: $\alpha_{rec.} \propto Z^3$ and

$S_{ion.} \propto Z^2$. More in detail, the ionisation equilibrium equation reads:

$$\frac{\partial}{\partial t} n_z = -\nabla \cdot \vec{\Gamma}_z + Q_z \tag{7.1}$$

where $-\nabla \cdot \vec{\Gamma}_z$ is the transport term and Q_z is the source term of the ion density n_z. The source term written in terms of the ionisation and recombination rates reads:

$$Q_z = -(n_e \cdot S_z + n_e \alpha_z) \cdot n_z + (n_e \cdot S_{z-1}) \cdot n_{z-1} + (n_e \cdot \alpha_{z+1}) \cdot n_{z+1} \tag{7.2}$$

The term $\vec{\Gamma}_z = D\nabla n - vn$ scales with Z, while the source term Q_z, which contains the ionisation S_{ion} and recombination α_{rec} rates, increases with Z^3.

This means, that in case of W the ionisation equilibrium is reached much faster than for nitrogen and explains why at the typical edge temperatures, W is in coronal equilibrium while N is not. Note that due the high recombination rate, the spectrum of W is characterised by hundreds of spectral lines at similar wavelength, such that the different shells overlap forming a quasi-continuum.

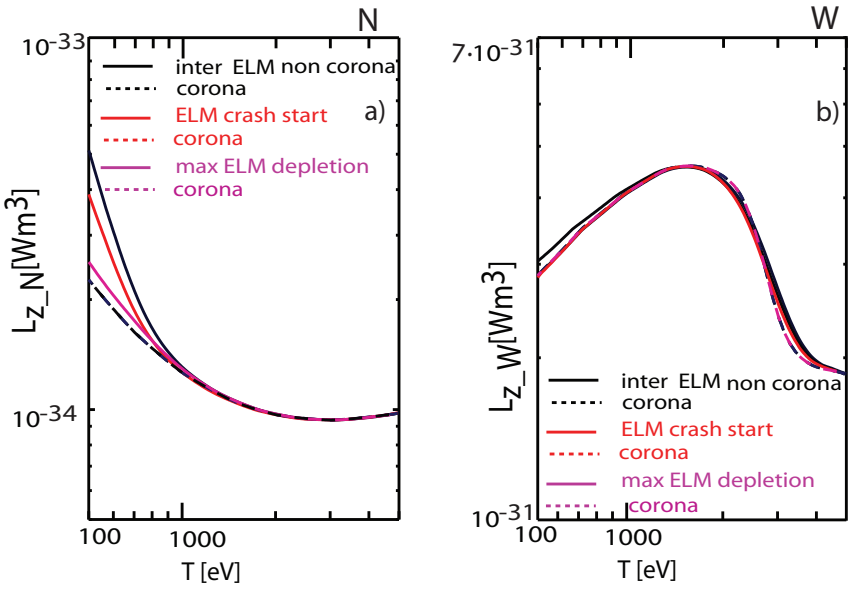

Figure 7.6: L_Z vs T_e: a) Nitrogen b) Tungsten.

Effect of ELM frequency in the diffusive ELM model

Figure 7.4 revealed differences in the behaviour of nitrogen and tungsten densities in the inter ELM phase. In order to investigate the different responses of nitrogen and tungsten to a change of f_{ELM}, a scan of f_{ELM} has been performed. The reference discharge has been modelled assuming different ELM frequencies while keeping the average ELM energy loss constant: $\delta W_{loss} \cdot f_{ELM} = const$, i.e. less frequent larger ELMs give the same contribution as more frequent smaller ELMs [84, 87]. In the following, the case with the lowest achievable f_{ELM} (10 Hz) before the occurrence of a radiative collapse is presented.

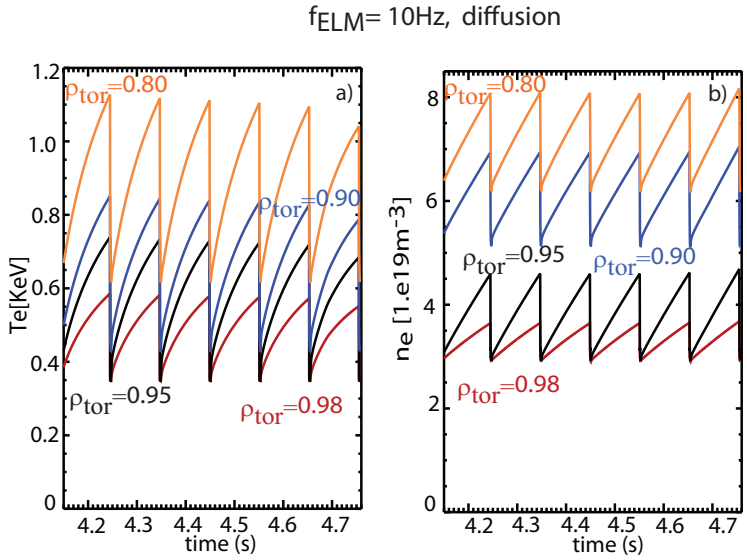

Figure 7.7: 10 Hz case. Time evolution of a) electron temperature, b) electron density at different radial positions in the pedestal: $\rho_{tor} = 0.8$ (in orange), $\rho_{tor} = 0.9$ (in blue), $\rho_{tor} = 0.95$ (in black) and $\rho_{tor} = 0.98$ (in red).

Figure 7.7 depicts the time evolution of T_e and n_e similar to figure 7.2. Since the average energy loss has been kept constant, here the ELM crash is much bigger than in the reference case (f_{ELM}= 143Hz). It is important to stress that the profile recovery depends on the radial position and on the amplitude of the crash itself. The greater the crash is, the greater the changes in the local gradients are. In addition, the time interval between two ELMs is long enough for each quantity to have time to develop its profiles. However, saturation is still not reached. This is a consequence of the low inter-ELM neoclassical transport coefficients. Note that in the f_{ELM} scan these transport coefficients are the same as used for the reference phase.

The evolution of the nitrogen and tungsten densities is shown in figure 7.8 a) and c) similar to figure 7.3 a) and c). The nitrogen density stays at the same level, with a slight increase only starting at 4.6 seconds probably due to a temperature effect caused by W accumulation. The tungsten density in fact increases with time leading to radiation collapse. The different behavior of N and W can be explained by the different peaking of the edge impurity density profiles. In fact the neoclassical pinch in the inter-ELM phase, and

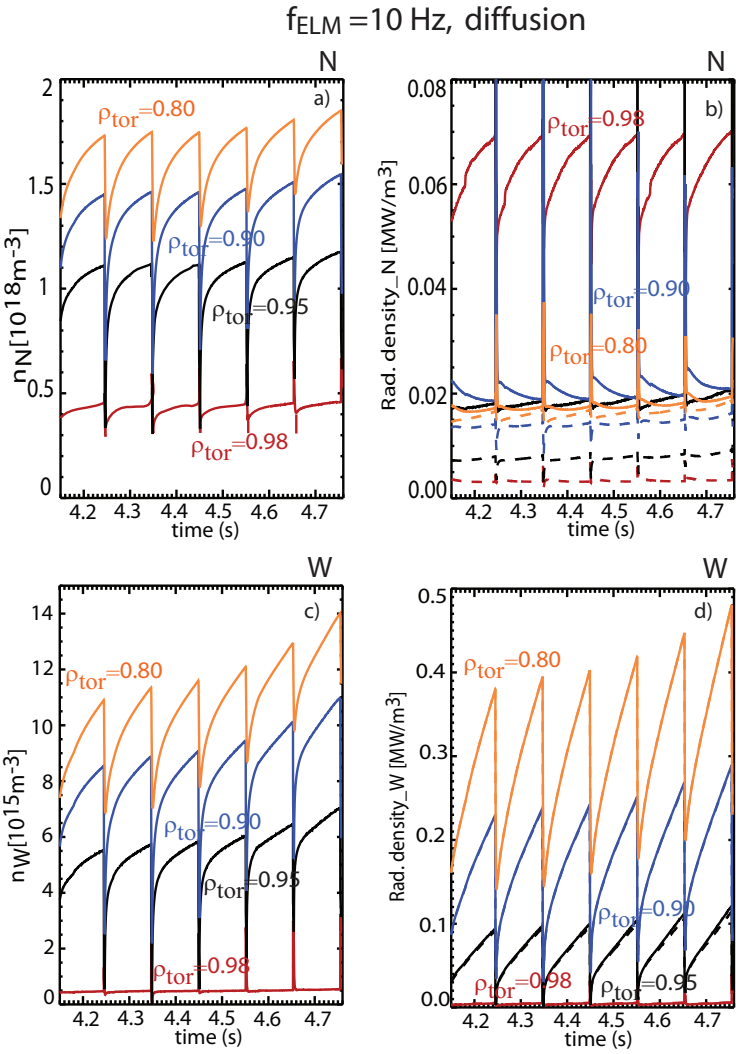

Figure 7.8: f_{ELm}= 10 Hz case: Time traces from STRAHL at different radial positions. Impurity density of a) N, c) W. Radiated power density of b) N, d) W. The corresponding dashed lines represent the coronal values.

therefore the peaking factor, increases with the charge state of the impurity. This means that W has a significantly more peaked profile than that of N. At low ELM frequencies, W has enough time to develop the strongly peaked profile, unlike at high ELM frequencies. This leads to W accumulation in the confined region. The increase in the tungsten concentration in turn leads to higher radiation. The comparison of the tungsten radiation in figure 7.4 d) with the radiation in 7.8 d) indicates that the radiation in the latter case is higher by a factor of 4. This is due to the interplay between the heat flux and the tungsten density and radiation. With a low ELM frequency, W density increases in the confined region leading to higher radiation which reduces the heat flux. A smaller heat flux means that less source is available to drive turbulent transport. Hence, the neoclassical transport effects contribute more. This is particularly important for W since the neoclassical effects increase with Z. In addition, the temperature screening, which tends to counteract the

convective term, gets lower as well. Hence, a self-enhancing mechanism of the W density sets in: the reduced f_{ELM} leads to higher W content and radiation in the confinement region reducing the heat flux. The latter in turns leads to further W accumulation. Panel d) shows that the radiated power density of W increases with decreasing f_{ELM}, while the nitrogen radiation (panel b)) stays roughly at the same level as in the reference case (compare with figure 7.4 a) and c)). The W radiation increase is reflected in the total radiation and is so high that the simulation crashes (collapse by radiation): the radiation power losses become larger than the sum of all heating contributions going to the electrons dissipating T_e while T_i collapses due to the equipartition power forcing $T_i \rightarrow T_e$. Note that in the condition described here, the plasma also crashes in the experiments.

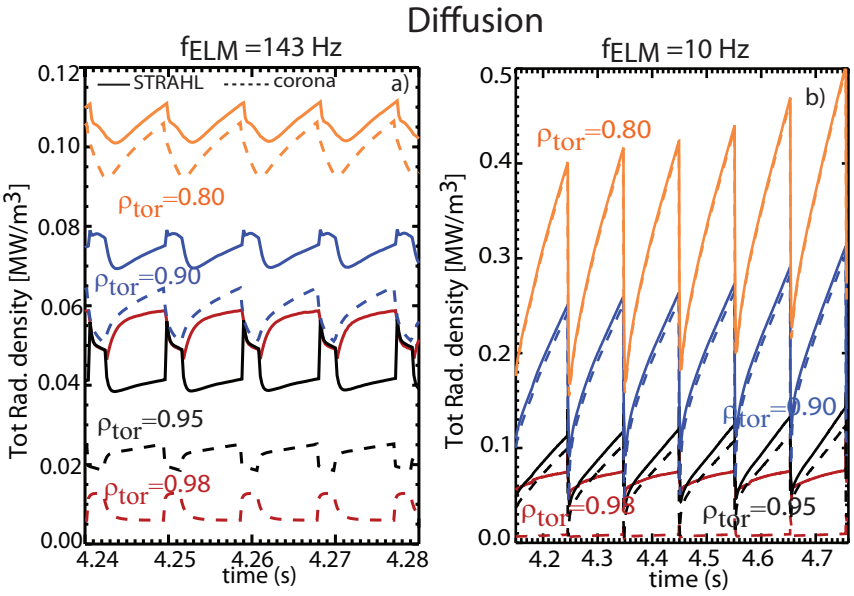

Figure 7.9: Comparison between the total radiated power of a) the reference case with f_{ELM}= 143 Hz and b) the case with f_{ELM}= 10 Hz.

For the reference case (f_{ELM}= 143 Hz), the different contributions from nitrogen and tungsten are combined to the total P_{rad} as follows: P_{rad} at $\rho_{tor} = 0.80$ is governed by tungsten. The ELM contribution of W is modulated by the oscillations in a typical sawtooth-like shape while the N contribution shows a slight modulation with a round shape. At $\rho_{tor} = 0.90$ the peak-like shape coming from nitrogen on the top of the W-sawtooth is significantly more evident. The effect of nitrogen becomes gradually more important going toward the edge. At $\rho_{tor} = 0.95$ the ELM oscillations are dominated by N (in this case a sharp peak). The region at $\rho_{tor} = 0.98$ is dominated by the nitrogen effect. In this region the deviations from coronal equilibrium are also most significant. The comparison between the total radiation of the reference case with P_{rad} obtained for the f_{ELM}=10 Hz case is displayed in figure 7.9. The total radiation increases from 0.11 MW/m^3 to 0.4 MW/m^3 at $\rho_{tor} = 0.80$. The edge region, in particular $\rho_{tor} = 0.95$, clearly shows the ELM crash feature, while the radiation at $\rho_{tor} = 0.80$ is mainly affected by the recovery of the profile. Additionally, figure 7.9 shows that in the f_{ELM} = 10 Hz case, the total P_{rad} is completely dominated by W due to its accumulation. Therefore the non-coronal features of N

radiation are not longer appreciable and the total radiation can be very well described by coronal calculation. Note that in the reference case, the role of the non-coronal nitrogen contribution is evident. The dashed lines of the coronal calculations are well separated from the non-coronal ones. Also they deviate more and more with time.

The scan of f_{ELM} highlights the importance of fast ELMs to prevent W accumulation in the confined region and the accompanied radiation collapse. This is in line with previous studies [88, 89]. The tungsten radiation calculated here increases by a factor of 4 when reducing the ELM frequency from 200 Hz to 10 Hz. This and the fact that in the outer region the tungsten radiation does not saturate, suggest that W radiation depends directly on the ELM frequency.

The nitrogen radiation on the other hand increases only by roughly 27% for the same f_{ELM} range, indicating a more complex dependence. This increase takes place mainly at the very edge ($\rho_{tor} = 0.98$), where nitrogen radiation almost reaches the steady state value at the end of each ELM cycle. As can been seen from the formula $P_{rad} = n_z \cdot n_e \cdot L_z(T, n \cdot \tau)$, several effects have to be taken into account: first, n_N increases by about 50% when f_{ELM} is reduced to 10 Hz. This effect of increased nitrogen content with decreasing ELM frequency is evident both in the modelling and the experiments (see chapter 6). Second the contribution of L_Z has to be considered: On one hand, the strong increase of $\tau_{ped} = 1/f_{ELM}$ also increases L_Z via the parameter $n \cdot \tau$. For this assumption of τ_{ped} in the PIRT model, τ_{ped} is increased by a factor of 15 going from f_{ELM} = 143 Hz to 10 Hz. On the other hand, it was shown experimentally that higher n_N lead to higher pedestal temperatures (see chapter 6), which correspond to a significant reduction of L_Z (see L_Z-T_e figure 7.6 a)). This temperature dependence overcompensates the effect of the ELM frequency via $n \cdot \tau$ on L_Z, so that L_Z decreases by roughly 25% going from 143 Hz to 10 Hz. This again weakens the effect of the nitrogen density increase on P_{rad} and explains why the nitrogen radiation does not respond strongly to such a severe change of f_{ELM}. Assuming coronal equilibrium, which does not consider the $n \cdot \tau$ contribution for L_Z, the increased temperature would lead to a strong underestimation of P_{rad} in the calculation. Hence, a non-coronal model should be applied for nitrogen radiation at the edge in presence of ELMs, as discussed in section 6.2. For W instead, there is no term $L_Z(T)$ to counteract the increase due to $n \cdot \tau$ when decreasing f_{ELM}. There is not an increase of the temperature and the profile is rather flat making the P_{rad} of W really sensitive to a change in f_{ELM}.

Turbulent background scan

A scan of the turbulent diffusion background of the impurities has been also performed. The aim was to demonstrate that the choice, motivated by experimental findings [30], of using neoclassical theory in the pedestal is indeed valid. A turbulent diffusion background D_{turb} for impurities which adds to the neoclassical contribution was introduced to the model. The simulations were performed using D_{turb} =0.001 m^2/s, D_{turb} =0.01 m^2/s, D_{turb} =0.1 m^2/s and setting the turbulent v_{imp}=0 in the core. The main result is that when the pedestal of impurities is dominated by the turbulent transport, the impurity density profiles of both impurities are just flat over the whole profile, in contrast to experimental observations. This property of diffusion occurs when the source is located at the edge. In order to reproduce the experimental impurity density profiles in the pedestal, it seems that the turbulent impurity particle transport has to be below the neoclassical level.

7.3.2 Convective ELM model

In this section, the convective ELM model is presented. In this model a high outward convection is applied during the ELM in the ELM affected area. Since the outward convection of each ELM expels particles, in this case the density of the cold neutrals needed to match the experimental edge density is higher than in the diffusive ELM model. In order to ensure the numerical solution of the transport equation, a discontinuity at the separatrix must be avoided. Therefore, it was assumed that the diffusion and convection velocities propagate in the SOL as well.

Figure 7.10 a) and c) show the time evolution of the impurity densities of nitrogen and tungsten. At the ELM crash, the impurity densities of both species drop at $\rho_{tor} = 0.80$, $\rho_{tor} = 0.90$ and $\rho_{tor} = 0.95$. At $\rho_{tor} = 0.98$, instead, both impurity densities exhibit an increase, however different for the two impurity species. The nitrogen density experiences a quick increase which then decreases again during the ELM crash. For n_W the quick increase is maintained for the entire ELM duration. At the end of the ELM cycle, just as quickly as the increase, the impurity density decreases to the same level as in the inter-ELM phase. Moreover, in the tungsten case, the impurity density at $\rho_{tor} = 0.95$ has already reached the equilibrium. The reason for which the density of both impurities exhibits a peak, although with different characteristics, can be explained by looking at the nitrogen and tungsten density profiles (panels b) and d)). Panel b) shows that the convective ELM erodes the gradients of the nitrogen density. Interestingly during the ELM cycle, for $\rho_{tor} > 0.97$, the nitrogen impurity density first goes up and then down compared to the inter ELM phase, while a "hole" around $\rho_{tor} = 0.95$ is detected. The hump is likely an artifact of the model. Various tests have been performed, the hump can be more or less pronounced but the qualitative behaviour remains a decrease in the confined region and an increase near the separatrix. The W density profile at the very edge is more defined than for N which is due to the stronger neoclassical pinch of tungsten compared to nitrogen. Compared to the diffusive ELM case, the W profile is similar, while the N

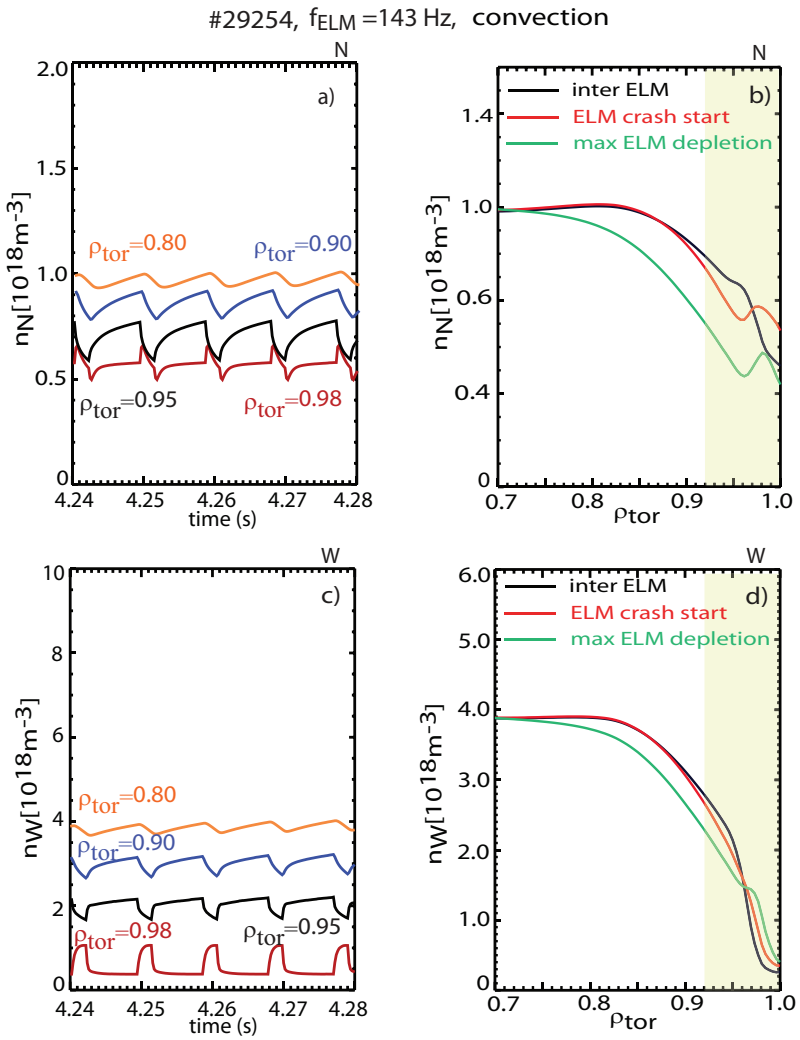

Figure 7.10: Time traces of a) N density, c) W density. Effect of ELMs on: b) N density profile; d) W density profile.

profile is characterised by significant higher values at the outermost part of the confined region and lower values of about 20 % in the core. These different behaviours can be explained by the neoclassical theory which predicts a neoclassical inward pinch increasing with Z (see sections 2.4 and 7.1). This stronger neoclassical pinch is able to counteract the convective effect which tends to expel particles and to erode the pedestal. The result is that, compared to the nitrogen case, the tungsten pedestal is more pronounced and shifted inwards by the stronger pinch. As for the diffusive case, the profiles flatten inside the ELM affected area in order to re-equilibrate the flux. The global effect of convection on both density profiles is to "remove" particles around $\rho_{tor} = 0.95$ and accumulate them around $\rho_{tor} = 0.98$. However, a common feature characterises both impurities and both ELM models: the gradients flatten inside a certain turning point which is located around $\rho_{tor} = 0.95$. At the edge the particle losses are higher and this happens in the diffusive case, as well as in the convective case. The reason is that this particle loss takes place due to an additional transport, independent from the fact that the transport is of a diffusive or

convective nature.

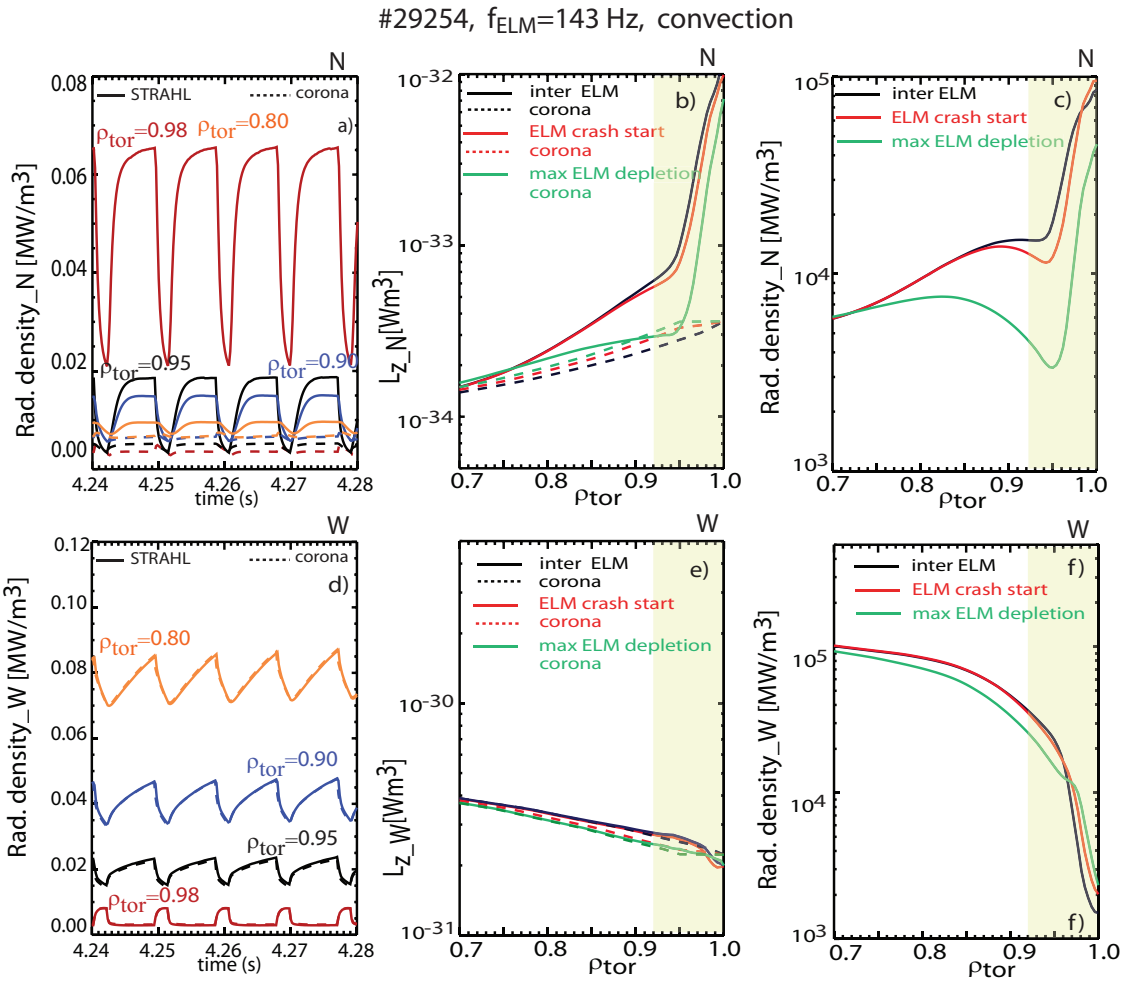

Figure 7.11: Time traces of the modelled radiation from STRAHL at different radial positions. The corresponding dashed lines represent the coronal values. Radiated power density of a) N, d) W. Effect of ELMs on L_Z profile of b) N, e) W. Effect of ELMs on radiation profile c) N, f) W.

Figure 7.11 b) and e) display the nitrogen L_Z and radiation profiles. Following the behaviour of the nitrogen density, P_{rad} increases slightly in the region $\rho_{tor} > 0.98$ at the ELM crash start, while at the maximal ELM depletion the whole profile lies below the inter-ELM phase. In contrast to the diffusive behaviour, both L_Z and P_{rad} decrease during the ELM crash. The effect of convection on the nitrogen ionisation stages is depicted in figure 7.12. The ionisation shells are narrowed and shifted radially outwards, which is the exact opposite situation than in the diffusive scenario. This explains the drop of radiation occurring in the pedestal region (figure 7.11 c) and f)). The ionisation shells are accumulated near the separatrix giving rise to the radiation peak observed at $\rho_{tor} = 0.98$.

The temporal response of the radiated power density of the two impurities is shown in figure 7.11 a) and b)). As mentioned above, because of the gathering of the shells near the very edge, the nitrogen radiation at $\rho_{tor} \sim 0.98$ exhibits a much higher peak in magnitude

than at the other radial positions. At all radial positions, the nitrogen radiation shows a drop. The W radiation, instead, reveals a peak at $\rho_{tor} \sim 0.98$ which follows the impurity density and L_Z behaviours. L_Z and P_{rad} profiles for tungsten are depicted in figure 7.11 e) and f).

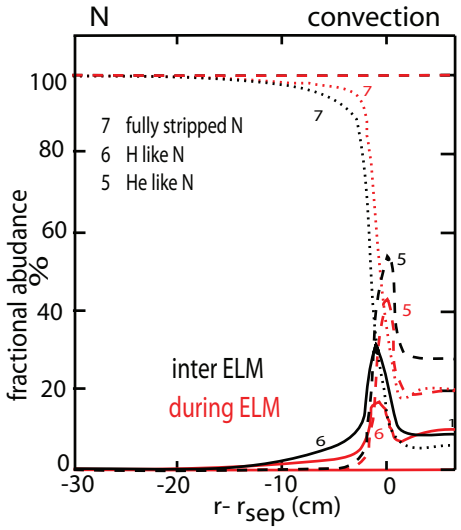

Figure 7.12: Fractional abundance of N in the inter ELM phase in black and during ELM in red. The zero point on the x axis represents the separatrix.

So far we have discussed the impurity and radiation behaviour for both impurities for the diffusive ELM model and for the convective ELM model separately. Now, it is worth comparing directly the results of the two cases. Figure 7.13 shows the comparison for nitrogen (panels a) and b)) and for tungsten (panels c) and d)) radiation. For the nitrogen case, at the ELM crash, the diffusive model leads to a peak in radiation at all radial positions, except $\rho_{tor} = 0.98$. In the convective model, on the contrary, all radial positions experience a drop ($\rho_{tor} = 0.98$ as well).

In the diffusive case, P_{rad} is dominated by the radiation emitted from the radial position $\rho_{tor} = 0.98$ (P_{rad}=0.5 MW/m^3). However, the contributions coming from $\rho_{tor} = 0.95$ and from $\rho_{tor} = 0.90$ are also not negligible ($P_{rad} \sim 0.03$ MW/m^3). Instead in the convective ELM scenario, because of the shell narrowing, P_{rad} is completely dominated by the radiation occurring at $\rho_{tor} = 0.98$.

A very different scenario arises when comparing the ELM diffusive model with the ELM convective model for the tungsten radiation: Its behaviour is the same in both cases (panel c) and d)). Only the magnitude of P_{rad} is, in the convective case, slightly lower than in the diffusive model. The reason is the flush out effect of impurities characterising the convection. In order to understand why P_{rad} of W experiences the same behaviour in both cases, it is important to keep in mind what we have learned from the diffusion case, namely that the ELM-induced transport is not the dominant term for W, while it is extremely important for N and responsible for the non-coronal effects. Therefore, in the case of tungsten, a change of the ELM transport type between diffusion and convection,

does not change the global W behaviour. What matters for W is the change of f_{ELM} as it is shown in the next section.

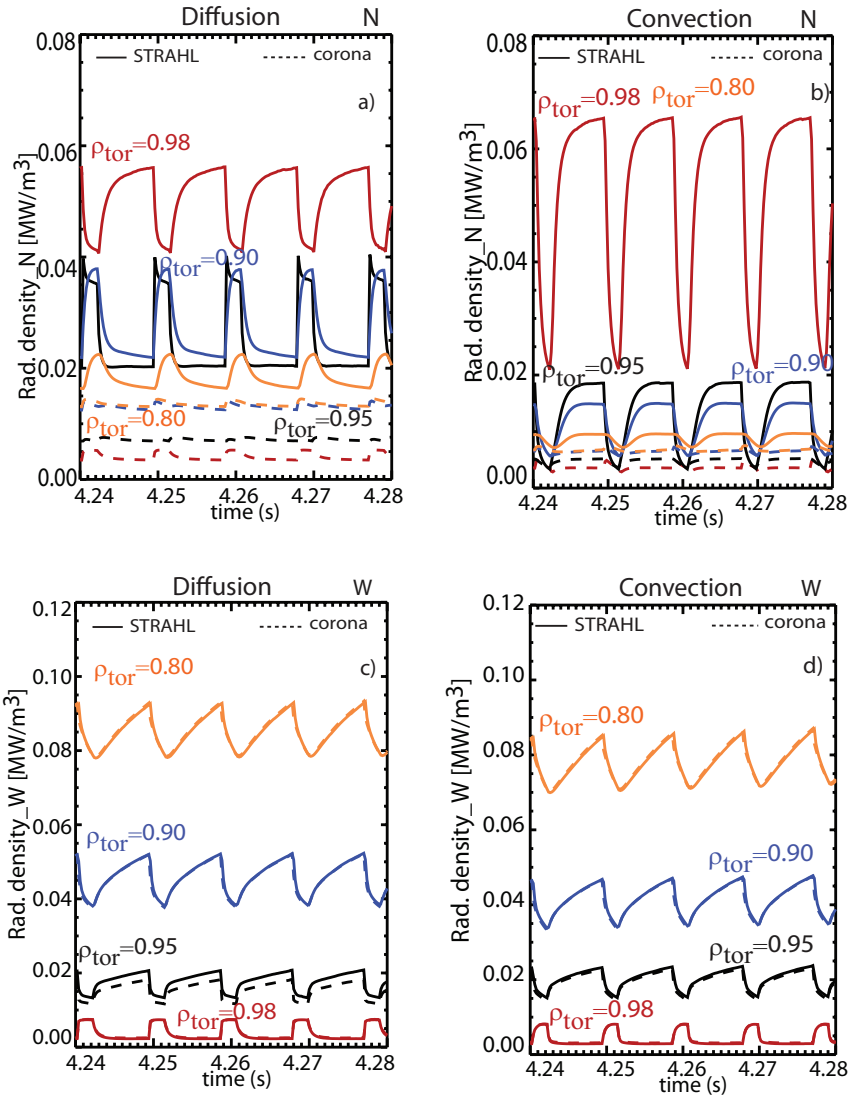

Figure 7.13: Radiated power density of a) N, c) W for the diffusive model. b) N, d) W for the convective model.

Effect of ELM frequency in the convective model

For the convective ELM model a scan of f_{ELM} was also carried out and the case with the lowest f_{ELM} before the radiative collapse (f_{ELM}= 10 Hz) is presented below. The time evolution of the impurity densities and the radiation for both nitrogen and tungsten are depicted in figure 7.14.

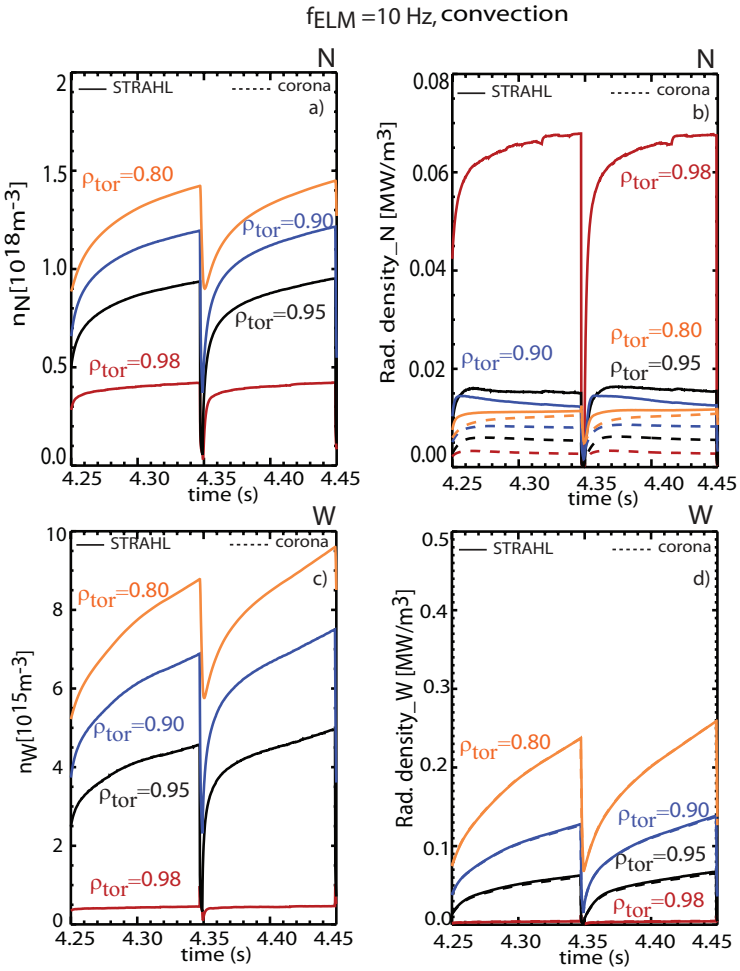

Figure 7.14: f_{ELm}= 10 Hz case: Time traces from STRAHL at different radial positions. Impurity density of a) N, c) W. Radiated power density of b) N, d) W. The corresponding dashed lines represent the coronal values.

The nitrogen density (panel a)) is a factor of two higher than in the reference case, f_{ELM}=143 Hz and approaches a saturated value. The W density is a little over a factor of 2 higher and shows a clear trend to accumulate in the confined plasma region (panel c)). Similarly to the diffusive ELM scenario, the radiated power density of nitrogen (panel b)) is the same as in the reference case f_{ELM}=143 Hz, whereas the W radiation is a factor of 3 higher, panel d). Note that in the diffusive case the increase was a factor of 4. The flush out effect and the outward shift of the ionisation shells characterising the convection behaviour can explain why the increase of P_{rad} in the convective scan is smaller than in the diffusive one.

The comparison between the total radiated power density for the reference case (f_{ELM}=143 Hz) and the $f_{ELM} = 10$ Hz case is illustrated in figure 7.15. The corresponding coronal values are also indicated for completeness, showing no difference between them and non-coronal values for W, while for N the difference is significant. Here, non-coronal effects need to be taken into account. For f_{ELM}=143 Hz, the radiated power at $\rho_{tor} = 0.8$ is about 0.1 MW/m^3 while for the 10 Hz case P_{rad} is 0.30 MW/m^3. For the convective model the W accumulation is significant, but it is a factor of 2 smaller than at the same time point in the diffusive model. Hence, in the convective scenario, W accumulation takes place on a longer time scale.

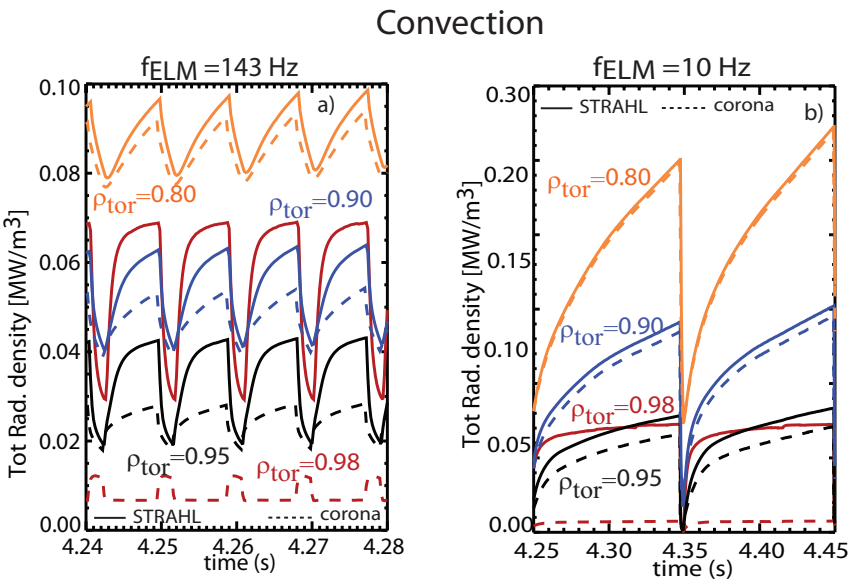

Figure 7.15: Comparison between the total radiated power for the reference case (f_{ELM}= 143 Hz) and the total radiated power with f_{ELM}= 10 Hz.

7.3.3 Comparison with bolometry

It has been shown that the radiated power exhibits opposite behavior depending on the assumed ELM model. In the diffusive case, the ELM crash causes an increase of the pedestal radiation except in the region near the separatrix. In the convective case, it causes a drop at all analysed radial positions. A matter of particular interest is whether the diffusive or the convective ELM model is able to reproduce the measurements of the line integrated radiation. Fast radiation events such as ELMs cannot be resolved by foil bolometry which has a time resolution of 2 ms at AUG. However, the diode bolometer system at AUG offers a high time resolution of down to 50 μs, a wide spectral range and a full coverage of the poloidal cross-section of ASDEX Upgrade [72], making them suitable to study fast events like ELM induced radiation.

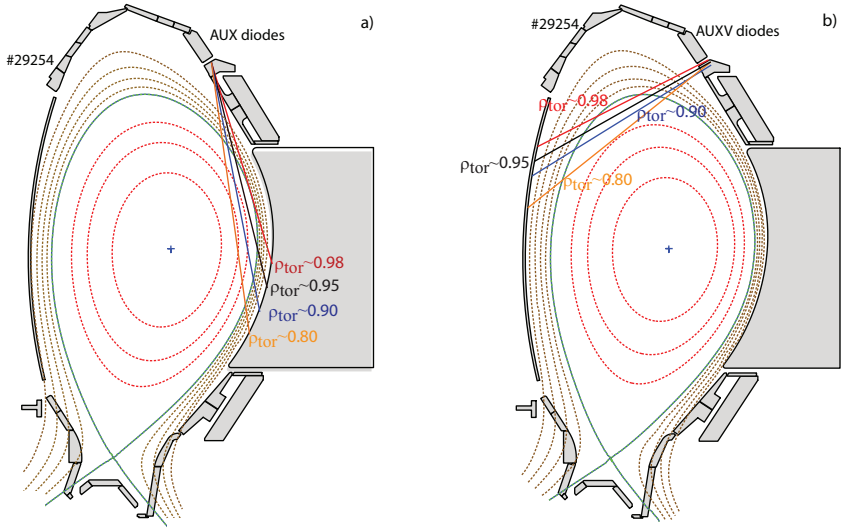

Figure 7.16: a) LOS at the low field side (LFS) chosen for the comparison between diode bolometers and modelling results. The lines were chosen tangential to the radial positions considered in the analysis, b) LOS at the high field side (HFS) tangential to the radial positions considered in the analysis.

In order to validate the predictive capabilities of the simulations and to assess which model is better suited to describe the experimental data, a comparison of the modelled radiated power with the measured P_{rad} has been carried out. From the modelling side, such a comparison can be attained by employing the synthetic bolometry diagnostic which has been implemented in ASTRA. A synthetic diagnostic observes the calculated quantities in the same way as the real diagnostic looks at the plasma. In this way the theoretical predictions can be compared with the measurements. For the synthetic diagnostic, the modelled P_{rad} given by STRAHL has been integrated along the experimental lines of sight (LOS) of the real cameras. The choice of the LOS has been done with care avoiding lines looking into the divertor and choosing lines tangential to the flux surface considered in the analysis. Lines of sight at the low field side have been considered because, compared to the lines at the high field side, they have a longer path in the pedestal plasma and a

shorter path in the SOL which is characterised by high radiation and is not included in the modelling. However, some lines of sight at the high field side have been also investigated and the results will be discussed below. The cross section of AUG with the considered lines of sight at the LFS and at the HFS is shown in figure 7.16 a) and b).

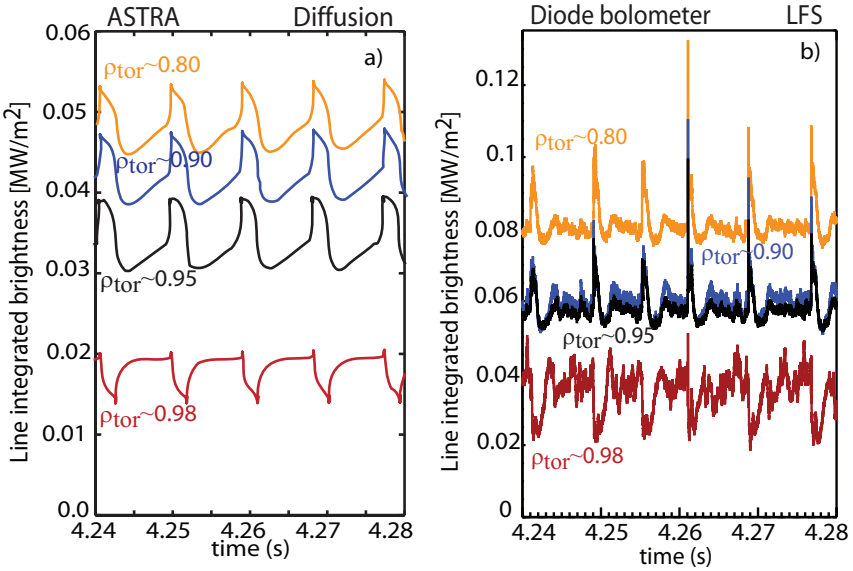

Figure 7.17: Integrated radiation of the same lines of sight at the LFS from the synthetic diagnostic a) and the measurements b). The diffusive ELM model is used. In red at $\rho_{tor} = 0.98$, in black at $\rho_{tor} = 0.95$, in blue at $\rho_{tor} = 0.90$, in orange at $\rho_{tor} = 0.80$.

Figure 7.17 displays the modelled (panel a)) and the measured (panel b)) radiation emitted at the different radial positions considered in the analysis when applying the diffusive ELM model. Both the modelled P_{rad} and the diode bolometers exhibit a radiation peak at the ELM crash, except at $\rho_{tor} = 0.98$ where a drop occurs for both. The comparison indicates that the modelling reproduces the temporal P_{rad} evolution well but the radiation measurements are systematically higher than those of the model. This discrepancy can be explained by considering that the measurements unavoidably take into account also the contribution of radiation in the SOL, which is small at the low field side, but still present. In sight of this fact, the results can be considered to be in reasonable agreement. The situation is different for the lines of sight at the high field side. For these lines the path in the SOL is almost comparable with the path through the plasma (see figure 7.16 for the geometry).

Figure 7.18 shows that the diode signals at $\rho_{tor} = 0.98$ depict small spikes before the drop which are also visible in the model. The modelling reproduces the temporal evolution but the radiation level is significantly higher: ($P_{rad,measured} \sim 3 \cdot P_{rad,modelled}$). In addition, very pronounced peaks are detected at all other radial positions. The pronounced peaks are a consequence of the long path made by the lines of sight in the SOL which is almost comparable with the path through the plasma.

To make this point clear and to demonstrate that these pronounced peaks do not originate

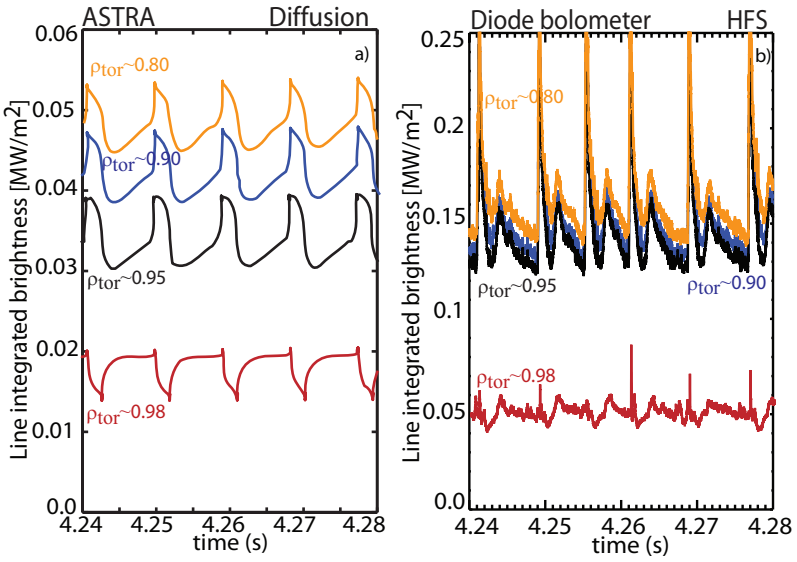

Figure 7.18: Integrated radiation of the same lines of sight at the HFS from the synthetic diagnostic a) and the measurements b). The diffusive ELM model is used.

from the pedestal but are rather a SOL effect, lines of sight in the upper SOL at the high field side have also been evaluated, see figure 7.19 a) for the geometry. The line integrated brightness measured in the pedestal is shown in panel b). Panels c) and d) display the line integrated brightness measured in the upper SOL. The pronounced peaks are also visible in the upper SOL and exhibit the same shape as found in the pedestal. The signals in panel c) are measured just outside the separatrix and exhibit high radiation values as expected when applying N seeding. This is reflected in the signals inside the pedestal. Indeed, this comparison sheds light on the fact that the pronounced peaks present in the HFS measurements originate from the SOL. This motivates the choice to consider the low field side measurements in order to reduce the impact of the SOL on pedestal radiation.

The comparison of the radiated power density using the convective model is presented in figure 7.20. In this case, the modelled P_{rad} (panel a)) drops at the ELM crash at each radial position contrary to the behaviour detected by diode bolometers (panel b)).

To summarise, in this chapter the hypotheses of a diffusive and a convective ELM models were investigated. The best agreement with the experimental measurements is found with the diffusive ELM model, while the convective ELM model clearly does not succeed in describing the experimental data.

The reasons for which in presence of nitrogen the diffusive ELM model describes better the experimental trend of the radiation might be explained with the following arguments: In the general picture, ELMs eject heat and particles into the SOL through filaments which are toroidally non-symmetric plasma structures aligned to the magnetic field. Their structure have been observed in several tokamaks [90, 91]. These filaments have mainly

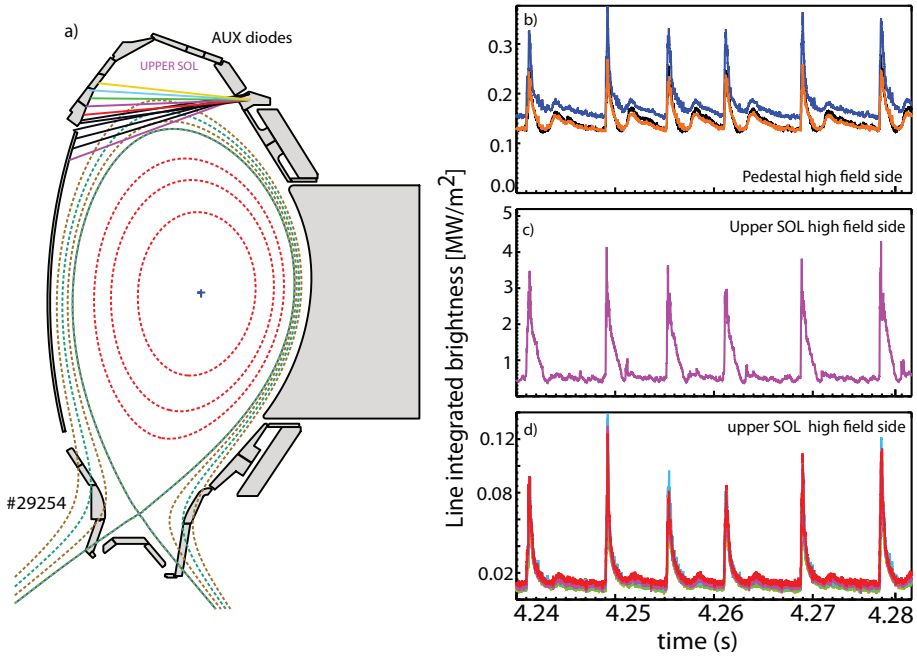

Figure 7.19: a) Geometry of the lines of sight at the upper SOL at the HFS b) Measured pedestal radiation at the HFS c) and d) Measured upper SOL radiation at the HFS.

convective properties [84] and are subjected to radial forces. In AUG they are expelled within 3 ms after the ELM crash but their energy content was found to be insufficient to account for the total expelled pedestal top energy [91]. If the heat and particles expelled by the filaments (convective nature) are low, this implies that the diffusive nature is also playing an important role. In particular, it has been observed that in presence of nitrogen the number of filaments is reduced [79, 92]. This observation is supported also by the modelling which suggests that it is the change in the SOL parameters induced by nitrogen leading to a reduction of the number of filaments [93]. In more detail, short ELMs during nitrogen never have more than one filament and in most cases none filaments at all. The discharge modelled in this chapter has nitrogen and tungsten. In the previous sections it was shown that for W diffusive and convective models predict similar behaviour and from what is reported above the convective nature of the filaments is highly reduced in presence of nitrogen. All this can explain, why for the discharge investigated in this chapter the diffusive ELM model is more suitable than the convective one to describe the experimental observations. A model which combines both the diffusive and convective ELM model could be envisaged. However, since the diffusive ELM model reproduces all the experimental observations, it appears that diffusion dominates the radial ELM transport for the examined cases with N seeding. The combination of the two models is likely to give only a slight modulation to the results obtained in the purely diffusive case. A different ratio of diffusive to convective components in the ELM may be found in cases without N seeding which is responsible for changes in the SOL parameters.

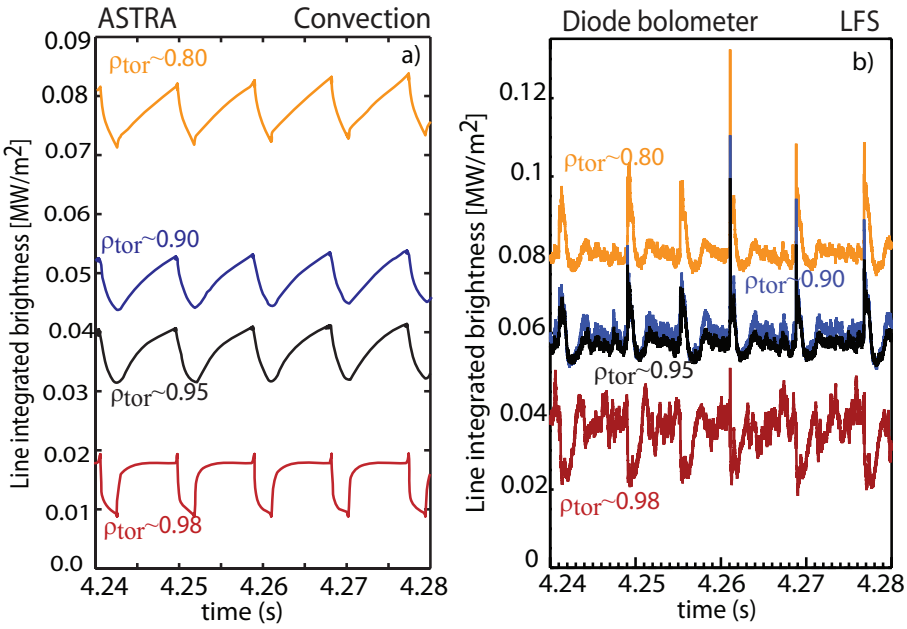

Figure 7.20: a) Integrated radiation of the same lines of sight at the high field side from the synthetic diagnostic a) and the measurements b). The convective ELM model is used.

7.4 Comparison with the PIRT model

As indicated in section 7.1, one of the aims of this work was to investigate the evolution of impurities and radiation in the pedestal in order to answer the following question: Why does the assumption of $f_{ELM} = 1/\tau_{ped}$ assumed in the PIRT model provide a good calculation of the radiated power in non-coronal conditions? The answer requires several considerations: in the peeling-ballooning model for ELMs [94], the ELM is driven by the pressure gradient and the ELM period is determined by the recovery of the profiles until the critical pressure gradient is reached again. This time is governed by both sources and radial transport of particles and energy at the edge of the plasma. It also depends on the heating power since an increase in the heating power results in a faster transport which in turns leads to higher f_{ELM}. Hence, f_{ELM} reflects the impurity residence time through transport effects which determine the recovery of the profiles until the next ELM crash. This is the reason that the inverse of f_{ELM} is a good estimation of the impurity residence time at the pedestal.

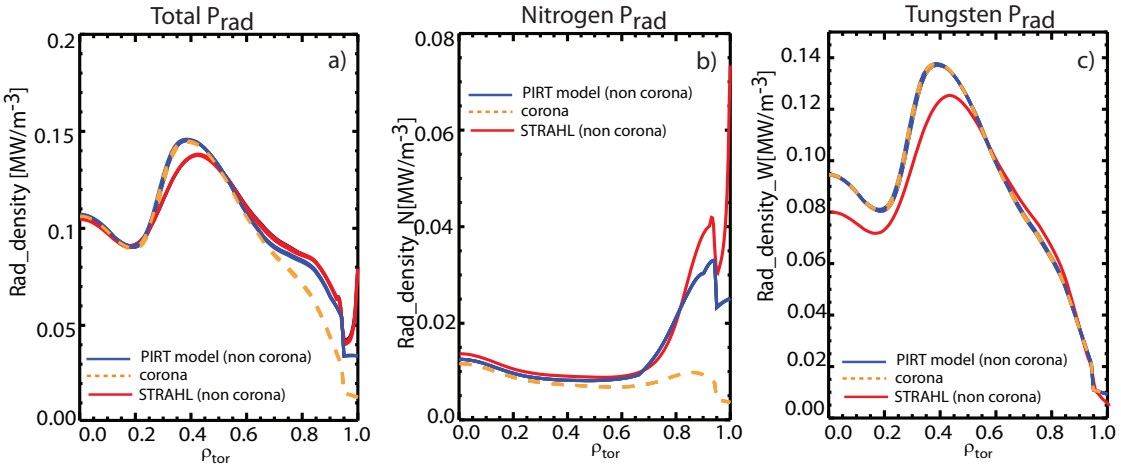

Figure 7.21: a) Total radiated power density profiles: From the PIRT model in blue, from STRAHL in red, from coronal in dashed orange; b) Nitrogen radiated power profile; c) Tungsten radiated power profile.

The very good agreement of the PIRT model with the radiation from STRAHL is shown in figure 7.21. Panel a) compares the total P_{rad} profile obtained from the PIRT model with STRAHL and with coronal calculations. Panel b) shows the comparison between the different models for nitrogen radiation, emphasising again the non-coronal effects at the plasma edge. Panel c) shows the comparison for tungsten. Note that the agreement depends on the plasma radius. At the very edge ($\rho_{tor} > 0.95$) the PIRT model shows constant radiation density with increasing radius which is in agreement with what was discussed in section 6.2. In figure 7.22 a), in addition to the total radiation from PIRT, STRAHL and coronal, the radiation contribution from W and N is also illustrated. Panel a) for the entire radius, panel b) zoomed in the region 0.7< ρ_{tor} <1.0. The important point here is that the radiation in the core is dominated by W while N dominates for $\rho_{tor} > 0.9$. Moreover, these plots indicate that the non-coronal effects already start to play a role at

$\rho_{tor} = 0.7$. As pointed out in section 7.3.1 the $n \cdot \tau$ dependence of L_Z has an important contribution to the radiation and explains why the N radiation does not change with f_{ELM} as significantly as for tungsten.

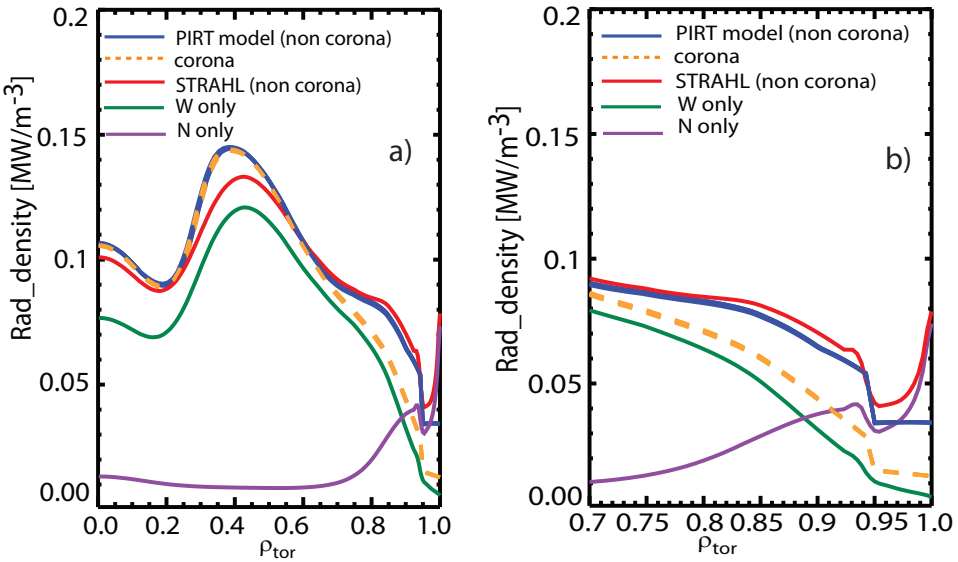

Figure 7.22: a) Total P_{rad} profile from the PIRT model in blue, total P_{rad} from STRAHL in red, total P_{rad} from coronal in dashed orange; W only contribution in green, N only contribution in violet; b) zoomed of the edge region $0.7 < \rho_{tor} < 1.0$.

The question arises what happens when f_{ELM} goes towards zero. At low f_{ELM} severe W accumulation occurs in the experiment as well as in the modelling. The STRAHL calculations showed that with f_{ELM}=10 Hz, W accumulates in the confined region and the simulation crashes. This is an indication about the excellent predictive capability of the simulations: they are able to reproduce the experimental behaviour in detail and therefore they encounter the same limitation of W accumulation as the experiments. Scenarios which foresee a mitigation or suppression of the ELM activity could also be considered: stationary cases with mitigated ELMs by B-coils [95] or quiescent H-modes, i.e H-modes without ELM activity [96]. In this cases a modification of the transport Ansatz would be required to account for their different transport properties compared to the analysed cases.

7.5 Summary and discussion

Time dependent modelling of kinetic profiles, impurities and plasma radiation in presence of ELMs has been presented for an AUG discharge. The simultaneous evolution of nitrogen and tungsten has been simulated for the first time. One of the important achievements of this modelling effort is the capability to reproduce the experimental discharge behaviour feeding the simulations only with transport coefficients and heat and particle

sources. A supplementary finding is the ability to predict W accumulation at low ELM frequencies starting from a transport Ansatz. Such achievements open a path towards a predictive use of the model which can allow the extrapolation of the impurity and radiation behaviour to other devices and to other impurity species. The modelling highlights the importance of high ELM frequency for the pedestal screening of the neoclassical inward pinch. It shows that an $f_{ELM} > 10$ Hz is required to prevent collapse by radiation due to W accumulation. This is in agreement with the results reported in Ref. [97] where an experimental minimum f_{ELM} of 12 Hz was found necessary to avoid W accumulation in AUG.

The results emphasise that while W radiation is to a large extent determined by f_{ELM} ($P_{\mathrm{rad,10Hz}} \sim 4 \cdot P_{\mathrm{rad,143Hz}}$), the N radiation is less affected. A possible explanation for this behaviour was given in section 7.3.2 and takes into account the dependence of the nitrogen L_Z on T_e and the observed temperature pedestal increase due to nitrogen. The strong enhancement of nitrogen radiation caused by the non-coronal effects through the ELM-induced transport is well reproduced and is in the range: $\frac{P_{\mathrm{rad,nocoronal}}}{P_{\mathrm{rad,coronal}}} \sim (2-5)$.

The different behaviour of N and W suggests a charge dependence of the impurity transport. In fact, the ETB is dominated by collisional radial transport which is characterised by a strong inward pinch that increase with impurity charge. This determines the strong peaking of the W profile causing W accumulation in the confined region. The effectiveness of ELMs to flush out tungsten from the confined region depends on the nature of particle transport during the ELM crash, namely if the ELM transport is diffusive or convective. Both hypotheses of a diffusive and a convective ELM transport were investigated. Both models show that low ELM frequencies lead to W accumulation, whereas convection appears favourable over diffusion in terms of impurity accumulation. The different effects of diffusion and convection on the ionisation stages of nitrogen were also shown: broadening and inward shift in the diffusive case, narrowing and outward shift in the convective case. In the convective scenario, this implies that the radiation is localised at the very edge with less radiation localised at the pedestal top.

A matter of particular interest is, whether the ELM behavior is of diffusive or convective nature. The comparison with diode bolometry reveals that the temporal evolution of the radiation is well reproduced by the diffusive ELM model, while the convective ELM does not succeed in describing the data. In section 7.3.3 a possible explanation for that has been attempted which considers the filamentary nature of the ELMs and the fact that in presence of nitrogen the number of filaments is reduced or even equal to zero. This means that convection is reduced such that diffusion dominates. Beside the considerations above, the results of this chapter are also in line and complementary to earlier studies dedicated to the measurement of the impurity transport coefficients [98]. Such studies have shown that an edge transport model with a diffusive transport during ELMs and an inward pinch in the inter-ELM phase yields the best description of the measurements.

For the future, it would be interesting to investigate these hypotheses from an experimental point of view as well. For instance, one could study the temporal profile evolution of nitrogen during an ELM while changing the ELM frequency.

Chapter 8

High density experiments with pellets

Future devices will have to operate at high core density to maximize fusion power. However, high edge temperatures and densities will strongly reduce the penetration of neutrals coming from gas puffing and therefore the particle source. The repeated injection of frozen deuterium pellets is a well established and powerful technique for high density operation which will be mandatory in ITER and DEMO to reach the operational densities. The upgraded pellet launcher system at ASDEX Upgrade with a versatile set of diagnostics is well suited for such studies. Section 8.1 introduces the high density scenarios obtained with pellet injection. Profile, transport and confinement analysis for an example discharge are discussed in section 8.2, 8.2.1 and 8.2.2.

8.1 Experiment set up

The high speed inboard pellet injection system at ASDEX Upgrade [99] consists of a storage cryostat type pellet source, a centrifuge accelerator and a guiding tube system (figure 8.1 left). The system delivers pellets with different sizes, speeds and repetition rates up to 70 Hz on a shot to shot basis. Pellets are launched into the plasma from the centrifuge launcher through a 17 m curved guiding tube. They are injected from the magnetic high field side (HFS) at an angle of 72 degrees to the mid plane. The HFS injection, although technically more complicated, allows to exploit the ∇B drift which in this case accelerates particles towards the plasma core [100].

An example where the full fuelling capability of the new pellet system has been exploited is shown in figure 8.1 Right). The plasma parameters were set to I_p = 1.0 MA, B_t = -2.5 T with a total heating power of 12 MW (panel a)). Besides the NBI, central heating is important to avoid impurity accumulation. However, for machine protection, during

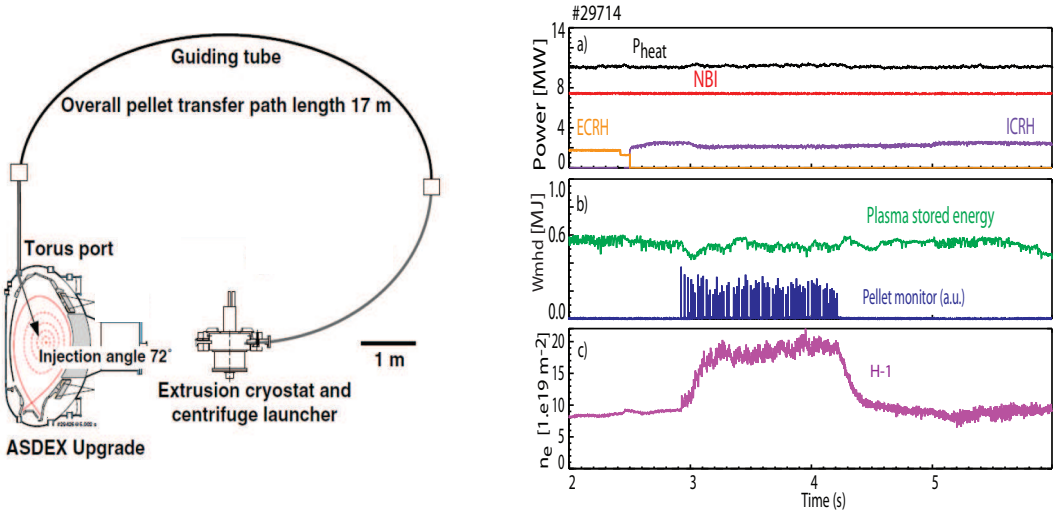

Figure 8.1: Left: The pellet launching system setup at AUG as operated in the campaigns 2012-2014 [101]. Right: Time traces of a typical high density discharge with pellets: a) P_{heat} (black), NBI, ECRH, ICRH heating (red, orange, violet); b) W_{mhd} (green) and pellet monitor (blue); c) density (H-1 channel).

the pellet train ECRH cannot be used because of strong power reflections at high density cut off layers. For the same reason, the ECE diagnostic is also not in operation. Hence, during the pellet train and also after this phase, core heating is provided solely by ICRH. At constant heating power a total number of 73 pellets of the largest available size were injected into the plasma at the maximum rate of 70 Hz with a speed of 572 m/s. The chosen velocity is the result of a balance between the maximum pellet penetration and pellet mass reduction [101]. The entire ice reservoir was consumed in one go enabling a pellet train of about 1.3 s from t= 2.9 s to 4.2 s (panel b)). During the pellet phase a high core density is reached and kept until the very last pellet (panel c)). When the last pellet is consumed all plasma parameters return to their initial values and the discharge can be ramped down safely. Except for a transient decrease at the very first pellets, the plasma stored energy stays constant during the discharge (panel b)). Its value is only around 0.6 MJ due to the moderate heating power. The transient behaviour at the start of the pellet train is analysed in detail in the following section 8.2.

8.2 Temperature and density studies

In order to gain a better understanding of the transient phase occurring at the start of the pellet train, time traces and profiles of both electron temperature and density of the presented discharge #29714 are analysed (figure 8.2).

The stored energy drop (panel c)) is caused by the faster temperature response compared to the density response, as indicated in panel a), b), d) and e). The first pellets induce

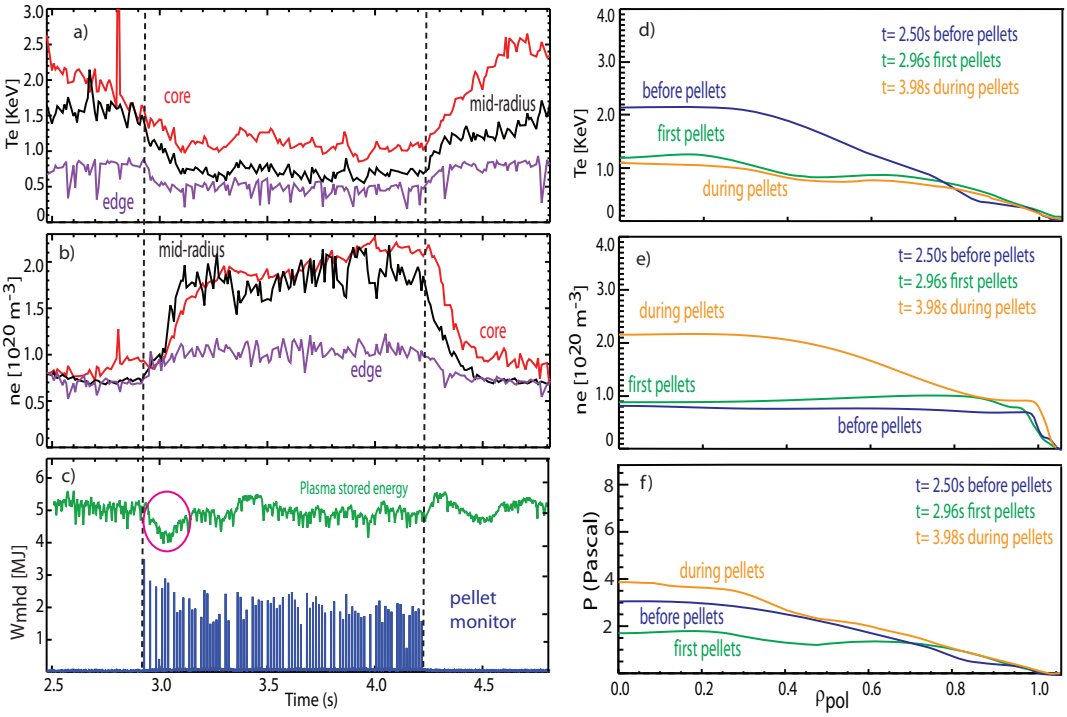

Figure 8.2: Time traces of a) T_e, b) n_e. In red in the plasma core, in black at mid-radius, in violet at the plasma edge. c) Stored energy and pellet monitor. d) T_e profile , e) n_e profile, f) pressure profile. In blue before the pellets, in green at the first pellets (at the minimum of W_{mhd}), in orange during the pellet train.

a drop of the pedestal temperature which propagates quickly towards the centre through profile stiffness. The pellets cool the plasma significantly such that the electron temperature is reduced by about 50 %. It should be underlined that due to this drop in T_e caused by the first pellets, the penetration depth of the following pellets into the plasma is increased. This favours the particle fuelling. The experimental temporal behaviour of the temperatures over the discharge is well reproduced by the critical gradient model presented in section 2.5 indicating the importance of the profile stiffness in determining the global plasma performance.

The density increase starts at the edge, while the increase in the core is slower. This is due to the low particle diffusion and due to the fact that an increase in density requires a given amount of particles which can only be delivered by the pellets on a longer time scale. This behaviour is well visible in panel b) (t= 2.9-3.2 s): the density at mid-radius (black) increases quickly while the core (in red) follows more slowly. As a result the profile is hollow in the center (panel e), green)). The pressure is similar before the pellets and after the transient phase when the density has reached its steady-state value (panel f)). This is consistent with the constant plasma energy. The recovery of the stored energy follows the density build up. After about 100 ms the core density also starts to rise and steadily increases until it reaches values of $2.3{\cdot}10^{20}$ m^{-3} (panel b)). In this time range the effect of diffusion become effective and the profiles in the centre are not hollow any longer (panel e) in orange). Towards the end of the pellet train (t= 4.0-4.2 s) the core density (in

red) keeps increasing while the density at mid-radius appears to stay constant (panel b) in black. The effect might be attributed to the Ware pinch (section 2.4) which plays an important role at high collisionality [102]. Interestingly, at mid-radius the density starts its decay right after the last pellet (due to the absence of the particle source), while the density in the core stays high for other $\sim$ 600 ms. This behaviour, where two different time scales seem to be involved was also found in the other analysed discharges (for instance the discharge presented in appendix A) and provides an important input for a particle transport analysis which is outside the scope of this work. The change in the density gradient indicates that the particle deposition is located around $\rho_{pol} = 0.6$. Note that in ITER this is estimated to be around $\rho_{pol} = 0.8$ which raises concerns about the effectiveness of pellet fuelling to reach sufficient core densities. This point is discussed in section 8.2.2.

To summarise, after the injection of pellets several processes occur in the plasma on different time scales: while the response of T_e is fast, the density builds up on a longer time scale. One possible reason for the faster response of T_e at the edge involves convective losses. Thereby plasma energy is spent on heating and ionising the ablation cloud of the pellet. The convective process is faster than both pellet delivery or particle diffusion, both processes on which the density build up depends on. This gives rise to a transient phase with reduced plasma energy right at the beginning of the pellet train. The described phenomena are fast, whereas diffusion and relaxation of the profile after the injection take place on a time scale of the order of the confinement time.

8.2.1 Transport analysis

The relation between pellet penetration and confinement is a crucial question and requires the understanding of plasma transport under such conditions. In the following the transport analysis for discharge #29714 is presented.

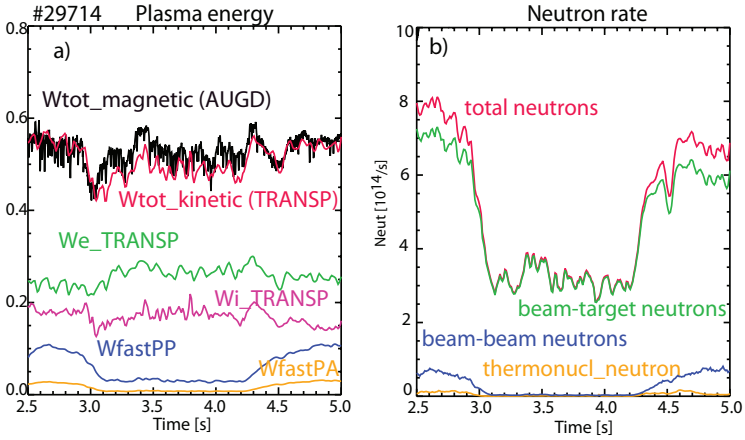

Figure 8.3: a) Contributions to the total stored energy W_{tot} from kinetic data (red): W_e (green), W_i (magenta), energy from fast perpendicular ions W_{fastPP} (blue), energy from fast parallel ions W_{fastPA} (yellow). W_{tot} from magnetic data (blue) agrees with TRANSP calculations. b) Total neutron rate from TRANSP (red) with its contributions: beam-target neutrons (green), beam-beam neutrons (blue), thermonuclear neutrons (yellow).

Similar to the analysis procedure adopted for the high radiation scenario (section 6.4), first the consistency between magnetic and kinetic data is verified. Also in this case, an excellent agreement between the magnetic plasma stored energy W_{tot} and the kinetic reconstruction from TRANSP is found. Both reveal that the stored energy remains constant throughout the discharge despite the strong density increase (excluding the transient phase at the beginning of the pellet train discussed in section 8.2). Figure 8.3 a) displays the stored energy components from TRANSP calculation. The main contributions are the thermal components W_e and W_i. Additional contributions consist of a perpendicular and a smaller parallel fast ion component. Note the decrease of the fast ions due to the increased collisionality (figure 8.4 c)). Panel b) shows the contributions to the neutron rate calculated from TRANSP. Three different contributions can be distinguished: the beam-target neutrons, the beam-beam neutrons and thermonuclear neutrons. Plot b) indicates that in AUG the main contribution comes from the beam-target where the beam is provided by the NBI. This is in agreement with Ref. [81], in which this contribution is identified as the dominant one in NBI heated discharges for P_{NBI}> 5 MW. The significant decrease of the neutron rate during pellets can be understood in terms of the smaller fast ion contribution due to the lower temperature and higher collisionality, the latter increasing by one order of magnitude during the pellet phase (figure 8.4 b)).

Results of the transport analysis are shown in figure 8.4 in black for the reference phase, in

red during pellets and in green for the post-pellet phase. Panel a) displays the NBI power deposition. It shows off-axis power deposition during the pellet train due to the high density and the consequently reduced beam penetration depth. Moreover, the TRANSP calculations indicate that during the pellet train the power deposited to the ions is lower than the power deposited to the electrons, in contrast to what happens in the pre and post pellet phase. The reason is that the fraction of heat going to electrons and ions is dependent on the beam energy and the plasma temperature. This relation is expressed by the parameter E_{crit} which is proportional to T_e [103]. In the case of low T_e (pellet phase), the heat is deposited more to the electrons.

Changes in temperature and density affect the collisionality which is directly proportional to the density and inversely proportional to the temperature. Panel b) illustrates, as expected, that collisionality increases significantly during the pellet phase by about one order of magnitude. As the other parameters, it returns to its initial values in the post-pellet phase.

Panel c) displays the effective heat diffusion coefficients for the three different phases. In this case of high collisionality, it is not possible to separate the electron and ion channels and an effective diffusivity has to be used 2.2. The power balance shows that χ_{eff} during the pellet train agrees well with its value before pellets inside the error bars for $\rho_{tor} > 0.5$. For $0.3 < \rho_{tor} < 0.5$, χ_{eff} exhibits an hump (in red) probably related to the off-axis deposition of the NBI to the electrons (panel a)). In the post-pellet phase χ_{eff} returns to similar values as in the initial phase. Panel d) shows that during pellets R/L_{T_e} and R/L_{T_i} change dramatically. This is attributed to the steep gradient modification and to the off-axis deposition. In the post pellet phase R/L_{T_e} and R/L_{T_i} return roughly to their initial values.

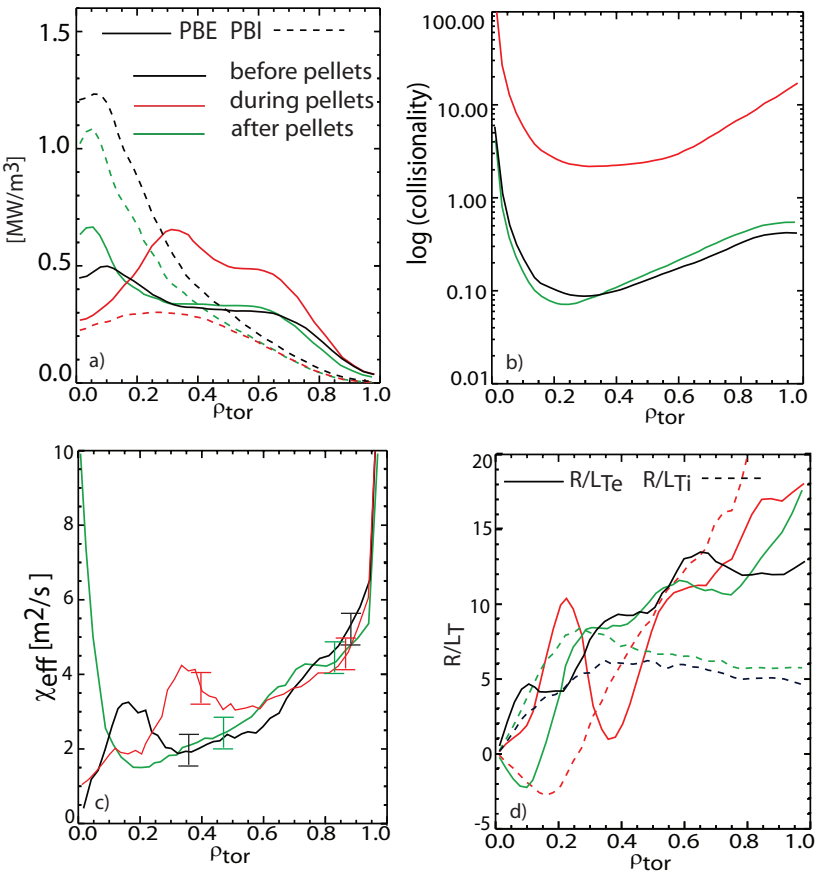

Figure 8.4: a) NBI deposition, b) collisionality (log scale), c) χ_{eff}, d) R/L_{T_e} and R/L_{T_i}. In black for the pre-pellet phase, in red during pellets and in green for the post-pellet phase.

8.2.2 Confinement analysis

Calculations of τ_E from both kinetic (TRANSP) and magnetic data (AUG) reveal that the confinement time remains constant during pellets despite the density increase (figure 8.5 red and black). In contrast to this, the IPB98 scaling (section 2.1) predicts a strong overestimation of τ_E during the pellet phase due to its proportionality $\tau_E \sim n_e^{0.41}$. A scaling describing the roll-over of τ_E with respect to $\frac{n}{n_{Gw}}$ has been proposed in Ref. [104]. This so-called H06 scaling improves the empirical ELMy H-mode confinement scaling from 1998 based on a standard dataset provided by a number of conventional and by two spherical tokamaks. The scaling reads:

$$\tau_{E,H06} = 6.94 \cdot 10^{-7} \cdot M_{eff}^{0.2} \cdot \kappa_a^{0.37} \cdot \left(\frac{q_{95}}{q_{cycl}}\right)^{0.77} \cdot A^{2.48205} \\ \frac{I_p^{1.3678} \cdot B_t^{0.12} \cdot R_0^{1.2345} \cdot n_e^{0.032236}}{A^{0.9 lnA} \cdot P_{net}^{0.74}} \cdot \left(\frac{\bar{n}_e}{n_{Gw}}\right)^{-0.22 ln \frac{\bar{n}_e}{n_{Gw}}} \tag{8.1}$$

M_{eff} is the effective atomic mass of the ions and allows the disentanglement of the interaction effect of the isotopic species. $\kappa_a = \frac{V}{2\pi^2 R a^2}$; $A = \frac{R}{a}$ is the aspect ratio. The dependence on the plasma shape is included by $f = \frac{q_{95}}{q_{cycl}}$. The density dependence is such that the exponent changes sign for densities $> n_{Gw}$.

The main difference between the two scaling is that in 1998, when the IPB98 was put forward, no data at high densities were available, whereas in 2006, when the H06 scaling was proposed, high density data were available. Therefore the data were fitted by a parabola which describes exactly the saturation of τ_E with increasing density for values $n_e > 0.85 \cdot n_{GW}$. This deviation above $0.85 \cdot n_{GW}$ is of particular importance since the calculation to achieve the maximum Q value (fusion power divided by external heating) for ITER were done assuming a confinement time of 4 s at n_{GW}= 0.85. Additionally, it had been already observed that the H-factor was decreasing slowly with the density for low triangularity but faster at high triangularity showing the importance of this parameter [105, 106]. However, the inclusion of the triangularity from all the different machines is not an easy task. In the H06 scaling this was accomplished using $f = \frac{q_{95}}{q_{cycl}}$ which has also the advantage of taking the magnetic shear and the current at the pedestal into account [107]. Note that the triangularity is important also for the high radiation scenarios. For instance, in section 6.5, it was shown that confinement improves with plasma shape.

The confinement time for discharge #29714 calculated from kinetic data (red), from magnetic data (black) and both predictions from the IPB98 (violet) and the H06 scaling (green) are displayed in figure 8.5. The time trace of the H-1 density channel is also shown to relate the τ_E changes to density changes. The comparison shows that the IPB98 is not suitable to describe τ_E in the high density regime, whereas the H06 turns out to be more appropriate.

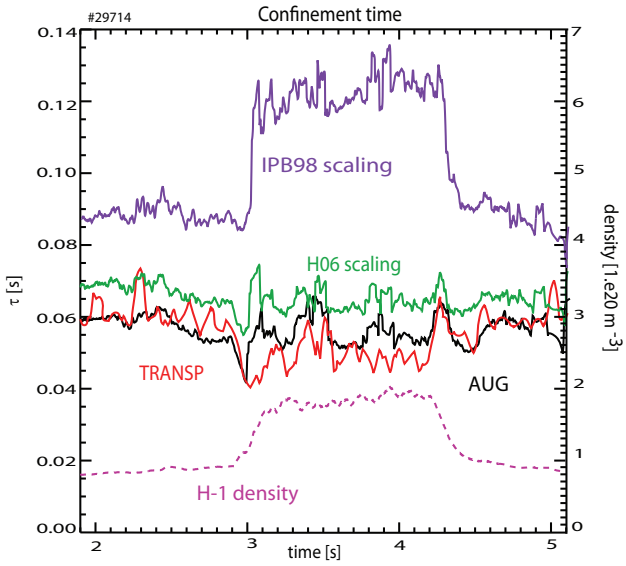

Figure 8.5: Comparison between τ_E from TRANSP (red), τ_E from AUG (black), τ_E from IPB98 (violet) and τ_E from H06 scaling (green). The density increase in the H-1 channel is also shown (dashed magenta).

Beside the importance of validating a scaling in a new scenario, it is crucial to understand the observed behaviour of τ_E in this high density regime. One observation is related to the pedestal pressure. For a given pressure, when the density profiles are flat, operation at low density is favorable. This allows higher pedestal temperatures which are then transferred to the core via stiffness. Conversely, operation at high density implies that the temperature is necessarily lower. In that case, the pressure is dominated by the density which, unlike the temperature, does not have a stiff profile. The change of pressure profile is an important question also in the case of peaked density profiles as presented here. In this case the key question is if the peaking of the density profile leads to a flattening of the temperature profiles. Indeed, the results of this thesis show that the temperatures remain stiff which is beneficial for an increased fusion output.

Another consideration is that the higher the density is, the more the NBI heats the plasma off-axis due to a reduced beam penetration. This condition is not favourable to increase the plasma temperature and therefore the confinement. In ITER this effect might only play a minor role due to the central α particle heating. In a reactor the power will be not an external adjustable input parameter as in present devices, but it will be an intrinsic plasma parameter. A third consideration is related to machine size. On one hand one has to consider that a reactor will be a much larger machine, with a larger B_t and I_p leading to a better confinement. On the other hand, because of the bigger dimensions, it is estimated that pellets will penetrate only up to around $\rho_{pol} \sim 0.8$. Hence, the important question is whether such an off-axis pellet deposition can still lead to high central density in order to reach sufficient fusion power. Central high densities can be achieved only with a peaked profile such that the edge density stays below the Greenwald limit. For low collisionality, which are a characteristic of a future reactor, such peaking could be generated by the turbulent particle pinch [14]. Indeed, peaked profiles at zero loop voltage

were observed [108] which exclude the occurrence of the Ware pinch and give indication of a non neoclassical pinch component.

The results presented in this chapter can contribute to an improvement of the scaling law for τ_E, contributing to the understanding of the underlying physics in high density scenarios. The H06 scaling describes the presented high density experiments at AUG, while the IPB98 does not. Possible improvements to the scalings must be based on a better understanding of the physics and an extended experimental database for $n > 0.85\, n_{GW}$. The discharges carried out during the course of this thesis were performed at constant heating power. The results presented here suggest that performing experiments exhibiting steadily increased central power would clarify the extent to which increasing heating power raises core temperature.

Chapter 9

Summary, conclusion and outlook

This work is dedicated to the study of high radiation and high density tokamak scenarios which are essential for future reactor operation. The high radiation fraction is required to limit power loads on machine components, whereas the high density is needed to maximise fusion performance.

The impurity seeding technique is typically employed in order to reduce heat loads to tolerable levels, whilst maintaining acceptable confinement. This thesis investigates the effect of impurities on plasma confinement properties through experimental and modelling means. In the experiments carried out over the course of this work the impurity seeding was applied to H-modes by means of nitrogen seeding, but also by injection of medium-Z impurities in order to radiate in the main chamber and assesses the possible impact of central radiation on confinement. Additionally, since future reactors will contain helium ash, the impact of helium on transport and confinement was also investigated.

High radiation experiments

Since edge radiation for low-Z impurities is subject to non-coronal effects, a non-coronal radiation model (PIRT) was developed and compared to bolometric measurements in order to provide a reliable radiation profile for transport calculations. Considering that ELMs flush out impurities and lead to a reorganisation of plasma profiles at each crash, the PIRT model uses the inverse of the ELM frequency as the residence time of impurities at the pedestal. The validity of this assumption was verified by modelling the evolution of the impurities and radiation with ASTRA coupled to STRAHL.

Transport analyses taking into account the spatial radiation distribution were performed for nitrogen seeded discharges and for discharges where N was combined with Kr and He. These confinement studies provide the following results:

N concentrations induce higher pedestal temperatures whilst keeping the density unchanged and therefore leading to higher pedestal pressure. Understanding the increase in the pedestal temperature and the link to pedestal stability is currently a major challenge in this field. A further confinement improvement can be obtained by increasing the triangularity. Likely this reduces f_{ELM} leading to a density increase.

The transport analyses conducted here indicate a strong role of the profile stiffness in setting the temperature profile features, as the pedestal improvement obtained with N is propagated to the core via stiffness. Hence, also with impurity seeding the edge temperature is an essential parameter of the profile behaviour and consequently for the global confinement.

The ELM frequency is key in controlling impurity concentrations in the plasma. In the N+Kr phases analysed here f_{ELM} is reduced due to the Kr radiation inside the pedestal which reduces the heat power flux through the separatrix. With a lower f_{ELM} the N concentration in the plasma increases. This is interpreted here as a result of the weaker impurity flush out due to a lower f_{ELM}. The higher N concentration in the plasma leads to further confinement improvement than obtained with only N as long as the Kr concentration is kept low enough such that f_{ELM} remains high enough to avoid impurity accumulation in the confined region. The avoidance of a radiation collapse due to excessive impurity accumulation requires accurate control of the Kr concentration in the plasma. This thesis provides an estimate of the Kr concentration simulating its source in STRAHL and comparing it with bolometry measurements. This method offers an estimation of the amount of Kr above which the discharges terminate in a radiation collapse. However it would be desirable in the future to have spectroscopic measurements of this impurity. It would be also useful to identify the impact of Kr on confinement and on the critical f_{ELM} without N. A modelling approach could be applied to estimate the critical f_{ELM} below which Kr accumulates, as was performed for W in the modelling section of this work.

Discharges with N+He are characterised by higher f_{ELM}. Here the increase of f_{ELM} induced by the presence of He leads to a reduction of the N concentration in the plasma reducing its beneficial effect and thus reducing the plasma performance. The analysis reveals that the width of the ion temperature profile is larger in the N-only phase than in the N+He phase. However, the ion core temperature in the N+He phase returns to the reference values suggesting also a contribution to degradation coming from the confined region. A slight increase in the ion heat diffusivity is found which is however not sufficient to account for the observed degradation. Since the case analysed here are complicated by the presence of nitrogen, experiments with He only are recommended to identify the extent of the He impact on energy fusion performance.

In light of the aforementioned findings, edge localised radiation losses do not impact the global confinement as along as the H-mode pedestal is sustained, whereas central radiation must be taken into account and kept at a level which is significantly lower than the local heating power density. Even using high-Z radiators, if the core radiation losses are controlled and the ELM frequency is kept high enough to avoid the radiation collapse, an even higher confinement than the one obtained with N-only can be achieved. The con-

finement improvement when using both low and high-Z radiators might be explained by an increased nitrogen concentration raising the plasma stored energy by increasing the temperature at the pedestal. However, since impurities contribute to Z_{eff}, this might indicate that the higher Z_{eff} (independent of the chosen impurity) can also contribute to the confinement improvement. The effect of Z_{eff} on the pedestal stability is currently under investigation [80]. However, the key role of the critical gradient behaviour for the regulation of the profile characteristics suggests that, in addition to a pedestal improvement, optimisation of fusion performance could originate from acting on the profile stiffness. This could be achieved for instance through q-profile shaping as currently investigated in so-called "improved H-modes" or hybrid scenarios.

The analysis of the collected database based on 79 seeded H-mode discharges with different radiators, radiation levels and heating powers shows that a wide range of plasma parameters was achieved. In particular ITER relevant values for the radiation fraction and the Greenwald fraction have been achieved keeping H_{98} close to 1. This is of particular importance because the working points of ITER and DEMO lie outside the currently used IPB98 database (on which the scaling is based) for at least these two quantities: radiation fraction and Greenwald fraction. This work contributes to collect data points in these regions, which are presently sparsely populated, and to the understanding of the underlying physics.

High radiation modelling

In order to gain a better understanding of the complex physical mechanisms which govern the behaviour of radiation and impurities in the presence of ELMs, an extensive modelling of the analysed N-seeded discharges was performed. This has been achieved by coupling the ASTRA and STRAHL codes. These time-dependent simulations include the self-consistent interplay of heat and particle transport of the background plasma and of impurities, radiation and transport effects induced at the edge by ELMs. The simultaneous evolution of nitrogen and tungsten was simulated for the first time. The experimental discharge behaviour was reproduced providing only transport coefficients and heat and particle sources. ELMs are modelled based on the two different assumptions of a diffusive and a convective transport individually. W accumulation at low ELM frequencies was successfully predicted by both ELMs models. Since the modelling was validated against experimental data from AUG, a predictive use of the model can be envisaged to determine the impurity and radiation behaviour of other impurities species and of other devices.

The model underlines the importance of high ELM frequency for the pedestal screening of the neoclassical inward pinch through exhibiting a radiation collapse when $f_{ELM} \leq 10$ Hz. This value is comparable to Ref. [97] where W was found to accumulate in AUG when f_{ELM} was below 12 Hz. Furthermore, the model demonstrates that W radiation is highly dependent on f_{ELM} while N exhibits only a weak f_{ELM} dependence. A possible explanation was offered whereby the role of L_z and its dependence on T_e is the reason for the difference in f_{ELM} dependence. It has also been found that ELM induced transport is

the main factor determining the N radiation characteristics. Increases in N radiation due to non-coronal effects are reproduced accurately illustrating the prominence of non-coronal effects in N radiation. These effects are not important for highly charged impurities such as W because of their higher ionisation and recombination rates leading to a faster equilibration. A comparison between the modelling results and the non-coronal PIRT model shows that the assumption $\tau_{ped} = 1/f_{ELM}$ is a good approximation for the residence time at the pedestal because f_{ELM} reflects the impurity residence time through the transport effects which determine the recovery of the profiles till the next ELM crash. It is crucial to take non-coronal effects into account in order to correctly estimate the radiation at the plasma edge.

The peaked nature of the W profile, responsible for its accumulation in the confined region, is determined by the strong inward pinch which is due to the dominance of collisional radial transport and the high Z. The degree to which W is flushed out depends on whether the ELM transport has a diffusive or a convective character. Both models exhibit W accumulation at low f_{ELM}, however this effect is lower in the convective model. The diffusive case predicts a broadening and inward shift of the N ionisation stages whilst the convective model shows a narrowing and outward shift. The latter is consistent with less localised radiation at the pedestal top and more at the very edge.

From comparison with diode bolometry it appears that only the diffusive ELM model describes the experimental data for the cases analysed here (with N). This could be due to a reduction in the number of filaments in the presence of N which would reduce convection. In absence of N seeding the convection may instead play an important role. Investigating which ELM model is more suitable in presence of impurities other than N could be an interesting topic of future work. From the experimental point of view, the temporal profile evolution of the considered impurity could be studied while f_{ELM} is varied.

High density experiments

Operation at high density can be achieved either with strong gas puff which leads to a reduction of the confinement, or by injection of frozen deuterium pellets such that central high densities are reached keeping the edge density below the Greenwald limit. The analysis of the high density experimental data conducted in this thesis has shed light on three main issues pertaining to this scenario:

Multiple independent processes take place when pellets are injected into the plasma, in particular a transient drop of the plasma energy at the beginning of the pellet train is observed. The plasma energy is spent on heating and ionising the pellet cloud. Hence, the drop in T_e is faster than the density build up. As the density is increased, the plasma stored energy recovers. This process can explain the observed loss in plasma energy.

During the pellet train the collisionality increases and the NBI deposition becomes off-axis during the high density due to the weaker beam penetration. This leads to dramatic

change in R/L_{T_e} and R/L_{T_i}. The transport analysis shows that the temperature profiles are also stiff under such conditions. Hence, stiffness appears to be a very general property of the plasma, not only does it characterise the profiles in L-mode and H-mode, but also in presence of N, Kr, Ar, He and pellets. This is beneficial in order to obtain an increased fusion output. The question of whether such an off-axis pellet deposition can still lead to high central densities in order to reach sufficient fusion power is naturally of major interest. For low collisionality, which is a naturally characteristic of future reactors, such peaking could be generated by the turbulent particle pinch. The extent to which the heating power could raise the central temperature may be identified performing experiments varying the heating power.

A detailed correction of fringe jumps in the DCN data allowed the reconstruction of the density profiles immediately after the injection of the last pellets. Two different time scales were identified in this decay phase which are promising starting point for particle transport studies in transient phases.

Concerning predictions for future devices, the energy confinement time remains constant at high densities. Hence, the confinement improvement $\sim n^{0.41}$ predicted by the IPB98 scaling is not observed. A scaling which foresees the roll over with respect to the Greenwald fraction turned out to be more appropriate. The results presented in this thesis can contribute to the understanding of the underlying physics in high density scenarios.

This work has fulfilled the goal of providing a coherent understanding of some aspects of the high radiation and high density scenarios. These studies, contributing to the understanding of the effects of impurities and pellet injection on confinement, provides a basis for comparison with studies of these effects in other devices. An extension of the confinement scaling is currently undertaken by the multiple-machine database group. The recent results of this thesis will contribute to this activity.

Appendix A

Development of an algorithm for fringe jump corrections

In chapter 8 it was shown that pellet injection is a powerful tool to reach high densities. However, the strong transient local perturbations caused by pellets impact several diagnostics at AUG, in particular the DCN interferometer measurements which provide indispensable information on n_e. In this section the algorithm developed in this work for fringe jump corrections is presented. As discussed in section 5.3.1, the DCN interferometer measures the phase shift between the reference and detector signals providing a line integrated measurement of n_e. Up to now, the phase shift and the counting of the integer multiple of 2π have been achieved with two generations of hard-wired readout electronics [60, 109]. Both sets of readout electronics band-pass filter the raw signals before further processing them. In the presence of pellets, the two available sets of DCN readout electronics behave differently: the old one drifts away towards negative density as a result of not detecting the pellet-related density rise. Whereas the new electronic detects a constant density increase as a result of massively overestimating the density rise by pellets (figure A.1 a)). These observations motivated the development of a detection approach based on the acquisition of raw data and phase reconstruction by software. Hence, raw signals for all 5 DCN channels for a few pellet discharges have been digitised with a sampling rate of 1 million samples per second. The analysis of the raw signals shows that the injection of fast and large pellets causes a sudden local density rise (due to the gas sublimating from the pellet surface) and a drop of the signal amplitude which slowly recovers (figure A.1 b). This effect is more enhanced for the edge channels. The phase is determined by the zero crossing of the signal. If a pellet arrives in the plasma, the signal does not cross the zero line for several oscillations (A.1 b)). This explains the behaviour of both the hard-wired phase detectors which use zero-crossing detection. All oscillations taking place above the zero line are cut off so that useful information is lost. Depending on phase counter design, the temporary lack of zero-crossings is either interpreted as strong density rise or as signal

perturbation, in whose presence constant density is assumed by default. This leads to the observed density time traces.

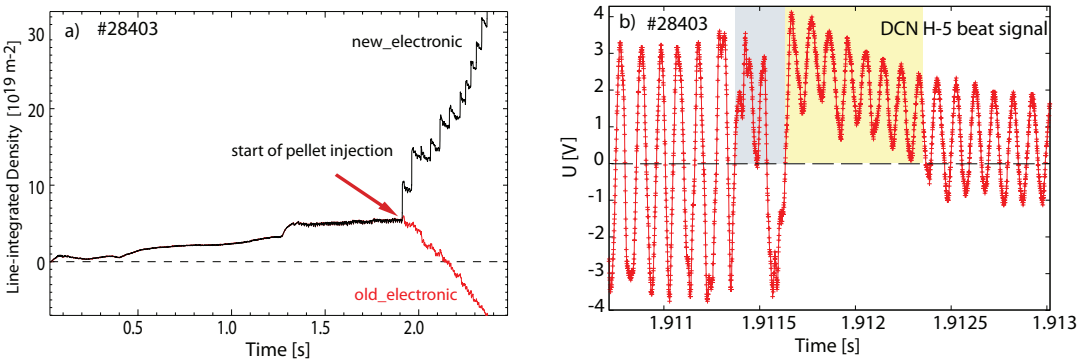

Figure A.1: a) Comparison between the old and new electronics: while the old electronic (in red) drifts towards low density values, the new one (black) drifts towards high density values. b) Raw detector signal of channel H-5 for discharge #28403. Pellet injection causes a drop of the amplitude. The signal does not cross the zero line for several oscillations.

The reconstruction of the phase from the raw signals was achieved in the following steps:

- The time traces of the raw signal are split into segments of the same length, each containing at least one full period.
- A sinusoid of the form $A \cdot sin(\omega t + \phi) + B$ is fitted to the signal in each segment using a Levenberg Marquardt least square method. For the fit initial values for the amplitude A, the phase ϕ and the offset B are required. These values are provided by finding the maximum and minimum within a segment: the offset B is given by the arithmetic mean of maximum and minimum, whereas the amplitude A is obtained calculating half the difference between maximum and minimum. The zero crossing provides the phase.
- The algorithm iterates until it finds the best fit parameter values which reduce the RMS of the errors between the measured data points and the calculated sinusoidal function.
- The desired phase shift modulo 2π is determined by the difference between the fitted phase and the reference phase. For the counting of the integer multiples of 2π, the phase variation from one segment to the next is considered to be always below half a period.
- The residue of the fit indicates whether there are any signal perturbations. In normal conditions, i.e. in absence of pellets, MHD activity or ELMs, the probe signal is a normal sinusoid and the residue of the Levenberg-Marquardt fit is low. In presence of one of the mentioned perturbations, the residue of the fit increases. Each perturbation exhibits a specific fingerprint determining which method has to be employed for fringe jump correction.

The effect of band-pass filtering the raw signals, as done by the hard-wired electronics, has been studied by applying a digital filter algorithm to the raw signals before performing phase reconstruction. In case of MHD activity the 10 KHz beat signal experiences a periodic amplitude modulation with a frequency f_{MHD}. It has been found that narrow band-pass filtering is suitable to remove MHD frequencies, provided that f_{MHD} is not too close to 10 kHz, but prevents detection of fast density changes. On the contrary, a broad band-pass is more suitable for pellet disturbances but it restricts the ability of the interferometer to provide a stable density measurement in presence of MHD activity. The hard-wired phase counters have a fixed bandwidth and therefore have to make a compromise between both goals. In this situation the advantage of using digital filtering becomes evident: it allows the adaption of the bandwidth selection depending on the desired object of analysis. For MHD-quiescent pellet discharges, large bandwidth (or not filtering at all) provides better results then the output of the the hard-wired electronics for two reasons: First the detrimental effect of the band-pass filter is avoided. Second, oscillation periods taking place entirely above the zero line (t = 1.918- 1.9123 s (yellow box) in figure A.1 b)) can be registered by the fitting algorithm, whereas they are lost in zero-crossing detection as applied in the phase counting electronics. The fitting algorithm delivers reliable results for small medium size pellets. For large pellets, however the perturbations are so strong that detecting the fast phase change due to pellets seems impossible without any additional information. In figure A.1 b), for example, phase tracking fails in the time window t =1.913- 1.917 s (blue box). Therefore, in order to correct the DCN time traces and provide the density profile for a high-density pellet discharge, a manual post-discharge approach was used. In the course of this work several attempts were made to manually correct high-density discharges starting from the density rise caused by the arrival of pellets. The most representative example is given by discharge #29714 illustrated in section 8.1 where 73 pellet-fringe jumps each for 5 channels were corrected. However, an ambiguity in the correction of channel H-5 still persisted, so that the exact density profile evolution throughout the pellet phase remains uncertain. The results presented in the following are instead obtained by beginning at the end of the discharge and performing fringe jump correction backward in time. In order to apply such a method, the discharge must not terminate in a disruption, nor exhibit perturbative events such as strong MHD activity after the last pellet. This condition was dubbed "soft-landing". A discharge with a rather soft-landing, to which this method was applied and the density profile reconstructed, is discharge #29674.

For this discharge, fringe jump corrections were required due to a minor MHD activity for the time window t= 7.65 - 7.85 s for all 5 DCN channels (figure A.2 a)). The pellet phase is excluded because of heavy perturbations of the DCN measurements. After the last pellet (at t= 4.21 s) measurements become available again. Since after the pellet train the discharge returns to its initial conditions, the fringe jump corrections in the post-pellet phase have been carried out such that they have the same density level as in the pre-pellet phase. Comparison with similar discharges was also used. After all fringe jumps had been corrected, an IDA profile based on this DCN data was calculated. The fitting procedure used to generate IDA profile can verify whether the fringe jumps corrections were indeed correct. The result, illustrated in figure A.2 b), shows a very good consistency of the DCN

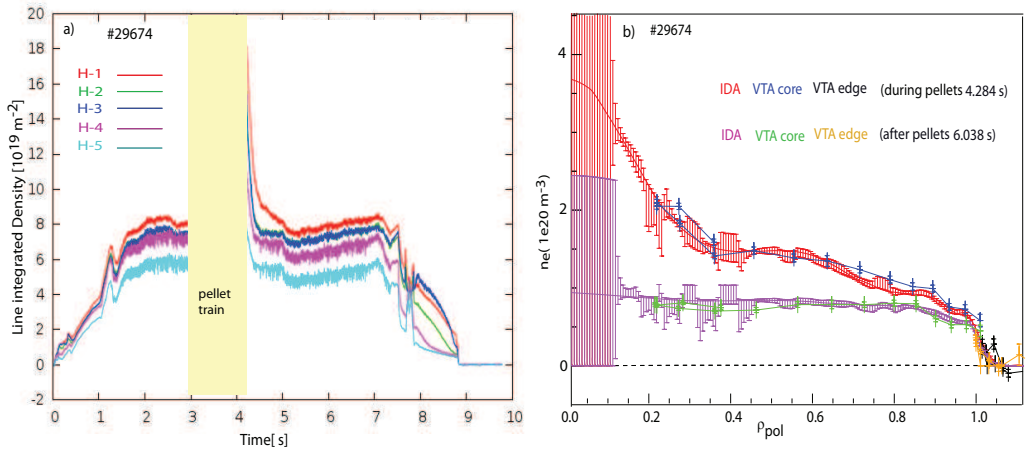

Figure A.2: a) Time traces of the 5 DCN channels corrected for fringe jumps. The gap between t= 2.94 - 4.21s was intentionally not corrected. The important zone is the density decay right after the gap; b) Comparison between the density profile obtained with IDA using the reconstructed DCN density and the VTA during the pellet train and after the pellet train. Note the very good agreement.

LOS with the TS data for both the time windows before and after the pellet train. The core density reconstructed by IDA gives a record core density of up to $3 \cdot n_{GW}$. Note that no measurements are available for $\rho_{pol} < 0.1$. It should be pointed out that this discharge has been carried out with the old DCN geometry (H-3 instead of H-0, see section 5.3.1). In the future it would be worth repeating this discharge with the new geometry where the density in the very core can be measured. Interestingly, after the injection of the last pellet, it takes about 300 ms until the density effect of the pellets has decayed outside about ρ_{pol}= 0.4. Instead, for ρ_{pol}< 0.4, the density profile is still rather peaked at that time and it takes further 500 ms until the density in the core is flat again. This means that two different time scales are involved as discussed in section 8.2.

Appendix B

Bibliography

[1] International energy agency (IEA). World energy oulook 2008 international energy agency. *(iea) publication*, 2008.

[2] R. Dux. Impurity transport in tokamak plasmas. *IPP report 10/27*, 2004.

[3] M. Greenwald, J.L. Terry, S.M. Wolfe, et al. A new look at density limits in tokamaks. *Nuclear Fusion*, 28(12):2199, 1988.

[4] G. Federici, C.H. Skinner, J.N. Brooks, et al. Plasma-material interactions in current tokamaks and their implications for next step fusion reactors. *Nuclear Fusion*, 41(12):1967, 2001.

[5] F. Wagner, G. Becker, K. Behringer, et al. Regime of Improved Confinement and High Beta in Neutral-Beam-Heated Divertor Discharges of the ASDEX Tokamak. *Phys. Rev. Lett.*, 49:1408–1412, 1982.

[6] H. Zohm. Edge localized modes (ELMs). *Plasma Physics and Controlled Fusion*, 38(2):105, 1996.

[7] R. Aymar, P. Barabaschi, and Y. Shimomura. The ITER design. *Plasma Physics and Controlled Fusion*, 44(5):519, 2002.

[8] ITER. General ITER website. url, 21.11.2012.

[9] H. Zohm. On the Minimum Size of DEMO. *Fusion Science and Technology*, 58(2):613–624, 2010.

[10] H. Zohm. *Magnetohydrodynamic Stability of Tokamaks*. WILEY VCH Verlag Publications, 2015.

[11] F. Ryter. PhD Network lecture. 2012.

[12] M. Kiikuchi, K. Lackner, and M. Tran. Fusion Physics. *IAEA Internation Atomic Energy Agency Press*, 2012.

[13] J. Wesson. *Tokamaks*. Oxford Science Publications, Oxford, 1997.

[14] C. Angioni, A.G. Peeters, G.V. Pereverzev, et al. Theory-based modeling of particle transport in ASDEX Upgrade H-mode plasmas, density peaking, anomalous pinch and collisionality. *Physics of Plasmas*, 10(8):3225–3239, 2003.

[15] A.A. Ware. Pinch-Effect Oscillations in an Unstable tokamak Plasma. *Phys. Rev. Lett.*, 25(916), 1970.

[16] T. Pütterich. Control and diagnostic of high-Z Impurities in Fusion Plasmas. *Habilitation LMU*, 2014.

[17] G. Tardini. Validation of theory based transport models in tokamaks plasmas. *IPP report 5/102*, 2003.

[18] B. Coppi and F. Pegoraro. Theory of the ubiquitous mode. *Nuclear Fusion*, 17(5):969, 1977.

[19] F. Romanelli. Ion temperature-gradient-driven modes and anomalous ion transport in tokamaks. *Phys. Plasmas*, 1:1018, 1989.

[20] J. Weiland, A.B. Jarmén, and H. Nordman. Diffusive particle and heat pinch effects in toroidal plasmas. *Nuclear Fusion*, 29(10):1810, 1989.

[21] B. Coppi and G. Rewoldt. New Trapped-Electron Instability. *Phys. Rev. Lett.*, 33:1329–1332, 1974.

[22] F. Jenko, W. Dorland, and G.W. Hammett. Critical gradient formula for toroidal electron temperature gradient modes. *Phys. Plasmas*, 8:4096, 2001.

[23] *IPP Summer University for Plasma Physics*. Max-Planck-Institut für Plasmaphysik, Garching, 2012.

[24] C. Angioni and A.G. Peeters. Direction of impurity pinch and auxiliary heating in tokamak plasmas. *Phys. Rev. Lett.*, 96:095003, 2006.

[25] X. Garbet, P. Mantica, F. Ryter, et al. Profile stiffness and global confinement . *Plasmas Physics and Controlled Fusion*, 46(9):1351, 2004.

[26] F. Imbeaux, R. Ryter, and X. Garbet. Modelling of ECH modultion experiments in ASDEX Upgrade with an empirical critical temperature gradient length transport model. *Plasma Physics and Controlled Fusion*, 43(1503), 2001.

[27] T. Dannert and F. Jenko. Gyrokinetic simulation of collisionless trapped-electron mode. *Physics of Plasmas*, 12(072309), 2005.

[28] F. Ryter, G. Tardini, F. De Luca, et al. Electron heat transport in ASDEX Upgrade: experiment and modelling. *Nuclear Fusion*, 43(11):1396–1404, 2003.

[29] F. Ryter, Y. Camenen, J.C. DeBoo, et al. Electron heat transport studies. *Plasma Physics and Controlled Fusion*, 48:B453–B463, 2006.

[30] T. Pütterich, R. Dux, M.A. Janzer, R.M. McDermott, and ASDEX Upgrade Team. ELM flushing and Impurity Transport in the H-mode Edge Barrier in ASDEX Upgrade. *Journal of Nuclear Materials*, 415(1, Supplement):S334–S339, 2011.

[31] W.W. Engelhardt. Wall effects and impurities in JET. *Phil. Trans. R. Soc.Lond.*, 322:79–94, 1987.

[32] H. P. Summers. Atomic data and analysis structure user manual. *JET-IR 06 Abingdon: JET Joint Undertaking Report*, 1994.

[33] P.G. Carolan and V.A. Piotrowicz. The behaviour of impurities out of coronal equilibrium. *Plasma Physics*, 25:1065–1086, 1983.

[34] H.P. Summers, W.J. Dickson, M.G. OḾullane, et al. Ionization state, excited populations and emission of impurities in dynamic finite density plasmas: I. The generalized collisional-radiative model for light elements. *Plasma Phys. Control. Fusion*, 48(2):263, 2006.

[35] R. Dux, A.G. Peeters, A. Gude, et al. Z dependence of the core impurity transport in ASDEXUpgrade H-Mode discharges. *Nuclear Fusion*, 39(11):1509–1522, 1999.

[36] R. Neu, R. Dux, A. Geier, et al. New results from the tungsten programme at ASDEX Upgrade. *Journal of Nuclear Materials*, 313–316:116–126, 2003.

[37] A. Kallenbach, M. Bernert, R. Dux, et al. Impurity seeding for tokamak power exhaust: from present devices via ITER to DEMO. *Plasma Physics and Controlled Fusion*, 55(12):124041, 2013.

[38] A. Kallenbach, M. Bernert, M. Beurskens, et al. Partial detachment of high power discharges in asdex upgrade. *Nuclear Fusion*, 55(5):124041, 2015.

[39] R.J. Hawryluk. An Empirical Approach to Tokamak Transport. *Physics of Plasmas Close to Thermonuclear Conditions*, 1:19–46, 1980.

[40] PPPL. TRANSP website. 26.04.2013. Available online at `http://w3.pppl.gov/transp`.

[41] G. Pereverzev and P.N. Yushmanov. ASTRA Automated System for TRansport Analysis in a Tokamak. IPP report 5/98, 2002.

[42] P.J. Mc Carthy. Analytical solutions to the Grad–Shafranov equation for tokamak equilibrium with dissimilar source functions. *Physics of Plasmas*, 6(9):3554–3560, 1999.

[43] A. Pankin, D. McCune, R. Andre, G. Bateman, and A. Kritz. The tokamak Monte Carlo fast ion module NUBEAM in the National Transport Code Collaboration library. *Computer Physics Communications*, 159(3):157–184, 2004.

[44] Behringer. *Journal of Nuclear Materials*, 415:334, 1987.

[45] R. Dux. STRAHL manual report IPP 10/30. *Max Planck Institut für Plasmaphysik, Garching*, 2006.

[46] A.G. Peeters, J. Stober, D. Coster, R. Schneider, and ASDEX Upgrade Team. The influence of neutral friction and neoclassical viscosity in the edge of ASDEX Upgrade. *Plasma Physics and Controlled Fusion*, 40(5):703–706, 1998.

[47] A.G. Peeters. Reduced Charge State Equations that Describe Pfirsch Schlüter Impurity Transport in Tokamak Plasma. *Phys. Plasmas*, 7(1):268–275, 2000.

[48] R. Dux and A.G. Peeters. Neoclassical impurity transport in the core of an ignited tokamak plasma. *Nuclear Fusion*, 40(10):1721–1729, 2000.

[49] R. Wenninger, T. Eich, E. Fable, et al. DEMO power and particle exhaust limits during and in between ELMs. *Nuclear Fusion*, 54:114003, 2015.

[50] A.A. Ivanov, R.R. Khayrutdinov, S.Yu. Medvedev, and Yu.Yu. Poshekhonov. New Adaptive Grid Plasma Evolution Code SPIDER. *Europhysics Conference Abstracts (CD-ROM, Proc. of the 32th EPS Conference on Plasma Physics, Tarragona, Spain, 2005)*, 29C:P5.063, 2005.

[51] R. Neu, R. Dux, A. Geier, et al. Impurity behaviour in the ASDEX Upgrade divertor tokamak with large area tungsten walls. *Plasma Physics and Controlled Fusion*, 44(6):811–826, 2002.

[52] B. Streibl, P.T. Lang, F. Leuterer, J.M. Noterdaeme, and A. Stabler. Chapter 2: Machine design, fueling, and heating in ASDEX upgrade. *Fusion science and technology*, 44(3):578–592, 2003.

[53] J. Stober, A. Bock, H. Höhnle, et al. ECRH on ASDEX Upgrade - System Status, Feed-Back Control, Plasma Physics Results. *EPJ Web of Conferences*, 32:02011, 2012.

[54] E. Poli, G.V. Pereverzev, and A.G. Peeters. Paraxial Gaussian wave beam propagation in an anisotropic inhomogeneous plasma. *Physics of Plasmas*, 6(1):5–11, 1999.

[55] R. Dux, R. Neu, A.G. Peeters, et al. Influence of the heating profile on impurity transport in ASDEX Upgrade. *Plasma Physics and Controlled Fusion*, 45(9):1815–1825, 2003.

[56] A. Kallenbach, R. Dux, M. Mayer, et al. Non-boronized compared with boronized operation of ASDEX Upgrade with full-tungsten plasma facing components. *Nuclear Fusion*, 49(4):045007, 2009.

[57] H. Faugel, P. Angenie, W. Becker, et al. The ASDEX Upgrade ICRF system: Operational experience and developments. *fusion engineering and design*, 74(1-4):319–324, 2005.

[58] R. Bilato, M. Brambilla, O. Maj, et al. Simulations of combined neutral beam injection and ion cyclotron heating with the TORIC-SSFPQL package. *Nuclear Fusion*, 51(10):103034, 2011.

[59] D. Veron. High sensitivity HCN laser interferometer for plasma electron density measurements. *Optics Communication*, 10(1), 1974.

[60] A. Mlynek, G. Schramm, H. Eixenberger, et al. Design of a digital multiradian phase detector and its application in fusion plasma interferometry. *Review of Scientific Instruments*, 81(3):033507, 2010.

[61] A. Mlynek. Real time control of the plasma density profile on ASDEX Upgrade. *PhD thesis, LMU*, 2010.

[62] H. Murmann, S. Götsch, H. Röhr, H. Salzmann, and K. H. Steuer. The Thomson scattering systems of the ASDEX upgrade tokamak. *Review of Scientific Instruments*, 63(10):4941–4943, 1992.

[63] B. Kurzan and H.D. Murmann. Edge and core Thomson scattering systems and their calibration on the ASDEX Upgrade tokamak. *Review of Scientific Instruments*, 82(10):103501, 2011.

[64] J. Schweinzer, E. Wolfrum, F. Aumayr, and M. Ploeckl. Reconstruction of plasma edge density profiles from lii(2s-2p) emission profiles. *Plasma Phys. Control Fusion*, 34(7):1173, 1992.

[65] M. Willensdorfer, E. Wolfrum, R. Fischer, et al. Improved chopping of a lithium beam for plasma edge diagnostic at ASDEX Upgrade. *Review of Scientific Instruments*, 83(2):023501, 2012.

[66] S.K. Rathgeber, L. Barrera, T. Eich, et al. Estimation of edge electron temperature profiles via forward modelling of the electron cyclotron radiation transport at asdex upgrade. *Plasma Physics and Controlled Fusion*, 55(2):025004, 2013.

[67] W. Suttrop, A.G. Peeters, ASDEX Upgrade Team, and NBI Group. Practical limitations to plasma edge electron temperature measurements by radiometry of electron cyclotron emission. Technical Report 1/306, IPP, Garching, Germany, December 1996.

[68] R. Fischer, C.J. Fuchs, B. Kurzan, et al. Integrated data analysis of profile diagnostics at asdex upgrade. *Fusion Science and Technology*, 58(2):675–684, 2010.

[69] E. Viezzer, T. Pütterich, R. Dux, R.M. McDermott, and ASDEX Upgrade Team. High-resolution charge exchange measurements at asdex upgrade. *Review of Scientific Instruments*, 83(10):103501, 2012.

[70] A. Kappatou. PhD Thesis, Eindhoven University of Technology, The Netherlands. 2014.

[71] L. Giannone, D. Queen, F. Hellman, and J.C. Fuchs. Prototype of a radiation hard resistive bolometer for ITER. In C. Hidalgo and B. Ph. van Milligen, editors, *Europhysics Conference Abstracts (CD-ROM, Proc. of the 32nd EPS Conference on Plasma Physics, Tarragona, 2005)*, volume 29C, pages P–5.084, Geneva, 2005. EPS.

[72] M. Bernert, T. Eich, A. Burckhart, et al. Application of AXUV diode detectors at ASDEX Upgrade. *Review of Scientific Instruments*, 85(3):033503, 2014.

[73] M. Bernert. Analysis of the H-mode density limit in the ASDEX Upgrade tokamak using bolometry. *IPP report 17/38*, 2013.

[74] T. Pütterich, R. Neu, R. Dux, et al. Modelling of measured tungsten spectra from ASDEX Upgrade and predictions for iter. *Plasma Physics and Controlled Fusion*, 50(8):085016, 2008.

[75] A. Kallenbach, M. Bernert, T. Eich, et al. Optimized tokamak power exhaust with double radiative feedback in asdex upgrade. *Nuclear Fusion*, 52(12):122003, 2012.

[76] J. Schweinzer, A.C.C. Sips, G. Tardini, et al. Confinement of 'improved H-modes' in the all-tungsten ASDEX Upgrade with nitrogen seeding. *Nuclear Fusion*, 51(11):113003, 2011.

[77] G. Tardini, R. Fischer, F. Jenko, et al. Core transport analysis of nitrogen seeded h-mode discharges in the asdex upgrade. *Plasma Physics and Controlled Fusion*, 55(1):015010, 2013.

[78] J.C. Fuchs, K.F. Mast, A. Herrmann, et al. Twodimensional reconstruction of the radiation power density in ASDEX Upgrade. In E. Joffrin, P. Platz, and P.E. Stott, editors, *Europhysics Conference Abstracts (Proc. of the 21th EPS Conference on Controlled Fusion and Plasma Physics, Montpellier, 1994)*, volume 18B, part III, pages 1308–1311, Geneva, 1994. EPS.

[79] P.A. Schneider, E. Wolfrum, M.G. Dunne, et al. Observation of different phases during an elm crash with the help of nitrogen seeding. *Plasma Physics and Controlled Fusion*, 56(2):025011, 2014.

[80] M. G. Dunne, L. Frassinetti, M. Beurskens, et al. Impact of nitrogen seeding on the aug pedestal: experiments and modelling. In *Europhysics Conference Abstracts (Proc. of the 42th EPS Conference on Plasma Physics, Lisbon, 2015)*, 2015.

[81] G. Tardini, C. Höhbauer, R. Fischer, R. Neu, and ASDEX Upgrade Team. Simulation of the neutron rate in asdex upgrade h-mode discharges. *Nuclear Fusion*, 53(6):063027, 2013.

[82] D.J. Campbell. The physics of the international thermonuclear experimental reactor feat. *Physics of Plasmas*, 8(5), 2001.

[83] R. Neu, R. Dux, A. Kallenbach, et al. Influence of the ^4He concentration on h-mode confinement and transport in ASDEX Upgrade. In P. Lalousis and S. Moustaizis, editors, *Europhysics Conference Abstracts (CD-ROM, Proc. of the 35th EPS Conference on Plasma Physics, Hersonissos, Crete, 2008)*, volume 32D, pages P–4.039, Geneva, 2008. EPS.

[84] A. Loarte, M. Becoulet, G. Saibene, et al. Characteristics and scaling of energy and particle losses during Type I ELMs in JET H-modes. *Plasma Phys. Control. Fusion*, 44, 2002.

[85] R. Bilato, M. Brambilla, D.A. Hartmann, and A. Parisot. Influence of an evanescence layer in front of the antenna on the coupling efficiency of ion cyclotron waves. *Nuclear Fusion*, 45(2):L5, 2005.

[86] C. Angioni O. Sauter. Neoclassical conductivity and bootstrap current formulas for general axisymmetric equilibria and arbitrary collisionality regime. *Physics of Plasmas*, 6(7), 1999.

[87] W. Suttrop. The physics of large and small edge localized modes. *Plasma Physics and Controlled Fusion*, 42(5A):A1–A14, 2000.

[88] R. Dux, A. Janzer, T. Pütterich, and ASDEX Upgrade Team. Main chamber sources and edge transport of tungsten in h-mode plasmas at asdex upgrade. *Nuclear Fusion*, 51(5):053002, 2011.

[89] T. Pütterich, R. Dux, M.A. Janzer, R.M. McDermott, and ASDEX Upgrade Ream. ELM flushing and Impurity Transport in the H-mode Edge Barrier in ASDEX Upgrade. *Journal of Nuclear Materials*, 415(1, Supplement):S334–S339, 2011.

[90] Fundamenski W, R A Pitts, and JET EFDA contributors. A model of ELM filament energy evolution due to parallel losses. *Plasma Phys. Control. Fusion*, 46(233), 2004.

[91] T. Eich, A. Herrmann, G. Pautasso, et al. Power deposition onto plasma facing components in poloidal divertor tokamaks during type-i ELMs and disruptions. *Journal of Nuclear Materials*, 337-339:669–676, 2005.

[92] Bogomolov A., Classen I.G.J., de Donne, et al. The effect of nitrogen seeding on ELM filaments. *Submitted to Nuclear Fusion*, 2015.

[93] S. Pamela, G.Huijsmans, A.Kirk, I.Chapman, and the MAST team. Effect of SOL temperature on Filament dynamics in MAST. 2014.

[94] P.B. Snyder, H.R. Wilson, J.R. Ferron, et al. Edge localized modes and the pedestal: A model based on coupled peeling–ballooning modes. *Physics of Plasmas*, 9(5):2037–2043, 2002.

[95] W Suttrop, L Barrera, A Herrmann, et al. Studies of edge localized mode mitigation with new active in-vessel saddle coils in asdex upgrade. *Plasma Physics and Controlled Fusion*, 53(12):124014, 2011.

[96] W. Suttrop, V. Hynönen, T. Kurki-Suonio, et al. Studies of the 'quiescent h-mode' regime in ASDEX Upgrade and JET. *Nuclear Fusion*, 45(7):721–730, 2005.

[97] J. Schweinzer, V. Bobkov, A. Burckhart, et al. Demonstration of the iter baseline scenario on asdex upgrade. In V. Naulin, C. Angioni, M. Borghesi, et al., editors, *Europhysics Conference Abstracts (CD-ROM, Proc. of the 40th EPS Conference on Plasma Physics, Espoo, Finland, 2013)*, volume 37D of *ECA*, page P2.134, Geneva, 2013. European Physical Society.

[98] R. Dux, A. Peeters, A. Gude, et al. Measurement of impurity transport coefficients in the confined plasma of ASDEX Upgrade. In *Proc. of the 18th IAEA Conference Fusion Energy (CD-Rom), Sorrento, Italy, October 2000*, volume IAEA-CSP-8/C, pages IAEA–CN–77/EXP5/32, Vienna, 2001. IAEA.

[99] B. Plöckl, P.T. Lang, G. Sellmair, et al. The enhanced high speed inboard pellet fuelling system at ASDEX Upgrade. *Fusion Engineering and Design*, 88(6-8):1059–1063, 2013.

[100] P.T. Lang, K. Büchl, M. Kaufmann, et al. High-Efficiency Plasma Refuelling by Pellet Injection from the Magnetic High-Field Side into ASDEX Upgrade. *Phys. Rev. Lett.*, 79:1487–1490, 1997.

[101] P.T. Lang, A. Burckhart, M. Bernert, et al. Elm pacing and high-density operation using pellet injection in the asdex upgrade all-metal-wall tokamak. *Nuclear Fusion*, 54(8):083009, 2014.

[102] C. Angioni, A.G. Peeters, G.V. Pereverzev, et al. Theory-based modeling of particle transport in ASDEX Upgrade h-mode plasmas, peaking, anomalous pinch and collisionality. *Physics of Plasmas*, 10(8):3225–3239, 2003.

[103] F. Sommer. Thermal insulation of high confinement mode with dominant electron heating in comparison to dominant ion heating and corresponding changes in torque input. *IPP report 1/352*, 2013.

[104] O. Kardaun. *for the ITPA global confinement database WG, Proc. 21th Conf. Plasma Phys. Control. Nucl.Fusion Res., Chengdu 2006*, IT/p1-10, 2006.

[105] G. Saibene, L.D. Horton, R. Sartori, et al. The influence of isotope mass, edge magnetic shear and input power on high density elmy h modes in jet. *Nucl. Fusion*, 39:1133, 1999.

[106] J. Stober, O. Gruber, A. Kallenbach, et al. Effects of triangularity on confinement, density limit and profile stiffness of H-Modes on ASDEX Upgrade. *Plasma Physics and Controlled Fusion*, 42(5A):A211–A216, 2000.

[107] O. Kardaun. *Private communication*, 2014.

[108] G.T. Hoang, C. Bourdelle, and B. Pergourie et al. Particle pinch with fully non-inductive lower hybrid current drive in tore supra. *Phys. Rev. Lett.*, 90(155002), 2003.

[109] H.R. Koslowski. A real-time multiradian phase detector for interferometry based on a digital phase locked loop circuit.

Acknowledgements

At this point it is a pleasure to convey my gratitude to the people that have aided and supported me in these three years.

I am deeply grateful to my direct supervisor Dr. Francois Ryter who introduced me to the complex world of plasma transport and guided me throughout the whole project. Thanks for all your knowledge and support with suggestion of further investigations. Your critical appraisal of my work is inestimable.

My sincere thank is owed to Prof. Dr. Hartmut Zohm. Thank you for giving me the opportunity to perform this thesis at IPP under your academic supervision. I'm grateful for the discussions and for the help to find out the essential questions at the basis of my thesis. Thanks for being always enthusiastic to read "something" also during the weekends.

I am deeply indebted to Dr. Emiliano Fable who introduced me to ASTRA and to the the modelling work. Thanks for all the interest you showed in my work, for making always time to answer my questions and discuss the results. *Grazie anche per le chiacchierate all' italiana!*

I would like to express my sincere gratitude to Dr. Alexander Mlynek for having introduced me into the field of interferometry. Thanks for your enthusiasm, your endless knowledge, precise and constructive comments. I will never forget your support in making the famous 74 DCK editions!

I gratefully acknowledge Dr. Ralph Dux for the maintenance of STRAHL and for always been willing to answer my questions.

I sincerely thank Dr. Giovanni Tardini for being always available to answer questions about TRANSP and facilitating his use.

I would like to thank Dr. Matthias Bernert for having introduced me in the topic of the tomography reconstruction. I will always remember the nice smiling face we retrieved from one of our deconvolutions! Thanks also for the most delicious Spaetzle I have eaten so far.

Many thanks go to Dr. Rainer Fischer for providing IDA profiles and to Dr. Rachael Mc. Dermott for the impurity density profiles.

I am also grateful to Prof. Arne Kallenbach, Dr. Clemente Angioni and Dr. Thomas Pütterich, Dr. Marco Sertoli for fruitful discussions and helpful comments.

The experiments for this thesis were conducted at ASDEX Upgrade. I want to thank the whole experimental team, and in particular Prof. Arne Kallenbach, Dr. Mike Dunne for the high radiation experiments and Dr. Peter Lang for the high density experiments.

Special thanks deserve the IT Group for their support and their availaibilty.

Appreciation also goes out to our secretaries Anja Bauer, Gabriele Dörsch, Petra Jordan and Margot Jung for all of their administrative assistance.

I would like to thank my adventure companions in the phD Network, especially Alexander Bock, Luis Guimares, Marco Barbisan and Nicola Funnesu for the great time in Padova and Lisbon.

Special thanks go to my office mates and all my fellow PhD students and postdocs at IPP. Thank you for good time and nice discussions at lunches, conferences, parties.

I would like to thank my friends outside IPP who made my life in Munich a great experience up to now. Thank to my friend working at the "egg-reactor" next to IPP building for nice lunches and for making me discover good pizzerias in Munich! A special thank goes to my dearest friend Silvia, your friendship throughout all these years is really precious to me! Thanks for understanding my limited time in the last period.

Thank to my friend in Italy for keeping the contacts and being there to welcome me back.

Exactly 10 years ago in this time of the year I was graduating in ballet at the Conservatory in Rome. Deepest gratitude to my ballet teachers in the academy for having transmitted me the passion and dedication in arts and in life in general and for build my personality trough extenuating daily training.

I would like to conclude these acknowledgements with a deep gratitude to my family. I thanks my parents for their unconditional love and support, for the joy of intellectual pursuit you transmitted me and for representing a solid reference point. Ilaria, thanks for being supportive and caring sister. You have been always an example for me. I would like to thank also my "German family" for their interest in the progress of this work. Fabian, words fail me to express my deep appreciation for your support, your patience, your encouragement and your belief in me and in what I can achieve.
Questa tesi è dedicata a voi!